First-principles calculations on the stabilization of iron carbides (Fe_3C, Fe_5C_2 and η-Fe_2C) in steels

PROEFSCHRIFT

ter verkrijging van de graad van doctor
aan de Technische Universiteit Delft,
op gezag van de Rector Magnificus prof. ir. K.C.A.M. Luyben,
voorzitter van het College voor Promoties,
in het openbaar te verdedigen op donderdag 17 oktober 2013 om 10:00 uur

door

Chaitanya Krishna ANDE

Master of Science in Chemical Sciences
Indian Institute of Science, Bengaluru, India
geboren te Vijayawada, India

Dit proefschrift is goedgekeurd door de promotor:

Prof.dr. B.J. Thijsse, Technische Universiteit Delft
Copromotor Dr.ir. M.H.F. Sluiter, Technische Universiteit Delft

Samenstelling promotiecommissie:

Rector Magnificus, voorzitter
Prof.dr. B.J. Thijsse, Technische Universiteit Delft, promotor
Dr.ir. M.H.F. Sluiter, Technische Universiteit Delft, copromotor
Prof.dr. D. Lamoen, Universiteit Antwerpen, Belgium
Prof.dr. E.H. Brück, Technische Universiteit Delft
Prof.dr.ir. B.J. Kooi, Universiteit Groningen
Prof.dr. R.A. de Groot, Radboud Universiteit Nijmegen
Dr. W. Kranendonk, Tata Steel Europe, IJmuiden
Prof.dr.ir. C.R. Kleijn, Technische Universiteit Delft, reservelid

This research was carried out under project number MC5.05239 in the framework of the Research Program of Materials innovation institute(M2i) in the Netherlands(www.m2i.nl)

ISBN: 978-90-77172-97-1

Printed and published by Proefschriftmaken.nl | | Uitgeverij BOXPress, ’s-Hertogenbosch

Propositions

belonging to the Ph.D. thesis of Chaitanya Krishna Ande

First-principles calculations on the stabilization of iron carbides (Fe_3C, Fe_5C_2 and η-Fe_2C) in steels

1. Computer simulation will totally replace experiment in the design of new materials.
2. As a corollary, rapid development of steels cannot be achieved without inputs from computational modeling.
3. A universally valid exchange-correlation functional will never be found.
4. First-principles results will soon be benchmarks for experimental results.
5. Formation enthalpies cannot predict partitioning of alloying elements between iron and carbide phases (Chap. 6 and 7).
6. Developing countries may violate intellectual property rights.
7. Publicly funded institutions should only use "open source" software.
8. The ratio of the highest and the lowest pay in an organization should be transparent and fixed.
9. Playing the stock market is a sure way to lose money and peace of mind.
10. Social life in the Netherlands is critically dependent on the availability of Belgian beer.

These propositions are regarded as opposable and defendable, and have been approved as such by supervisors prof.dr. B.J. Thijsse and dr.ir. M.H.F. Sluiter.

Stellingen

behorende bij het proefschrift van Chaitanya Krishna Ande

First-principles calculations on the stabilization of iron carbides (Fe_3C, Fe_5C_2 and η-Fe_2C) in steels

1. Voor het ontwerpen van nieuwe materialen zullen experimenten geheel door computer simulatie vervangen worden.
2. Een logisch gevolg is dan dat de snelle ontwikkeling van staalsoorten niet bereikt kan worden zonder computer simulaties.
3. Een universeel geldige exchange-correlatie functionaal zal nooit gevonden worden.
4. Ab initio resultaten zullen spoedig ijkpunten zijn voor experimentele resultaten.
5. Formatie-enthalpieën kunnen de partitionering van legeringselementen tussen ijzer en carbide fasen niet voorspellen (hoofdstukken 6 en 7).
6. Ontwikkelingslanden mogen intellectuele eigendomsrechten schenden.
7. Overheidsinstellingen zouden uitsluitend “open source” programmatuur moeten gebruiken.
8. De verhouding tussen de hoogste en de laagste salarissen in een organisatie zouden openbaar moeten zijn en vast moeten liggen.
9. Gokken op de beurs zal zeker leiden tot het verlies van geld en gemoedsrust.
10. Het sociale leven in Nederland is totaal afhankelijk van de beschikbaarheid van Belgisch bier.

Deze stellingen worden opponeerbaar en verdedigbaar geacht en zijn als zodanig goedgekeurd door de promotoren prof.dr. B.J. Thijsse and dr.ir. M.H.F. Sluiter.

. . . to my parents, brother and grandparents

Contents

Chapter 1

Introduction

In this chapter, a general introduction to steels, their design, and the role that first-principles calculations can play in the design of steels is presented. The motivation of the present thesis in using first-principles calculations to aid in the design of new TRIP steels is then given.

1.1 Steel[1]

Steel is one of the most important structural materials that is available to mankind since its mass production started with the invention of the Bessemer process in the mid-19th century. It is an alloy that consists mostly of iron and has a carbon content between a few ppm and 2.1% by weight depending on the grade. While carbon is the most common alloying element, various other alloying elements can also be used, such as aluminium, silicon, phosphorus, sulfur, titanium, vanadium, chromium, manganese, nickel, cobalt, copper, zinc, niobium, molybdenum and tungsten. The choice of the alloying elements used in the steel depends on the properties expected of the steel. Carbon and other alloying elements act as hardening agents, preventing dislocations in the iron lattice from sliding past one another. Varying the amount of alloying elements and the form of their presence in the steel (solute elements, precipitated phase) controls qualities such as the hardness, ductility, and tensile strength of the resulting steel. Before going further, it would be instructive to look at the iron-carbon phase diagram first.

1.2 Iron-carbon phase diagram

The presence of C and other alloying elements alters the phase diagram of pure iron. The phase diagram for iron and carbon should in principle be between

---

[1] Experts on steel and TRIP steel can directly go to Sec. 1.4

iron and graphite because graphite is thermodynamically the most stable form of carbon. Nonetheless, the iron-graphite phase diagram is seldom used because graphite seldom forms in the processing of steels. It is cementite, a metastable carbide that exists infinitely at room temperature, that occurs in steels. An iron-cementite phase diagram is therefore used instead of an iron-carbon phase diagram.

The Fe-Fe_3C phase diagram is shown in Fig. 1.1. Pure iron exists as bcc-Fe (ferrite, α) at room temperature and transforms into fcc-Fe (austenite, γ) at 912 °C and transforms into δ-Fe at an even higher temperature of 1394 °C. It finally melts at 1538 °C. The α phase is ferromagnetic, while the γ and the δ phases are paramagnetic [1].

Carbon (C), the major alloying element in steels, dissolves interstitially in bcc-Fe with a maximum solubility of about 0.022 wt%. The solubility of C in the γ phase is much higher at about 2.14 wt%. The final form of a steel is usually obtained by first heating it with all the alloying elements into the liquid phase, then cooling it via different phases (γ, γ+α, etc.) (for example, follow the grid line at 1 % C composition in Fig. 1.1) and finally tempering it. Roughly speaking, the rate at which austenite is cooled and tempered determines the microstructure of steels that we finally obtain. At a slow rate of cooling, we obtain pearlite; at a moderate cooling rate, we obtain bainite; and with a rapid quench, we obtain martensite which is then tempered to obtain tempered martensite (Fig. 1.2). Pearlite and bainite are microstructures in steel and martensite is a body centered tetragonal phase of bcc-Fe with a supersaturation of C in the crystal structure. The hardness of the three in increasing order is: pearlite $<$ bainite $<$ martensite.

Since the solubility of C in the α phase is much less than its solubility in the γ phase, a lot of carbon in the solid solution with iron precipitates out of the solution in the form of carbides (cementite, Hägg carbide, η-carbide, TiC, NbC, etc.) during cooling from the high temperature austenite to the room temperature ferrite phase. These carbides, thus effectively act as 'carbon sinks'.

Other alloying elements that are added in addition to C alter the phase diagram of the Fe-Fe_3C phase diagram further and lead to the necessity of studying ternary phase diagrams of the Fe-C-X type. These additional alloying elements can lead to the formation of new precipitate phases. Although cementite is the most common carbide observed in steels, other alloying elements and thermo-mechanical processing can lead to other precipitate phases to form during the steel making process. In the case of cementite formation, other carbides appear to precipitate, with increasing temperature, in the order: i) η-Fe_2C (η-carbide), ii) Fe_5C_2(Hägg carbide) and iii) Fe_3C [3,4]. The appearance of ϵ-Fe_2C precedes η-Fe_2C.

1.3 TRIP Steel

A large number of steels are presently available (Fig. 1.3) with a wide range of properties. The choice of the steel obviously depends on the target application. Of the numerous types of steels available at present, TRIP (TRansformation Induced

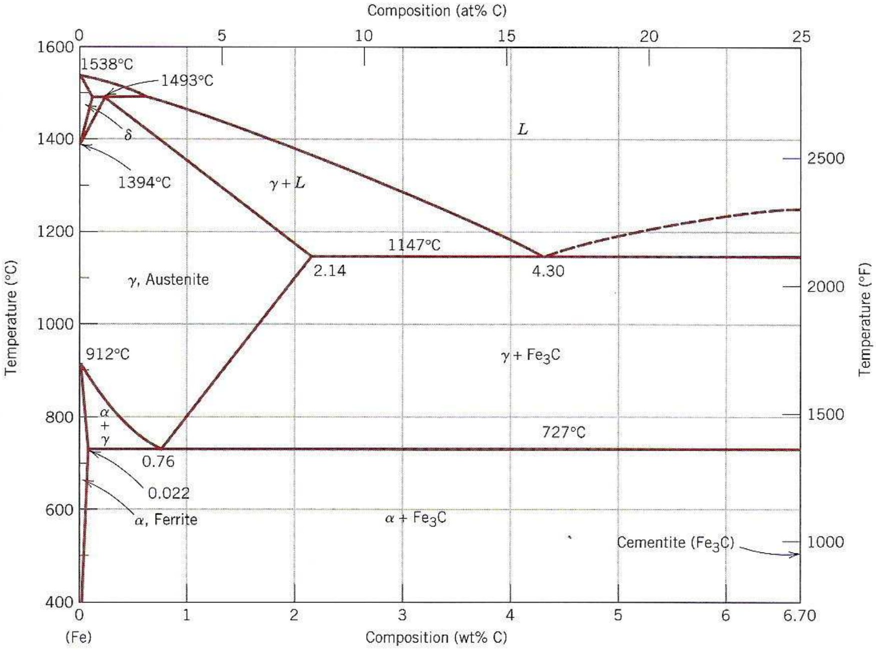

Figure 1.1: Fe-Fe$_3$C phase diagram

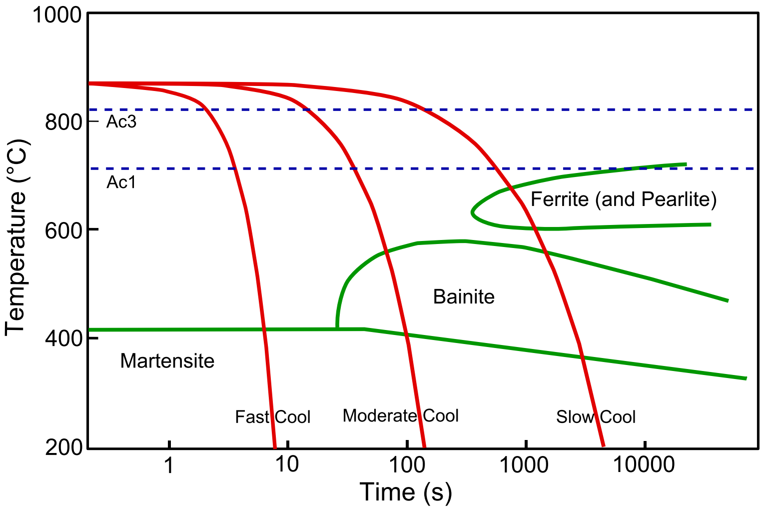

Figure 1.2: Continuous cooling transformation diagram for steel. Ac1 is the temperature at which austenite begins to form on heating; and Ac3 is the temperature at which ferrite in a hypoeutectoid steel completely transforms to austenite [2].

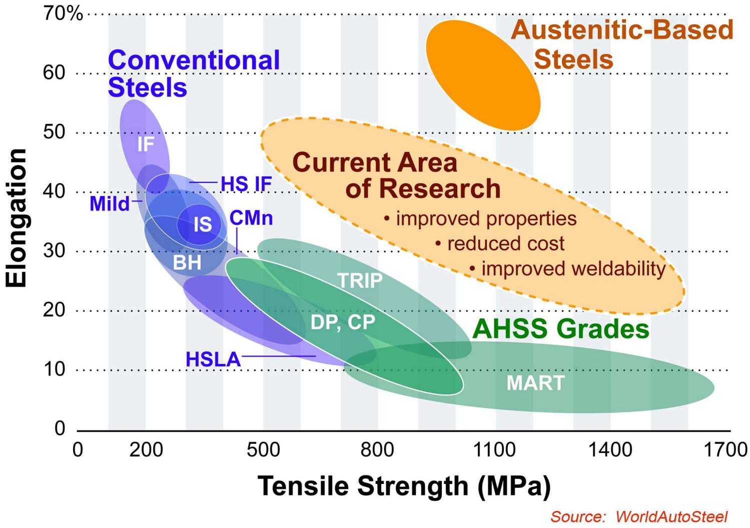

Figure 1.3: Various steel grades presently available. HS (High Strength), IF (Interstitial Free), HSLA (High Strength Low Alloy), DP (Dual Phase), CP (Complex Phase), TRIP (TRansformation Induced Plasticity)

Plasticity) steels are low-alloy steels that combine properties of enhanced strength and ductility. This satisfies the requirements of the automotive industry for good formable high-strength steels. TRIP steels consist of a triple-phase microstructure consisting of ferrite, bainite and retained austenite [5]. Austenite is a soft and ductile phase while martensite is hard and brittle. The TRIP effect exploits the properties of these phases to achieve the required strength and ductility. The soft phase, austenite, is stabilized to room temperature and transforms to the hard phase, martensite, on application of external stress and/or plastic deformation. Hence, it is important that austenite is stabilized to room temperature to achieve a good TRIP effect. Carbon is one agent that aids the stabilization of austenite to room temperature. Carbon is much more soluble in austenite than in ferrite and when austenite transforms to ferrite, the ferrite expels the excess carbon. One way for ferrite to expel carbon is by forming carbide precipitates, either of iron or of other alloying elements available in the steel. For TRIP steels, where the C has to be held in the iron solution to stabilize the austenite phase to room temperature, this is detrimental and needs to be avoided.

1.4 Design of steels

The design of steels is a difficult process and requires a good understanding of how the desired properties of the steel are related to its microstructure. The microstructure in turn depends on both the alloy composition and the thermomechanical processing of the steel. The design of a majority of steels till recently has been based on experience and intuition about the effect of alloying elements and processing conditions (tempering, solution treatment, hot working, cold working, etc.) on the microstructure and thereby on the final properties of the steel. But, developments that started roughly about forty years ago [6–9] have led to significant elimination of the trial and error processes from steel design. For example, the Fe-S53 alloy has been designed solely based on 'computational materials design' [10]. The two most important developments that contributed to the computational design of materials are the CALPHAD [9] and first-principles methods (for an overview of the developments related to steel, see [11]). Both have their respective advantages and disadvantages which are briefly discussed below.

In the CALPHAD (CALculation of PHase Diagrams) method, the free energies of all the phases involved in the phase diagram of the alloy system are obtained by fitting analytical expressions, based on the regular solution model and its modifications (Compound Energy Formalism), to available thermodynamic information (mostly from experiments). These free energies are then used to calculate the equilibrium phase diagram of the alloy system. The fitting parameters in the analytical expressions are modified both to fit available experimental data and also to reproduce the experimentally known regions of the phase diagram faithfully. Therefore, the choice of the fitting parameters requires significant amount of judgment on the part of the investigator. In addition, thermodynamic information about the phases involved is usually available only at high temperatures where equilibrium can be obtained in relatively short times. Another added complication is that it is very difficult to obtain information about metastable phases which do not occur in the equilibrium phase diagram. Although the CALPHAD approach eliminates significant amount of trial and error from the steel design process, it is still based on parametrized fitting to available experimental thermodynamic data. First-principles methods remove the dependence of the free-energies of the phases on available experimental data and thereby remove a number of 'adjustable' parameters from the CALPHAD models.

A computational approach, known as first-principles methods or *ab initio* methods, can be applied to the steel design process and used in tailoring properties of steels. One can obtain complete thermodynamic properties (in addition to a number of other properties) of a phase using first-principles methods with nothing more than the knowledge of its crystal structure and without recourse to any experiments or fitting parameters. This information obtained from first-principles methods can then be used in the CALPHAD method to obtain much more accurate phase diagrams. In addition, since only a knowledge of the crystal structure is required to obtain the thermodynamic data about the phase, even metastable phases can be dealt with ease. Another advantage of first-principles calculations is that although experimentally it is difficult to control, observe and isolate very small precipitate phases to study them, it will be shown how it is rather straightforward to compute their properties from first-principle methods.

One shortcoming of the first-principles methods are that they are much more computationally demanding than the CALPHAD approach. Another one is that they require the help of other statistical thermodynamic methods to transform first-principles energies into thermodynamic quantities like free energies.

1.5 Motivation

As detailed in Sec. 1.3, it is of great importance in TRIP steels and also other low alloy steels to suppress the loss of carbon from the austenite phase. Precipitation of carbides in steel depletes the amount of C available for austenite stabilization and hence it is desirable to suppress the formation of most carbide phases in these steels. In this respect, the most commonly observed carbides in low alloy steels are cementite (Fe_3C), Hägg carbide (Fe_5C_2) and eta-carbide (η-Fe_2C). A convenient approach to curtail the loss of carbon would then be to add alloying elements that suppress the formation of these carbide precipitates. Finding out which alloying elements are most suitable for this suppression of carbide formation is the major focus of this thesis.

1.6 Overview

Along the way to discuss the (de)stabilization of carbide phases that occur in steels (Chap. 6, 7) we first discuss the pure phases of iron (bcc-Fe), cementite, Hägg carbide and η-carbides (Chap. 3). Si is one of the important alloying elements, that is added to TRIP steels to suppress the formation of carbide phases in steels [5]. In light of this, we discuss the effect of Si on the activity and diffusion of C in bcc-Fe (Chap. 5). The dilute solutions of impurity alloying elements in bcc-Fe are discussed in Chap. 4 and the results from this chapter are used later in the calculation of the stability of carbides in Chap. 6 and 7. Theory behind the first-principles methods which are used in the above calculations are explained along with a few important practical considerations in Chap. 2 and can be skipped by people well versed in using plane-wave first-principles codes.

Chapter 2

Density Functional Theory

2.1 Introduction

This chapter introduces the theory behind the most common first-principles methods. It first shows that capturing the exchange and correlation of the electrons to be the most involved issue in all the methods. Then the two most common approaches used to deal with the issue: Hartree-Fock/Post-Hartree-Fock and Density Functional Theory (DFT) are discussed. Finally, DFT implemented using a plane-wave basis along with some practical issues that need to be taken care of when using plane-wave methods are considered.

2.1.1 Approaches to obtain ground state energy

Quantum mechanics states that all possible information about an atomistic system (atom, molecule, solid, surface, etc.) can be obtained from its wavefunction. Although the wavefunction can be obtained by solving the Schrödinger equation (Sec. 2.2) of the system, it is difficult to solve it exactly for an atomistic system containing more than one electron. One important quantity obtained from the wavefunction is the ground state energy E_0 of the system. Two popular approaches to obtain the ground state energy of the system are: the Hartree-Fock (HF)/post-HF, and the Density Functional Theory (DFT) approaches.

The ground state energy E_0 of the system using these two approaches can be written as

$$\begin{aligned} E_0(\Psi_0) &= E_{HF} + E_C^{post-HF} \\ E_0(\rho_0) &= E_{KS} + E_X^{DFT} + E_C^{DFT}. \end{aligned}$$

$E_0(\Psi_0)$ and $E_0(\rho_0)$ show the explicit dependence of the total energy on the ground state wavefunction Ψ_0 and the ground state charge density ρ_0 respectively. E_{HF}

and E_{KS} are the Hartree-Fock and Kohn-Sham energies respectively. E_X is called the exchange energy (Sec. 2.1.2) and arises due to the quantum nature of the electron which gives rise to spin. E_C is the correlation energy (Sec. 2.1.2) and is due to the correlation between electrons in the system because of their charge. Different approaches used to obtain the exchange and correlation energies are mentioned in the superscripts. Exchange energy in the HF method is naturally included in E_{HF} while the correlation energy has to be computed separately. In the DFT approach, both exchange and correlation energy have to be calculated separately. This chapter deals with how Ψ_0, ρ_0 and thereby $E_0(\Psi_0)$ and $E_0(\rho_0)$ are obtained as a sum of the different terms under the two approaches and the various approximations involved. Although we use DFT in this thesis to obtain the ground state energies, both the approaches share a number of concepts that it necessitates a simultaneous discussion of both the approaches. But first, we will briefly discuss each of the energy terms and the computational complexity involved in determining each of them.

E_{HF} and E_{KS} account for a major part of the total energy and are also easy to compute. This leaves us with the other three terms: $E_C^{post-HF}$, E_X^{DFT} and E_C^{DFT}. Approximations, called post HF methods, lead to an increasingly accurate approximation of $E_C^{post-HF}$. But, each of these approximations scales as ($> O(n^4)$), where n is the size of the system, and makes these methods computationally unfeasible as of today except for very small systems with tens of atoms. On the other hand, although it is easy ($\leqslant O(n^3)$) to compute E_X^{DFT} and E_C^{DFT}, and relatively larger systems can be considered, the exact form of these two terms is not known. Also, no apparent way exists to systematically obtain increasingly accurate E_X^{DFT} and E_C^{DFT}.

2.1.2 Exchange and correlation

The fermionic nature of the electrons requires that two electrons cannot exist at the same point in space with the same set of quantum numbers and is known as the Pauli exclusion principle. Mathematically, the Pauli exclusion principle can be accounted for by ensuring that the wavefunction of a set of electrons is antisymmetric under exchange of a pair of electrons. That is to say that the process of swapping an electron for any of the other electron should leave the wavefunction unaltered except for a change of sign (Sec. 2.7, 2.12). Any wavefunction possessing that property will tend to zero (indicating zero probability) as any pair of electrons with the same quantum numbers approach each other. This fermionic nature of electrons leads to exchange.

“A visual impression of the effect of exchange can be obtained by considering the region surrounding a given electron with a particular quantum mechanical spin. If we look at an electron with spin-up, then the Pauli exclusion principle means that other nearby spin-up electrons will be repelled. Spin-down electrons will not be affected since they have a different spin quantum number. Thus our spin-up electron is surrounded by a region which has been depleted of other spin-up electrons. Thus a small positive charge develops in this region (the average electron distribution exactly balances the positive charge of the ion cores, and therefore, this region is relatively depleted of electrons). Similarly, if we had considered a spin-down electron from the start, then we would have found a region depleted of other spin-down electrons. The edge of the electron depleted region is not clearly defined, but nevertheless we call this region the exchange hole.

Ignoring the Pauli exclusion principle generated exchange hole for the moment, we can also visualize a second type of hole in the electron distribution caused by simple electrostatic processes. If we consider the region immediately surrounding any electron (spin is now immaterial) then we should expect to see fewer electrons than the average, simply because of their electrostatic repulsion. Consequently each electron is surrounded by an electron-depleted region known either as the Coulomb hole (because of its origin in the electrostatic interaction) or the correlation hole (because of its origin in the correlated motion of the electrons). Just as in the case of the exchange hole the electron depleted region is slightly positively charged. The effect of the correlation hole is twofold. The first is obviously that the negatively charged electron and its positively charged hole experience a binding force due to simple electrostatics. The second effect is more subtle and arises because any entities which interact with the electron over a length scale larger than the size of the correlation hole will not interact with the bare electron but rather with the electron+correlation hole (which of course has a smaller magnitude charge than the electron alone). Thus any other interaction effects, such as exchange, will tend to be reduced (i.e. screened) by the correlation hole" [12]. The interaction between electrons is repulsive so they will tend to "avoid each other", that is, the probability to find two electrons at the same position or close to each other will be reduced to avoid an energy penalty. These correlations are not limited to short distances, weak correlations over the range of a few nanometers are caused by the same effect and both of these effects turn out to be difficult to describe.

Now that the essential issues of describing an all electronic atomic system have been discussed, the different approaches to obtain accurate description of the ground state are discussed.

2.1.3 Overview

The present chapter is organized as follows: first, the quantum mechanical description of an atomistic system is discussed (Sec. 2.2). The Born-Oppenheimer approximation, common to both approaches and used to decouple the motion of the nuclei and electrons is discussed in Sec. 2.4. The variational principle used in determining optimal one-electron orbitals is discussed in Sec. 2.3. Subsequently, the Hartree method, where the wavefunction is expressed as a product of one-electron orbitals (Sec. 2.5), and the self-consistent field method used to obtain optimal one electron orbitals (Sec. 2.6) are discussed. Spin and indistinguishability of the electrons which leads to 'exchange' is not included in the Hartree approximation. Including these properties of the electron into the one-electron functions using a Slater determinant then leads to the Hartree-Fock equation which we discuss in Sec. 2.8. Although Hartree-Fock equations describe exchange of the electrons exactly they do not include any 'correlation' of the electrons. post-HF methods which are used to include correlation are then discussed in Sec. 2.9. Density Functional Theory (DFT) (Sec. 2.10) is then discussed. Finally, representation of wavefunctions using basis sets (Sec. 2.11) and DFT as implemented using plane wave basis set and associated practical aspects relevant to this thesis are discussed (Sec. 2.12).

As a final remark, for a more detailed discussion of all the concepts discussed in this chapter please refer the following: [12] for an equation-less introduction to many-body theory and DFT, [13] for a clear and accessible introduction to quantum chemistry, [14] for an extensive introduction to computational chemistry and finally to [15] and the classic [16] for an in depth discussion.

2.2 Schrödinger equation

The equations of interest in describing atomistic systems are the time-dependent and time-independent Schrödinger equations which follow rules of quantum mechanics [13]. Specifically, to obtain the allowed energies of an atomistic system, we use the Hamiltonian operator, $\hat{H}$ on Ψ. For a system with n electrons and N nuclei, $\hat{H}$ is given as

$$\hat{H} = -\frac{1}{2}\sum_{i}^{n}\nabla_i^2 - \frac{1}{2}\sum_{\alpha}^{N}\frac{1}{M_\alpha}\nabla_\alpha^2 - \sum_{i\alpha}^{nN}\frac{Z_\alpha}{|r_i - R_\alpha|} - \sum_{ij,i\neq j}^{nn}\frac{1}{|r_i - r_j|} + \sum_{\alpha\beta,\alpha\neq\beta}^{NN}\frac{Z_\alpha Z_\beta}{|R_\alpha - R_\beta|}. \tag{2.1}$$

in atomic units (we use atomic units in this chapter unless mentioned). Solving the time-independent Schrödinger as an eigenvalue equation,

$$\hat{H}\Psi(r,R) = E\Psi(r,R) \tag{2.2}$$

gives us the allowed energies and wavefunctions of the system. The lowest possible energy and the corresponding wavefunction thus obtained are the ground state energy E_0 and the ground state wavefunction Ψ_0 respectively of the system. r and R represent all the electron and nuclear coordinates. Thus, the wavefunction is a function in an $3(n+N)$ dimensional space and hard to solve even numerically except in the simplest of cases, like the hydrogen atom and the H^{2+} molecule where there is only one electron.

2.3 Variational principle

Obviously, the ground-state wave function Ψ_0 and energy E_0 satisfy the Schrödinger equation

$$\hat{H}\Psi_0 = E_0\Psi_0 \tag{2.3}$$

Multiplying Eq. 2.3 from the left by Ψ_0^* and integrating over all space one obtains,

$$E_0 = \frac{\int \Psi_0^* \hat{H} \Psi_0 d\mathbf{r}}{\int \Psi_0^* \Psi_0 d\mathbf{r}} \tag{2.4}$$

The variational theorem states that if we substitute any other function Φ for Ψ_0 in Eq. 2.4 and calculate the corresponding energy according to

$$E_\Phi = \frac{\int \Phi^* \hat{H} \Phi d\mathbf{r}}{\int \Phi^* \Phi d\mathbf{r}}$$

then E_Φ will be greater than the ground state energy E_0. In other words,

$$E_\Phi \geq E_0 \tag{2.5}$$

The variational principle states that we can calculate an upper bound to E_0 by using any trial function we wish. The closer Φ is to Ψ_0 in some sense, the closer E_Φ will be to E_0. We can choose a trial wave function such that it depends upon some arbitrary parameters, α, β, γ, …, called variational parameters. The energy also will depend upon those variational parameters, and Eq. 2.5 would be

$$E_\Phi(\alpha, \beta, \gamma, \dots) \geq E_0$$

Now we can minimize E_Φ with respect to each of the variational parameters and thereby determine the best possible ground-state energy that can be obtained from our trial wave function [13].

The variational principle is used in both the HF/post-HF and DFT approaches to solve the Schrödinger equation to obtain the optimal one-electron orbitals.

2.4 Born-Oppenheimer approximation

One approximation used to make the Schrödinger equation (Eq. 2.2), involving both nuclei and electrons as dependent variables, tractable is the Born-Oppenheimer approximation. It assumes that the motion of the nuclei can be decoupled from the motion of the electrons. The approximation derives from the fact that the nuclei are much heavier than the electrons and that one can assume that electrons instantaneously rearrange around the nuclei. The approximation leads to separate equations for the nuclei and electrons. After the separation, the Schrödinger equation for the electronic system reduces to

$$\left(-\frac{1}{2} \sum_i^n \nabla_i^2 - \sum_{i\alpha}^{nN} \frac{Z_\alpha}{|r_i - R_\alpha|} - \sum_{ij,i\neq j}^{nn} \frac{1}{|r_i - r_j|} \right) \Psi(r;R) = E_{el}(R)\Psi(r;R). \tag{2.6}$$

where $\Psi(r;R)$ implies that the Schrödinger equation depends parametrically on the position of the nuclei. In other words, the electrons are moving in a potential provided by the nuclei. When the positions of the nuclei change, the electrons rearrange instantaneously. The electronic energy E_{el} in turn serves as a potential for the nuclei to move in. For the nuclei, one obtains

$$\left(-\frac{1}{2}\sum_{A}^{N}\frac{1}{M_\alpha}\nabla_\alpha^2 + E_{el}(R) + \sum_{\alpha\beta,\alpha\neq\beta}^{NN}\frac{Z_\alpha Z_\beta}{|R_\alpha - R_\beta|}\right)\Phi(R) = E\Phi(R).$$

The crucial approximation that allowed separation of the equation for the electrons and nuclei was to assume that the action of the nuclear kinetic operator on the electronic wavefunction is zero.

It is interesting to note that the Hamiltonian in Eq. 2.6 contains single particle operators that give the kinetic energy and the interaction of the electrons with the nuclei and the two particle electron-electron interaction term. If not for the presence of the electron-electron interaction term, the wavefunction of the system can be expressed as a product of one-electron wavefunctions (orbitals) and the total energy of the system obtained as a sum of the eigenvalues of each of the individual one-electron Schrödinger equations. Obtaining the exact solution of Eq. 2.6 would be very expensive or rather impossible and it is only solved approximately. The simplest approximate solutions of the electronic Schrödinger's equation are based on the idea that the electrons occupy orbitals. In the approach by Hartree, each electron occupies its own orbital and the total wavefunction is then a product of the single-particle orbitals [13, 17].

2.5 Hartree method

When the only terms in the Hamiltonian are the one-electron kinetic energy and nuclear attraction terms, the operator is 'separable' and may be expressed as

$$\hat{H} = \sum_{i=1}^{N}\hat{h}_i \tag{2.7}$$

where N is the total number of electrons and $\hat{h}_i$ is the one-electron Hamiltonian defined by

$$\hat{h}_i = -\frac{1}{2}\nabla_i^2 - \sum_{k=1}^{M}\frac{Z_k}{r_{ik}} \tag{2.8}$$

where M is the total number of nuclei.

Eigenfunctions of the one-electron Hamiltonian defined by Eq. 2.8 must satisfy the corresponding one-electron Schrödinger equation

$$\hat{h}_i\psi_i = \epsilon_i\psi_i. \tag{2.9}$$

Because the Hamiltonian operator defined by Eq. 2.7 is separable, its many-electron eigenfunctions can be constructed as products of one-electron eigenfunctions. That is

$$\Psi_{HP} = \psi_1\psi_2\ldots\psi_N. \tag{2.10}$$

A wave function of the form of Eq. 2.10 is called a 'Hartree-product' wave function.

The eigenvalue of Ψ is readily found from proving the validity of Eq. 2.10, viz.,

$$\begin{aligned}
\hat{H}\Psi_{HP} &= \hat{H}\psi_1\psi_2\ldots\psi_N \\
&= \sum_{i=1}^{N}\hat{h}_i\psi_1\psi_2\ldots\psi_N \\
&= (\hat{h}_1\psi_1)\psi_2\ldots\psi_N + \psi_1(\hat{h}_2\psi_2)\ldots\psi_N + \ldots + \psi_1\psi_2\ldots(\hat{h}_N\psi_N) \\
&= (\epsilon_1\psi_1)\psi_2\ldots\psi_N + \psi_1(\epsilon_2\psi_2)\ldots\psi_N + \ldots + \psi_1\psi_2\ldots(\epsilon_N\psi_N) \\
&= \sum_{i=1}^{N}\epsilon_i\psi_1\psi_2\ldots\psi_N \\
&= \left(\sum_{i=1}^{N}\epsilon_i\right)\Psi_{HP}
\end{aligned}$$

where repeated application of Eq. 2.9 is used in proving that the energy eigenvalue of the many-electron wave function is simply the sum of the one-electron energy eigenvalues. If every ψ is normalized then $\Psi_{HP}$is also normalized, since $|\Psi_{HP}|^2 = |\psi_1|^2\,|\psi_2|^2\ldots|\psi_N|^2$.

However, the Hamiltonian defined in Eqs. 2.7, 2.8 does not include interelectronic repulsion, computation of which is vexing because it depends not on one electron, but instead on all possible (simultaneous) pairwise interactions. One can think, however, how useful is the Hartree-product wave function in computing energies from the correct Hamiltonian? That is, we wish to find orbitals ψ that minimize $\langle\Psi_{HP}|\hat{H}|\Psi_{HP}\rangle$. By applying the variational principle, one can show that each such orbital ψ_i is an eigenfunction of its own operator $\hat{h}_i$ defined by

$$\hat{h}_i = -\frac{1}{2}\nabla_i^2 - \sum_{k=1}^{M}\frac{Z_k}{r_{ik}} + V_i\{j\} \tag{2.11}$$

where the final term represents an interaction potential with all of the other electrons occupying orbitals {j} and may be computed as

$$V_i\{j\} = \sum_{j\neq i}\int\frac{\rho_j}{r_{ij}}\mathrm{d}\mathbf{r}$$

where ρ_j is the charge (probability) density associated with electron j. The repulsive third term on the r.h.s of Eq. 2.11 is exactly analogous to the attractive second term, except that the nuclei are treated as point charges, while electrons, being treated as wave functions, have their charge spread out, so an integration over all space is necessary.

The Hartree product wavefunction is symmetric (i.e. stays precisely the same after interchange of two fermions) rather than antisymmetric, so the Hartree approach effectively ignores the Pauli exclusion principle. The fermionic nature can be naturally included into the wavefunction when a Slater determinant is used as an approximation for the wavefunction (Sec. 2.12) [14].

2.6 Self-consistent field (SCF) method

Since the point of undertaking the calculation is to determine the individual ψ, one wonders how can they be used in the one-electron Hamiltonians before they are known? This problem is solved using the iterative 'self-consistent field' (SCF) method. In the first step of the SCF process, one guesses the wavefunctions ψ for all of the occupied orbitals and uses these to construct the necessary one-electron operators $\hat{h}$. Solution of each differential Eq. 2.9 provides a new set of ψ, presumably different from the initial guess. So, the one-electron Hamiltonians are formed anew using these presumably more accurate ψ to determine each necessary ρ, and the process is repeated to obtain a still better set of ψ. At some point, the difference between a newly determined set and the immediately preceding set falls below some threshold criterion, and we refer to the final set of ψ as the 'converged' SCF orbitals. The same SCF procedure is also used to obtain optimal one-electron Hartree-Fock and Kohn-Sham orbitals (Sec. 2.5 and Sec. 2.12) [14].

2.7 Electron spin and antisymmetry

All electrons are characterized by a spin quantum number. The electron spin function is an eigenfunction of the operator S_z and has only two eigenvalues, $\pm\hbar/2$; the eigen functions are orthonormal and are typically denoted as α and β. The spin quantum number is a natural consequence of the application of relativistic quantum mechanics to the electron (i.e., accounting for Einstein's theory of relativity in the equation of quantum mechanics), as first shown by Dirac. Another consequence of relativistic quantum mechanics is the Pauli exclusion principle, which is usually stated as the assertion that no two electrons can be characterized by the same set of quantum numbers. Thus, in a given molecular orbital (MO) (which defines all electronic quantum numbers except spin) there are only two possible choices for the remaining quantum number, α or β, and thus only two electrons may be placed in any MO. Also, the Pauli exclusion principle with a single-valued many-particle wavefunction is equivalent to requiring the wavefunction to be antisymmetric,

$$\Psi(1,2,\ldots,i,j\ldots n) = -\Psi(1,2,\ldots,j,i,\ldots n). \tag{2.12}$$

Knowing these aspects of quantum mechanics, if we were to construct a ground-state Hartree-product wave function for a system having two electrons of the same spin, say α, we would write

$$^3\Psi_{HP}(1,2) = \psi_a(1)\alpha(1)\psi_b(2)\alpha(2) \tag{2.13}$$

where the left superscript 3 indicates a triplet electronic state (two electrons spin parallel) and ψ_a and ψ_b are different from one another (since otherwise electrons 1 and 2 would have all identical quantum numbers) and orthonormal. However, the wave function defined by Eq. 2.13 is fundamentally flawed and does not obey the Pauli exclusion principle, that is,

$$\begin{aligned} {}^3\Psi_{HP}(2,1) &= \psi_b(1)\alpha(1)\psi_a(2)\alpha(2) \\ &\neq -{}^3\Psi_{HP}(1,2). \end{aligned}$$

But, a Slater determinant for the triplet ground state given by

$$\begin{aligned} {}^3\Psi_{SD} &= \frac{1}{\sqrt{2}}\begin{vmatrix} \psi_a(1)\alpha(1) & \psi_b(1)\alpha(1) \\ \psi_a(2)\alpha(2) & \psi_b(2)\alpha(2) \end{vmatrix} \\ &= \frac{1}{\sqrt{2}}\left[\psi_a(1)\alpha(1)\psi_b(2)\alpha(2) - \psi_a(2)\alpha(2)\psi_b(1)\alpha(1)\right] \end{aligned} \tag{2.14}$$

does obey the Pauli exclusion principle. The Slater determinant obeys the antisymmetry principle for the fact that the value of a determinant changes sign when two rows (or columns) are interchanged and interchanging two rows is equivalent to interchanging two electrons. The factor $1/\sqrt{2}$ in front is a normalizing factor for the wave function.

Now, let us see how the use of a Slater determinant with the fermionic nature of the electron embedded in it leads to exchange. Consider the energy of the interelectronic repulsion for the wave function of Eq. 2.14. We evaluate this as

$$\begin{aligned} &\int {}^3\Psi_{SD}\frac{1}{r_{12}}{}^3\Psi_{SD}\mathbf{dr_1}\mathrm{d}\omega_1\mathbf{dr_2}\mathrm{d}\omega_2 \\ &= \frac{1}{2}\Big[\int |\psi_a(1)|^2|\alpha(1)|^2\frac{1}{r_{12}}|\psi_b(2)|^2|\alpha(2)|^2\mathbf{dr_1}\mathrm{d}\omega_1\mathbf{dr_2}\mathrm{d}\omega_2 \\ &\quad -2\int |\psi_a(1)||\psi_b(1)||\alpha(1)|^2\frac{1}{r_{12}}|\psi_b(2)||\psi_a(2)||\alpha(2)|^2\mathbf{dr_1}\mathrm{d}\omega_1\mathbf{dr_2}\mathrm{d}\omega_2 \\ &\quad +\int |\psi_a(2)|^2|\alpha(2)|^2\frac{1}{r_{12}}|\psi_b(1)|^2|\alpha(1)|^2\mathbf{dr_1}\mathrm{d}\omega_1\mathbf{dr_2}\mathrm{d}\omega_2\Big] \\ &= \frac{1}{2}\Big[\int |\psi_a(1)|^2\frac{1}{r_{12}}|\psi_b(2)|^2\mathbf{dr_1}\mathbf{dr_2} \\ &\quad -2\int |\psi_a(1)||\psi_b(1)|\frac{1}{r_{12}}|\psi_b(2)||\psi_a(2)|\mathbf{dr_1}\mathbf{dr_2} \\ &\quad +\int |\psi_a(2)|^2\frac{1}{r_{12}}|\psi_b(1)|^2\mathbf{dr_1}\mathbf{dr_2}\Big] \\ &= \frac{1}{2}\left(J_{ab} - 2\int \psi_a(1)\psi_b(1)\frac{1}{r_{12}}\psi_a(2)\psi_b(2)\mathbf{dr_1}\mathbf{dr_2} + J_{ab}\right) \\ &= J_{ab} - K_{ab} \end{aligned} \tag{2.15}$$

where $\mathbf{r}$ and ω represent the spatial and spin coordinates respectively.

Eq. 2.15 indicates that for this wave function the classical Coulomb repulsion between the electron clouds in orbitals a and b is reduced by K_{ab}. This consequence of the Pauli principle reflects the reduced probability of finding two electrons of the same spin close to one another, a 'Fermi hole' is said to surround each electron (also see Sec. 2.1.2).

If we consider the contrasting Slater determinantal wave function formed from different spins

$$\Psi_{SD} = \frac{1}{\sqrt{2}}\left[\psi_a(1)\alpha(1)\psi_b(2)\beta(2) - \psi_a(2)\alpha(2)\psi_b(1)\beta(1)\right]$$

and carry out the same evaluation of interelectronic repulsion we would have

$$\begin{aligned}
&\int \Psi_{SD}\frac{1}{r_{12}}\Psi_{SD}\mathrm{d}\mathbf{r_1}\mathrm{d}\omega_1\mathrm{d}\mathbf{r_2}\mathrm{d}\omega_2 \\
=\;& \frac{1}{2}\left[\int \left|\psi_a(1)\right|^2\left|\alpha(1)\right|^2\frac{1}{r_{12}}\left|\psi_b(2)\right|^2\left|\alpha(2)\right|^2\mathrm{d}\mathbf{r_1}\mathrm{d}\omega_1\mathrm{d}\mathbf{r_2}\mathrm{d}\omega_2\right. \\
& -2\int\left|\psi_a(1)\right|\left|\psi_b(1)\right|\left|\alpha(1)\right|\left|\beta(1)\right|\frac{1}{r_{12}}\left|\psi_b(2)\right|\left|\psi_a(2)\right|\left|\alpha(2)\right|\left|\beta(2)\right|\mathrm{d}\mathbf{r_1}\mathrm{d}\omega_1\mathrm{d}\mathbf{r_2}\mathrm{d}\omega_2 \\
& \left.+\int\left|\psi_a(2)\right|^2\left|\alpha(2)\right|^2\frac{1}{r_{12}}\left|\psi_b(1)\right|^2\left|\beta(1)\right|^2\mathrm{d}\mathbf{r_1}\mathrm{d}\omega_1\mathrm{d}\mathbf{r_2}\mathrm{d}\omega_2\right] \\
=\;& \frac{1}{2}\left[\int\left|\psi_a(1)\right|^2\frac{1}{r_{12}}\left|\psi_b(2)\right|^2\mathrm{d}\mathbf{r_1}\mathrm{d}\mathbf{r_2}\right. \\
& -2\cdot 0 \\
& \left.+\int\left|\psi_a(2)\right|^2\frac{1}{r_{12}}\left|\psi_b(1)\right|^2\mathrm{d}\mathbf{r_1}\mathrm{d}\mathbf{r_2}\right] \\
=\;& \frac{1}{2}\left(J_{ab}+J_{ab}\right) \\
=\;& J_{ab}
\end{aligned} \tag{2.16}$$

The exchange correlation disappears due to the orthogonality of the α and β spin functions, which causes the second integral in the second equality to be zero when integrated over either spin coordinate [14]. Eq. 2.15 and 2.15 show that only the Coulomb correlation term survives when considering electrons of opposite spins, while both the Coulomb and the exchange correlation terms survive when electrons of the same spin are considered.

2.8 Hartree-Fock method

In the Hartree-Fock method a Slater determinant is used as the approximation for the ground state wavefunction. The Slater determinant naturally includes the fermionic nature of electrons. Again as in the Hartree method, using the variational principle, one can show that each HF orbitals can be individually an eigenfunction of its own operator $\hat{f}_i$ defined by the one-electron Fock operator

$$\hat{f}_i = -\frac{1}{2}\nabla_i^2 - \sum_\alpha \frac{Z_\alpha}{r_{i\alpha}} + V_i^{HF}\{j\} \tag{2.17}$$

where the final term, the HF potential, is $2\hat{J}_i - \hat{K}_i$, and the $\hat{J}_i$ and $\hat{K}_i$ operators are defined so as to compute the J_{ij} and K_{ij} integrals previously defined in Eq. 2.15). As can be seen from the presence of both the Coulomb and the exchange operators, the interaction of each electron with the static field of all of the other electrons includes exchange effects on the Coulomb repulsion.

Once again the one-electron equations in Eq. 2.17, 2.18 can be solved self-consistently to obtain the Hartree-Fock orbitals and the Hartree-Fock energy.

$$\hat{f}_i \psi_i(1) = \epsilon_i \psi_i(1), \tag{2.18}$$

Thus we have an eigenvalue equation for the single particle HF orbitals ψ_i. By observing Eq. 2.18 and the form of the operator one can see that in the Hartree term the electrons interact with the potential formed by electron densities of the other electrons. This means that the HF method is a mean field method and the correlations of the electrons are accounted for only partially. Indeed, the electrons with opposite spins have non-zero probability of occupy the same position in space. Although this probability is zero for the electrons with parallel spins, these correlations are still local and non-local correlations are missing from HF completely. This can be understood from the fact that the long range two electron interaction is described as an interaction of two charge densities. It is important to note that we have obtained a set of coupled non-linear equations, i.e., the solution cannot be obtained directly since the operators J and K depend on the solution. The equations need to be solved iteratively starting from some suitable guess for the set of orbitals which is then refined in each step. Since when convergence is reached the new interaction operators are identical to the previous ones, the procedure is called the self-consistent-field (SCF) method.

To summarize, in the Hartree-Fock method, the energy eigenfunctions are assumed to be products of one-electron wavefunctions and the total energy, called the Hartree-Fock energy, E_{HF}, is the sum of the eigenvalues of these one-electron wavefunctions. The repulsion between the electrons is only considered in an average, mean field, manner, i.e., each electron interacts with an average charge density provided by all the other electrons. The effects of electron correlation, beyond that of exchange energy resulting from the anti-symmetrization of the wavefunction, are completely neglected. E_{HF} is the upper limit of the exact non-relativistic ground state electronic energy E_0 and the difference, $E_0 - E_{HF}$ is called the correlation energy [14].

2.9 Post Hartree-Fock methods

For the great majority of systems under study, in particular for excited states and processes such as molecular dissociation reactions, electron correlation is by far the most important. Post Hartree-Fock methods try to describe this electron correlation in a more accurate manner than is possible in the Hartree-Fock method. In the Hartree-Fock method, a single determinant is used to approximate the wavefunction and if we use a variational method to calculate the ground state energy, a restriction to a single determinant to describe the wavefunction is not necessary. Post Hartree-Fock methods which use the variational method, therefore, use multiple determinants to describe the wavefunction. This leads to a much better description of electron correlation than what could be achieved in the Hartree-Fock method.

A variety of post-HF methods exist, namely, Configuration interaction (CI), Coupled cluster (CC), Moller-Plesset perturbation theory (MP2, MP3, MP4, etc.). Each of the methods takes a slightly different approach to describe electron correlation. In the CI method, in addition to the HF determinant, determinants where one or more of the occupied orbitals are replaced by an orbital higher in energy than the highest occupied HF orbital, an "excited" orbital are considered. When determinants containing single and double excitations are added to approximate the total wavefunction, the method is called CISD. If all possible determinants are added (within the given basis set) the approach is called full-CI (FCI) and is exact within the basis set. However, it is usually not possible to perform an FCI calculation because the number of determinants rises quickly with the size of the basis. One of the problems of the CISD approach is that it is not size extensive, that is, the sum of the CISD energies of two species calculated separately differs from the CISD energy of a dimer at infinite separation. The quadratic CISD(T) (QCISD(T)) method can be used to solve the size consistency issue.

Another method that does not suffer the size consistency issue of CI is the CC approach. Here the wavefunction is written $\Psi_{CC} = \exp(T)\Psi_{HF}$, where T is an operator that includes single, double, triple, ... excitations. Because the cost increases quickly with the number of excitations included, single and double excitations are most often used with the effect of triple excitations accounted for perturbatively. The CCSD(T) method has become the 'gold standard' for quantum chemistry reference calculations.

Instead of using the variational approach, a perturbative approach can also be taken starting with the HF Hamiltonian and wavefunction to improve the energy further. The perturbation is chosen to replace the mean field HF electron interaction term with the Coulomb operator. Most often second order energy corrections are evaluated, referred to as second order Moller-Plesset theory (MP2). The MP2 method is used for many reference calculations since it is cheaper than CCSD(T).

The most serious problem of the post-HF methods is the scaling with the basis set size. While MP2 scales as $O(n^5)$, CCSD(T) scales as $O(n^7)$ where n is the number of the basis set functions. Another method which take a completely different approach to evaluation the wavefunction but has a more favorable scaling is the quantum Monte Carlo (QMC) method. In this method, the wavefunction is calculated using a stochastic procedure and as with other stochastic methods, the error decreases only slowly with the length of the simulation. Because of the high cost, these methods are limited to small systems and are often used only to obtain reference data which are then used to assess more approximate approaches.

2.10 Density Functional Theory

Yet another way of describing exchange and correlation effects is the Density Functional Theory (DFT). While exchange is included exactly in HF methods and correlation is added using post-HF methods, DFT has both exchange and correlation included in a single functional[1] and yields one electron orbitals similar to the HF method called the Kohn-Sham orbitals. Unfortunately, the exact form of the exchange-correlation functional is not known.

Since the electronic wavefunction of an n-electron system depends on the $3n$ spatial and n spin coordinates the ground state energy also depends on them. But in 1964, Pierre Hohenberg and Walter Kohn proved that for systems with a nondegenerate ground state, the ground-state energy, wave function, and all other electronic properties are uniquely determined by the ground state electron probability density $\rho_0(x, y, z)$ [18]. Thus E_0 is a functional of ρ_0 and is written $E_0[\rho_0]$ where the square brackets denote a functional relation.

2.10.1 Hohenberg-Kohn theorem

The ground-state electronic wave function of an n-electron system is an eigenfunction of the purely electronic Hamiltonian which, in atomic units, can be written as

$$\hat{H} = -\frac{1}{2}\sum_{i=1}^{n} \nabla_i^2 + \sum_{i=1}^{n} v(\mathbf{r}_i) + \sum_{i,j,i\neq j} \frac{1}{r_{ij}} \tag{2.19}$$

$$v(\mathbf{r}_i) = -\sum_{\alpha} \frac{Z_\alpha}{r_{i\alpha}} \tag{2.20}$$

Using operators, Eq. 2.19 can be written as,

$$\hat{H} = \hat{T} + \hat{V}_{ne} + \hat{V}_{ee} \tag{2.21}$$

It is given as the sum of electronic kinetic-energy terms, electron-nuclear attractions, and electron-electron repulsions. The quantity $v(\mathbf{r}_i)$ is the potential energy of interaction between electron i and the nuclei and depends on the coordinates x_i, y_i, z_i, of electron i and on the nuclear coordinates. $v(\mathbf{r}_i)$ is called the external potential acting on electron i, since it is produced by charges external to the system of electrons. Hohenberg and Kohn also proved that $\rho_0(r)$ determines the external potential and the number of electrons in the system. We will not go into the simple proofs here. To emphasize that $\rho_0(r)$ determines the external potential and also the ground-state energy we write E_0 as $E_v[\rho_0]$. Obviously, $v(\mathbf{r}_i)$ differs for different systems.

Taking the average of Eq. 2.21 for the ground state, we have $E = \overline{T} + \overline{V}_{ne} + \overline{V}_{ee}$, where, for notational convenience, overbars instead of angular brackets have

---

[1] While a function $f(x)$ associates a number with each value of the variable x for which the function f is defined, a functional $F[f]$ is a rule that associates a number with each function f.

been used to denote averages. Each of the average values in this equation is the property of the system determined by the ground-state electronic wave function, which, in turn, is determined by $\rho_0(\mathbf{r})$. Therefore, each of these averages is a functional of ρ_0:

$$E_0 = E_v[\rho_0] = \overline{T}[\rho_0] + \overline{V}_{ne}[\rho_0] + \overline{V}_{ee}[\rho_0].$$

Since $\hat{V}_{Ne} = \sum_i^n v(\mathbf{r}_i)$,

$$\hat{V}_{Ne} = \left\langle \Psi_0 \middle| \sum_i^n v(\mathbf{r}_i) \middle| \Psi_0 \right\rangle = \int \rho_0(\mathbf{r}) v(\mathbf{r})\, \mathrm{d}(\mathbf{r}).$$

Thus, $\hat{V}_{Ne}[\rho_0]$ is known, but the functionals $\overline{T}[\rho_0]$ and $\overline{V}_{ee}[\rho_0]$ are unknown. We have

$$E_0 = \int \rho_0(\mathbf{r}) v(\mathbf{r})\, \mathrm{d}\mathbf{r} + \overline{T}[\rho_0] + \overline{V}_{ee}[\rho_0] = \int \rho_0(\mathbf{r}) v(\mathbf{r})\, \mathrm{d}(\mathbf{r}) + \overline{F}[\rho_0] \tag{2.22}$$

where the functional $F[\rho_0]$, is independent of the external potential. Eq. 2.22 does not provide a practical way to calculate E_0 from ρ_0, because the functional $F[\rho_0]$ is unknown [15].

2.10.2 Hohenberg-Kohn variational theorem

To turn Eq. 2.22 from a formal relation to a practical tool, we need a second theorem proven by Hohenberg and Kohn, and an approach developed by Kohn and Sham [19]. Hohenberg and Kohn proved that for every trial density function $\rho_{tr}(\mathbf{r})$ that satisfies $\int \rho_{tr}(\mathbf{r}) = n$ and $\rho_{tr}(\mathbf{r}) \geq 0$ for all $\mathbf{r}$, the following inequality holds: $E_0 \leq E_v[\rho_{tr}]$. Since $E_0 = E_v[\rho_0]$, the true ground-state electron density minimizes the energy functional $E_v[\rho_{tr}]$. This is exactly similar to the way a normalized ground-state wave function minimizes the variational integral [15].

2.10.3 Kohn-Sham method

The Hohenberg-Kohn theorem says that it is possible in principle to calculate all the ground-state molecular properties from ρ_0, without having to find the molecular wave function. Using the HF and post-HF methods, one first find the wavefunction and then finds ρ by integration. The Hohenberg-Kohn theorem does not tell us *how* to calculate E_0 from ρ_0 without first finding the wave function. Kohn and Sham propose a practical method for finding ρ_0 and for finding E_0 from ρ_0 [19]. The method is capable, in principle, of yielding exact results, but because the equations of the Kohn-Sham (KS) method contain an unknown functional that must be approximated, the KS formulation of DFT yields approximate results.

A fictitious reference system (denoted by the subscript s and often called a *noninteracting system*) of n noninteracting electrons that each experience the same external potential-energy function $v_s(\mathbf{r}_i)$, where $v_s(\mathbf{r}_i)$ is such as to make the ground-state electron probability density $\rho_0(\mathbf{r})$ of the molecule we are interested in; $\rho_s(\mathbf{r}) =$

$\rho_0(\mathbf{r})$. Since Hohenberg and Kohn proved that the ground-state probability density function determines the external potential, once $\rho_s(\mathbf{r})$ is defined for the reference system, the external potential $v_s(\mathbf{r}_i)$ in the reference system is uniquely determined, although we might not know how to actually find it. The electrons do not interact with one another in the reference system, so the Hamiltonian of the reference system can be written as,

$$\hat{H}_s = \sum_i^n \left[-\frac{1}{2}\nabla_i^2 + v_s(\mathbf{r}_i) \right] \equiv \sum_i^n \hat{h}_i^{KS}$$

where $\hat{h}_i^{KS}$ is the one-electron Kohn-Sham Hamiltonian which is exactly similar to the one-electron HF Hamiltonian (Eq. 2.17).

Since the reference system s consists of noninteracting particles, the ground state wavefunction $\Psi_{s,0}$ of the reference system is the Slater determinant of the lowest energy Kohn-Sham spin-orbitals u_i^{KS} of the reference system, where the spatial part $\theta_i^{KS}(\mathbf{r}_i)$ of each spin-orbital is an eigenfunction of the one-electron operator $\hat{h}_i^{KS}$, that is,

$$\Psi_{s,0} = |u_1 u_2 \ldots u_n\rangle\,, \qquad u_i = \theta_i^{KS}(\mathbf{r}_i)\sigma_i \tag{2.23}$$
$$\hat{h}_i^{KS}\theta_i^{KS} = \epsilon_i^{KS}\theta_i^{KS}$$

where σ_i is a spin function (either α or β) and the ϵ_i^{KS}'s are Kohn-Sham orbital energies.

For a closed-shell ground state, the electrons are paired in the Kohn-Sham orbitals, with two electrons of opposite spin having the same Kohn-Sham orbital.

Eq. 2.22 can be written

$$\begin{aligned} E_v[\rho] &= \int \rho(\mathbf{r})v(\mathbf{r})\,d\mathbf{r} + \overline{T}_s[\rho] + \frac{1}{2}\int\int \frac{\rho(\mathbf{r}_1)\rho(\mathbf{r}_2)}{r_{12}} d\mathbf{r}_1 d\mathbf{r}_2 \\ &\quad + \Delta\overline{T}[\rho] + \Delta\overline{V}_{ee}[\rho] \qquad (2.24) \\ E_v[\rho] = E_0[\rho] &= \int \rho(\mathbf{r})v(\mathbf{r})\,d\mathbf{r} + \overline{T}_s[\rho] + \frac{1}{2}\int\int \frac{\rho(\mathbf{r}_1)\rho(\mathbf{r}_2)}{r_{12}} d\mathbf{r}_1 d\mathbf{r}_2 \\ &\quad + E_{xc}[\rho] \qquad (2.25) \end{aligned}$$

where

$$\Delta\overline{T}[\rho] = \overline{T}[\rho] - \overline{T}_s[\rho] \tag{2.26}$$
$$\Delta\overline{V}_{ee}[\rho] = \overline{V}_{ee}[\rho] - \frac{1}{2}\int\int \frac{\rho(\mathbf{r}_1)\rho(\mathbf{r}_2)}{r_{12}} d\mathbf{r}_1 d\mathbf{r}_2 \tag{2.27}$$

$\Delta\overline{T}$ is the difference in the average ground-state electronic kinetic energy between the molecule and the reference system of noninteracting electrons with electron density equal to that in the molecule. The second term on the right hand side of Eq. 2.27 is the classical expression for the electrostatic interelectronic repulsion energy if the electrons were smeared out into a continuous distribution of charge with electron density ρ. The functionals $\Delta\overline{T}$ and $\Delta\overline{V}_{ee}$ are unknown and constitute the exchange-correlation energy functional $E_{xc}[\rho]$. The first three terms in Eq. 2.25 are easy to evaluate from ρ and those include the main contributions to the ground-state energy, but the fourth term although not easy to evaluate accurately is a relatively small term. The key to accurate KS DFT calculation of molecular properties is to get a good approximation to E_{xc}.

E_0 can be evaluated once ρ_0 is known. But the fictitious system of noninteracting electrons defined to have the same electron density as that in the ground state of the molecule: $\rho_s = \rho_0$. The electron probability density of the n-particle system whose wavefunction is given by Eq. 2.23 is given as

$$\rho = \rho_s = \sum_i^n \left|\theta_i^{KS}\right|^2 \tag{2.28}$$

Using Eqs. 2.20, $\overline{T}_s[\rho] = -\frac{1}{2}\left\langle \psi_s \left| \sum_i \nabla_i^2 \right| \psi_s \right\rangle$ and 2.28 in Eq. 2.25 the ground state energy will be

$$\begin{aligned} E_0 \quad &= \quad -\sum_\alpha Z_\alpha \int \frac{\rho(\mathbf{r})}{r_{1\alpha}} d\mathbf{r}_1 - \frac{1}{2}\sum_i^n \left\langle \theta_i^{KS}(1) \left| \sum_i \nabla_i^2 \right| \theta_i^{KS}(1) \right\rangle \\ &\quad + \frac{1}{2}\int\int \frac{\rho(\mathbf{r}_1)\rho(\mathbf{r}_2)}{r_{12}} d\mathbf{r}_1 d\mathbf{r}_2 + E_{xc}[\rho] \end{aligned} \tag{2.29}$$

We can therefore find $E_0$from ρ if we can find the KS orbitals θ_i^{KS} and if we know the functional E_{xc}.

The Kohn-Sham orbitals are found as follows. The Hohenberg-Kohn variational theorem tells us that we can find the ground-state energy by varying ρ (subject to the constraint $\int \rho d\mathbf{r} = n$) so as to minimize the functional $E_v[\rho]$. Equivalently, instead of varying ρ, we can vary the KS orbitals θ_i^{KS}, which determine ρ from Eq. 2.28. Just as we showed that the orthonormal orbitals that minimize the Hartree-Fock expression for the molecular energy satisfy the Fock equation (Eq. 2.18), one can show that the Kohn-Sham orbitals that minimize the expression Eq. 2.29 for the molecular ground-state energy satisfy,

$$\left[-\frac{1}{2}\nabla_1^2 - \sum_\alpha \frac{Z_\alpha}{r_{1\alpha}} + \int \frac{\rho(\mathbf{r}_2)}{r_{12}} d\mathbf{r}_2 + v_{xc}(1)\right]\theta_i^{KS}(1) = \epsilon_i^{KS}\theta_i^{KS}(1) \tag{2.30}$$

$$\left[-\frac{1}{2}\nabla_1^2 + v_s(1)\right]\theta_i^{KS}(1) = \epsilon_i^{KS}\theta_i^{KS}(1) \tag{2.31}$$

$$\hat{h}(1)\theta_i^{KS}(1) = \epsilon_i^{KS}\theta_i^{KS}(1) \tag{2.32}$$

where the exchange-correlation potential v_{xc} is given as the function derivative of the exchange-correlation energy E_{xc}:

$$v_{xc}(\mathbf{r}) = \frac{\delta E_{xc}[\rho(\mathbf{r})]}{\delta\rho(\mathbf{r})}$$

The one-electron Kohn-Sham operator $\hat{h}^{KS}(1)$ in Eq. 2.32 is the same as the Fock operator (Eq. 2.18) in the Hartree-Fock equations except that the exchange operators $\hat{k}$ in the Fock operator are replaced by v_{xc}, which handles the effects of both exchange (antisymmetry) and electron correlation.

There is only one problem in using the Kohn-Sham method to find ρ and E_0. No one knows what the correct functional $E_{xc}[\rho]$ is. Therefore, both E_{xc} in the energy expression Eq. 2.29 and v_{xc} in Eq. 2.30 are unknown. Various approximations are used for both of them which we will discuss shortly.

The exchange-correlation energy E_{xc}(Eq. 2.25) contains the following components: the kinetic correlation energy (the term ΔT in Eq. 2.25, which is the difference in $\overline{T}$ for the real molecule and the reference system of noninteracting electrons), the exchange energy (which arises from the antisymmetry requirement), the Coulombic correlation energy (which is associated with interelectronic repulsions), and a self-interaction correction (SIC). The SIC arises from the fact that the classical charge-cloud electrostatic-repulsion expression $-\frac{1}{2}\int\int\frac{\rho(\mathbf{r}_1)\rho(\mathbf{r}_2)}{r_{12}}d\mathbf{r}_1 d\mathbf{r}_2$ erroneously allows the portion of ρ in $d\mathbf{r}_1$ that comes from the smeared-out part of a particular electron to interact with the charge contributions of that same electron to ρ throughout space. In reality, an electron does not interact with itself. Note that for a one-electron molecule, there is no interelectronic repulsion, but the expression $-\frac{1}{2}\int\int\frac{\rho(\mathbf{r}_1)\rho(\mathbf{r}_2)}{r_{12}}d\mathbf{r}_1 d\mathbf{r}_2$ erroneously gives an interelectronic repulsion [15].

2.10.4 Exchange-correlation functionals

The exchange-correlation energy can be written as sum of the exchange and the correlation energies,

$$E_{xc}[\rho] = E_x[\rho] + E_c[\rho].$$

A variety of approximations have been used to obtain the exchange-correlation energy. These exchange-correlation functionals can be classified as LDA, GGA, meta-GGA and hybrid functionals depending on their dependence on one or more of the quantities: local density (ρ) , gradient of the local density ($\nabla\rho$), the Laplacian of the density ($\nabla^2\rho$) and the kinetic energy density $\tau = \sum_i(\nabla\phi_i^{KS})^2$. In the Local Density Approximation (LDA), E_{xc} depends only on ρ. In the Generalized Gradient Approximation (GGA), in addition to ρ, E_{xc} also depends on the gradient of the electron density. E_{xc} in meta-GGA's depends on all the quantities: ρ, $\nabla\rho$, $\nabla^2\rho$ and τ. Hybrid functionals are GGA functionals with a fraction of the exact HF-exchange. This dependence can be summarized as,

$$\begin{aligned}
E_{xc}^{LDA}(r) &= E_{xc}^{LDA}[\rho] \\
E_{xc}^{GGA}(r) &= E_{xc}^{GGA}[\rho, \nabla\rho] \\
E_{xc}^{meta-GGA}(r) &= E_{xc}^{GGA}[\rho, \nabla\rho, \nabla^2\rho, \tau] \\
E_{xc}^{hybrid-GGA}(r) &= a_x E_{HF}^{exact} + E_{xc}^{GGA}[\rho, \nabla\rho]
\end{aligned}$$

No approximation of E_{xc} is able to describe all chemical systems and all properties accurately. For example, B3LYP, a popular hybrid functional, describes molecules well [20, 21], but fails badly at the description of solids [22]. In contrast, PBE [23, 24], which describes periodic systems like solids and surfaces reasonably well, is not able to describe molecular properties as well as B3LYP [20]. We will restrict ourselves to the case of solids below.

Coming to properties, LDA tends to overestimate bond strengths in solids and GGA underestimates them. In LDA, the calculated lattice constants are too small and cohesive energies are overestimated by about 1 %. PBE, a GGA functional, corrects the overbinding of LDA, and gives properties with similar errors but opposite to those from LDA. Other equilibrium properties that are sensitive to lattice constants such as bulk moduli, phonon frequencies, and magnetic moments are also sometimes over-corrected by GGA. Both LDA and GGA underestimate energy gaps in semiconductors and insulators [22].

Important for the present work, GGA produces the correct ground state for magnetic transition metals; the LDA fails quite badly in this regard [25]. LDA incorrectly predicts the hexagonal close-packed nonmagnetic structure of Fe to be the most stable [26, 27] ground state crystal structure, but GGA correctly predicts the ferromagnetic body-centered structure as the ground state [28]. Furthermore, LDA predicts body-centered cubic Cr to be non-magnetic, but GGA correctly predicts it to be antiferromagnetic [29].

The search for the perfect exchange-correlation functional is far from over, and new functionals are still being developed [30]. Treating non-local dispersion interactions, which are important in describing materials like hydrocarbons, noble gases, proteins, DNA, etc., has been a problem till recently for all the exchange-correlation functionals mentioned till now. Recently, a number of dispersion-corrected exchange-correlation functionals have been introduced [31]. More information about various exchange-correlation functionals and the accuracy of their description of different material systems can be found in Ref. [20–22].

2.11 Basis sets

Basis sets are used to mathematically represent wavefunctions. The concept of a basis sets can be understood with the help of a simple analogy. In Fourier series expansions we use $a_0/2 + \sum_{n=1}^{\infty} a_n \sin nx + \sum_{n=1}^{\infty} b_n \cos nx$ to represent any periodic functions; $\sin nx$ and $\cos nx$ terms being basis functions of the expansion (Appendix A). The accuracy with which the expansion represents the original function depends on the features of the original function and also on how many terms are included in the expansion. Given a fixed number of terms in the expansion, more 'smoother' functions can be described more accurately compared to functions with discontinuities and jumps. Here, the use of sin and cos terms is motivated by the periodicity of the function that is being described.

Similarly, a wave function is represented by a basis set and different basis sets can be used to represent the wavefunction. The choice is usually directed by the system under consideration. It is natural for the wave function of a molecular system to be expressed in terms of molecular orbital basis functions each of which is expressed in terms of atomic orbital basis functions. This is called the Linear Combination of Atomic Orbitals-Molecular Orbitals (LCAO-MO) method. Similarly, it is natural for solid state systems like solids and surfaces, with inherent periodicity, to be expressed in terms of plane waves. The plane-wave method, which is mostly used in solid-state calculations, utilizes the periodicity of the lattice and electronic orbitals are expanded using a set of functions $\exp^{iG\cdot r}$, where G is a vector of the reciprocal lattice. After a short discussion of both the basis sets (Sec. 2.11.1 and 2.11.2), the plane-wave basis is discussed in detail (Sec. 2.12).

2.11.1 Localized basis sets

The LCAO-MO method uses localized basis sets. For example, a single hydrogen atom can be represented by a hydrogen atom-like (1s) function called a Slater-type orbital (STO). Although, a single hydrogen atom can be adequately represented by a single STO, a hydrogen molecule needs more than two 1s STO's; to represent the bonding and anti-bonding orbitals. Hence, more basis set functions are added so that orbitals can be accurately represented. In the hydrogen molecule example, adding 2p functions helps in describing the bonding more accurately because of their directional nature. Thus it is important to choose a large enough basis set to obtain reliable results. In modern quantum chemistry programs, STOs are not used anymore because the integrals resulting in the secular determinants are difficult to evaluate. This difficulty is overcome by the use of Gaussian type orbitals (GTO). One issue with localized basis sets is the basis set superposition error (BSSE). Binding energy of a dimer is generally overestimated due to BSSE. BSSE occurs since upon formation of the dimer (A+B) the basis functions on species B represent an additional optimization space for orbitals of species A which lowers the total energy and results in overestimation. Also, it is difficult to represent an electron, unless explicitly specified, detached for an atom as the localized basis does not exist in vacuum. While it is advisable to use localized basis with slow decay (diffuse) functions for molecular calculations, in condensed phase these cause a poor conditionality of the overlap matrix and often lead to numerical instabilities [17].

2.11.2 Plane waves

The issues above can be avoided by the use of a plane wave basis set. Plane waves arise naturally in calculations involving solids as Bloch functions ($\exp^{iG\cdot r}$) are the eigen functions of a system with a periodic potential. Thus we are basically using the Fourier representation of the orbitals and storing the Fourier coefficients. The size of the basis is therefore controlled by the highest momentum of the plane wave included in the basis. The main advantages of using a plane wave basis are: one, they are all orthogonal and thus several terms in the electronic Hamiltonian are simple to evaluate. Two, BSSE is avoided and the complete cell is described in a similar manner. However, description of molecules is very inefficient as a lot of effort is spent in describing vacuum. Another important problem that arises due to the use of plane waves is the description of the rapid oscillations of the electronic orbitals close to the atomic nuclei. Accurate description of these rapid oscillations would require very high plane-wave cut-offs. Various approaches are used to avoid the description of these fast oscillations while still retaining the efficiency of plane-waves (Sec. 2.12.5). We will now discuss planewave DFT in detail.

2.12 Planewave DFT

In this section we discuss the implementation of DFT in a plane-wave approach. Most of the discussion below is based on Sec. II of Ref. [32].

2.12.1 Periodicity

Bloch's theorem (Sec. 2.12.2) is applicable only to periodic systems. A bulk crystal can obviously be represented by a periodic replication of the primitive cell in space (Fig. 2.1). At the other extreme, a molecule which has no inherent periodicity can be made to have 'pseudo' periodicity. This can be achieved by inserting the molecule in a 'box' and replicating the box in three dimensional space. Since we want to calculate the properties of the isolated molecule and not a 'crystal' of molecules, we have to make sure that the box is big enough that the molecules in neighboring cells do not interact with each other (Fig. 2.1). Defects and surface can similarly be periodically represented.

A point defect (vacancy, substitutional impurity) can be modeled by inserting it into big enough bulk crystal and replicating it in space. Again, similar to the case of molecules, since we want to calculate the properties of an isolated defect, the cell should be chosen big enough such that neighboring defects do not interact with each other (Fig. 2.1). In this case the energy per unit cell of a crystal containing an array of defects is calculated, rather than the energy of a crystal containing a single defect. The independence of defects in neighboring cells can be checked by increasing the volume of the supercell until the computed defect energy has converged. It can then be assumed that defects in neighboring unit cells no longer interact.

Similarly, a surface may have periodicity in the plane of the surface, but it cannot have periodicity perpendicular the the surface. The supercell contains a crystal slab and a vacuum region (Fig. 2.1). The supercell is repeated over all space, so the total energy of an array of crystal slabs is calculated. To ensure that the results of the calculation accurately represent an isolated surface, the vacuum regions must be wide enough so that faces of adjacent crystal slabs do not interact across the vacuum region, and the crystal slab must be thick enough so that the two surfaces of each crystal slab do not interact through the bulk crystal.

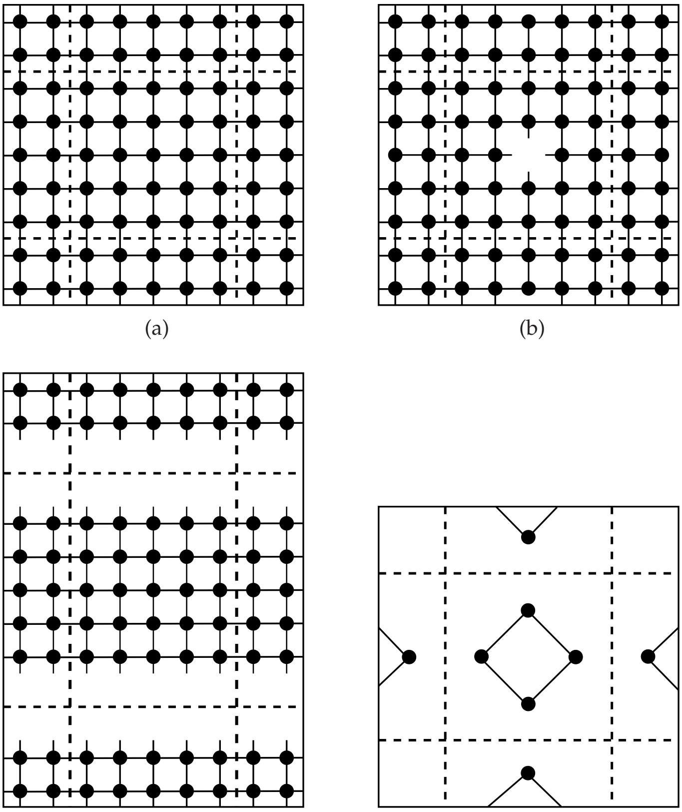

(a) (b)

(c) (d)

Figure 2.1: Schematic illustrations of supercell geometries: bulk crystal (a), point defect (vacancy) (b), surface (c), molecule (d). The supercell area is enclosed by dashed lines.

2.12.2 Bloch's theorem

Bloch's theorem states that the wave function of an electron in a periodic potential (from a crystal) can be written as the product of a cell-periodic part and a wavelike part [32–34],

$$\psi_i(\mathbf{r}) = \exp(i\mathbf{k}\cdot\mathbf{r}) f_i(\mathbf{r}).$$

The cell-periodic part of the wave function can be expanded using a basis set consisting of a discrete set of plane waves whose wave vectors are reciprocal lattice vectors of the crystal,

$$f_i(\mathbf{r}) = \sum_{\mathbf{G}} c_{i,\mathbf{G}} \exp(i\mathbf{G}\cdot\mathbf{r}),$$

where the reciprocal lattice vectors $\mathbf{G}$ are defined by $\mathbf{G}\cdot\mathbf{l} = 2\pi m$ for all $\mathbf{l}$ where $\mathbf{l}$ is a lattice vector of the crystal and m in an integer. Therefore each electronic wave function can be written as a sum of plane waves,

$$\psi_i(\mathbf{r}) = \sum_{\mathbf{G}} c_{i,\mathbf{k}+\mathbf{G}} \exp[i(\mathbf{k}+\mathbf{G})\cdot\mathbf{r}].$$

2.12.3 Brillouin zone integration

Due to periodicity of the crystal structure, electronic states are allowed only at a set of **k** points determined by the boundary conditions that apply to the bulk solid. The density of allowed **k** points is proportional to the volume of the solid. The infinite number of electrons in the solid are accounted for by an infinite number of **k** points, and only a finite number of electronic states are occupied at each **k** point. Bloch's theorem changes the problem of calculating an infinite number of electronic wave functions to one of calculating a finite number of electronic wave functions at an infinite number of **k** points. The occupied states at each **k** point contribute to the electronic potential in the bulk solid so that, in principle, an infinite number of calculations are needed to compute this potential. However, the electronic wave functions at **k** points that are very close together will be almost identical. Hence it is possible to represent the electronic wave functions over a region of **k** space by the wave functions at a single **k** point. In this case the electronic states at only a finite number of **k** points are required to calculate the electronic potential and hence determine the total energy of the solid [32].

Using a plane-wave basis, the average property $\overline{g}$ of the system can be written as,

$$\overline{g} = \frac{V_{cell}}{(2\pi)^3} \int_{BZ} g(\mathbf{k})\, \mathrm{d}\mathbf{k}$$

where BZ is the Brillouin zone and **k** is a reciprocal lattice vector. The integral is defined over all possible values of **k** in the Brillouin zone.

Computationally, the above integral is evaluated on a grid of k-points which are chosen in such a way that an efficient convergence of the desired property is obtained as a function of the k-point grid density. A special set of k-points called the Monhkhort-Pack grid [35] is usually employed in a plane wave calculation [2].

---

[2] Properties such as the density of states (DOS) are non-analytical (spectral) functions and hence

2.12.4 Energy cut-off

Bloch's theorem states that the electronic wave function at each $\mathbf{k}$ point can be expanded in terms of a discrete plane-wave basis set. In principle, an infinite plane-wave basis set is required to expand the electronic wave functions. The coefficients $c_{i,\mathbf{k}+\mathbf{G}}$ for the plane waves with small kinetic energy $(\hbar^2/2m)\,|\mathbf{k}+\mathbf{G}|^2$ are typically more important (because of the PAW approximation, Sec. 2.12.5) than those with large kinetic energy. Thus the plane-wave basis set can be truncated to include only plane waves that have kinetic energies less than a particular cutoff energy. If a continuum of plane-wave basis states were required to expand each electronic wave function, the basis set would be infinitely large no matter how small the cutoff energy. Application of the Bloch's theorem allows the electronic wave functions to be expanded the terms of discrete set of plane waves. Introduction of an energy cutoff to the discrete plane-wave basis set produces a finite basis set [32].

2.12.5 Pseudopotentials

Most of the ordinary properties (bonding, reactivity) of a chemical system are dictated by the valence electrons of the constituent atoms; the core electrons not playing an important role. Also, closer to the nuclei, where core electrons are located, the wave function varies rapidly. Accurate representation of these rapid oscillations requires a much larger set of plane waves with high energy cut-offs. This can again be understood easily with reference to a Fourier series expansion. Relatively larger basis sets are required to represent sharply peaked and/or rapidly varying functions than to represent functions with no peaks and/or slowly varying. For example, the number of nodes in hydrogen orbitals increase in the order: 1s < 2p < 2s < 3d < 3p < 3s . . . and thus they would require progressively larger basis sets to be represented accurately.

Since core electrons do not play a major role in the properties of the system and in addition are much harder to describe accurately, it would be beneficial to mimic their behavior while avoiding the associated complexities in their representation. In other words, if we are able to devise a method that just keeps the properties of the valence electron density while replacing the core density with a smoothly varying nodeless function, we will able to calculate the properties of interest with a much smaller basis. This is exactly what pseudopotentials have been designed for.

The pseudopotential is an effective potential constructed to replace the atomic all-electron potential (full-potential) such that the core states are eliminated and the valence electrons are described by nodeless 'pseudo' wavefunctions. In this approach only the chemically active valence electrons are dealt with explicitly, while the core electrons are 'frozen', being considered together with the nuclei as

---

integration schemes employed to integrate smooth functions are not of much use when directly applied. To overcome this the property is smoothened using Gaussian or Lorentzian smoothening. This smoothened function can then be easily integrated with 1st, 2nd or higher order integration methods.

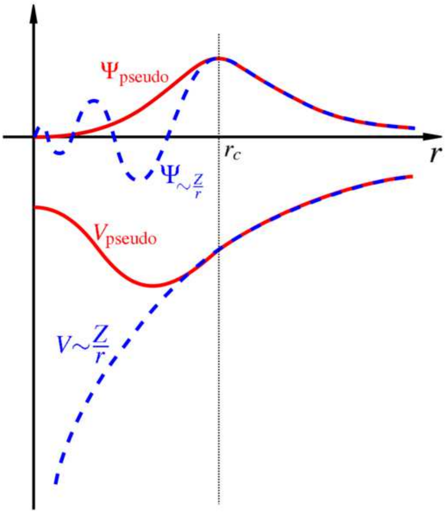

Figure 2.2: Illustration of a pseudopotential.Comparison of a wavefunction in the Coulomb potential of the nucleus (blue) to the one in the pseudopotential (red). The real and the pseudo wavefunction and potentials match above a certain cutoff radius r_c.

rigid non-polarizable ion cores. Norm-conserving pseudopotentials [36] are derived from an atomic reference state, requiring that the pseudo- and all-electron valence eigenstates have the same energies and amplitude (and thus density) outside a chosen core cutoff radius r_c. Pseudopotentials with larger cutoff radius are said to be softer, that is more rapidly convergent, but at the same time less transferable, that is less accurate to reproduce realistic features in different environments. Norm-conserving pseudopotentials enforce the condition that, outside of a cutoff radius, the norm of each pseudo-wavefunction be identical to its corresponding all-electron wavefunction. Ultrasoft pseudopotentials [37] relax the norm-conserving constraint to reduce the basis-set size further. Another related technique is the projector augmented wave (PAW) method [38]. The PAW method retains the nodal structure of the core while still retaining the computational efficiency of a pseudopotential.

Since in this thesis we use a planewave basis along with a frozen core PAW approximation, we restrict ourselves to the calculation of properties under this approximation.

2.12.6 Smearing

One last thing of practical importance are the smearing methods. The numerical evaluation of integrals converges easily for continuous functions while it does not for functions which are discontinuous. Especially for a metal, the Brillouin zone can be divided into regions that are occupied and unoccupied by electrons.

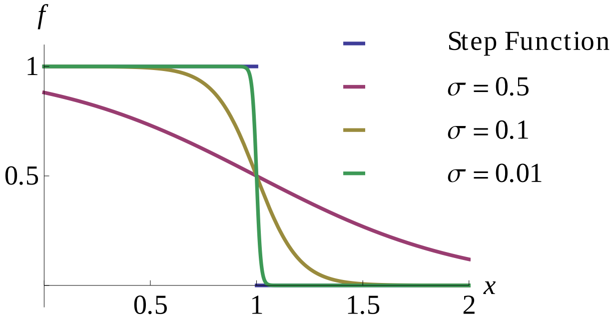

Figure 2.3: Fermi-Dirac function with $k_0 = 1$ and several values of σ.

The surface in k space that separates these two regions is called the Fermi surface. From the point of view of calculating integrals in k space, this is a significant complication because the functions that are integrated change discontinuously from nonzero values to zero at the Fermi surface. If no special efforts are made in calculating these integrals, very large numbers of k points are needed to get well-converged results.

Two methods are popular to overcome this difficulty: the tetrahedron method and the smearing method. In the tetrahedron method, discrete set of k points are used to define a set of tetrahedra that fill reciprocal space and the function being integrated is defined at every point in the tetrahedron using interpolation. Once the interpolation is complete, the function to be integrated has a simple form at all positions in k space and the integral can now be evaluated using the entire space, and not the original discrete points. Blöchl developed interpolation methods that go beyond a simple linear interpolation and these are the methods that are most widely used. In the smearing methods, the function being integrated is forced to be continuous by 'smearing' out the discontinuity. An example of a smearing function is the Fermi-Dirac function:

$$f\left(\frac{k-k_0}{\sigma}\right) = \left[\exp\left(\frac{k-k_0}{\sigma}\right)+1\right]^{-1}.$$

This changes a discontinuous step function into a function without a discontinuity. As $\sigma \to 0$, the above function approaches the step function. One of the widely used smearing method was developed by Methfessel and Paxton [39]. Their method uses expressions for the smearing functions that are more complicated than the simple Fermi-Dirac function above, but are still characterized by a single parameter, σ.

2.12.7 Convergence

For a given exchange-correlation functional, the ground state energy obtained by solving the Kohn-Sham equations should be numerically converged. When using plane-wave DFT, numerical convergence should be achieved with respect to all the following: plane-wave energy, density of the k-point grid, self-consistency cycle, and ionic relaxation.

The energy cutoff for the plane wave energy and the density of the k-point grid can be increased gradually to check if convergence in total energy is achieved to ‘desired accuracy.’ The ‘desired accuracy’ depends on the property being studied. If one is interested in the phase stability of phases which differ by less than 10 meV in energies, we need to achieve a convergence of at least 1 meV or better. One needs to use much denser k-point grids for metals compared to insulators and semi-conductors. Usually a k-point density of about 0.25 Å^{-1} along each of the reciprocal lattice vectors gives a good description of properties for metals while a k-point density of 0.5 Å^{-1} gives a good description of the properties for insulators and semi-conductors. Relatively high plane-wave energy cutoffs are required when elements from the first and second row of the periodic are part of the system under consideration. A cut-off of about 400 eV is generally sufficient for calculation of most properties involving these elements.

Finally, only calculations employing the same energy cutoff, k-point density, smearing methods can be compared. Differences in energies of calculations employing different energy cutoffs, k-point densities, or smearing methods will lead to wrong results.

2.13 Temperature dependence of properties

The calculation of a number of properties at 0 K is rather straightforward. But calculating the same properties as a function of temperature is relatively more involved. For example, calculation of structural parameters (crystal lattice parameters, molecular structure) is relatively easy while the calculation of thermal expansion coefficients are slightly more difficult.

Structural, electronic, thermodynamic and mechanical properties of pure phases can also vary as a function of temperature and pressure. For solid phases, such as the ones that we are interested in, the change in properties as a function of pressure is negligible and also irrelevant in the case of steels as most of the thermal and mechanical processing is done at atmospheric pressure. Hence, we would be interested in the change of these properties as a function of temperature.

Now that we have discussed all the essential details required to understand a first-principles calculation, in the next chapter we will calculate a number of propertis of the pure phases: bcc-Fe, Fe_3C, Fe_5C_2 and η-Fe_2C.

Chapter 3

Iron, Cementite (Fe_3C), Hägg carbide (Fe_5C_2) and η-Fe_2C

3.1 Introduction

3.1.1 Overview

In this chapter the properties of the pure phases, bcc-iron and the iron carbides: Fe_3C, Fe_5C_2, and η-Fe_2C, are studied. The focus will be on the structural (crystal, magnetic), electronic (density of states), thermodynamic (formation energy, vibrational free energy, heat capacity, Debye temperature) and mechanical properties (elastic moduli, elastic tensors) of these phases. But first, we will discuss what is already known about them experimentally and theoretically.

3.1.2 Experiments

3.1.2.1 Iron

Pure iron at ambient pressure and temperature is a body centered cubic ferromagnetic (FM) solid usually know as ferrite or the α phase. It exists in this state from 0 K all the way up to 1043 K where it magnetically disorders into a paramagnetic bcc state. At 1184 K the paramagnetic bcc state transforms into a paramagnetic fcc state, referred to as austenite or the γ phase. At a still higher temperature of 1665 K the paramagnetic bcc state reappears, denoted as the δ phase before melting at 1811 K into a paramagnetic liquid. In steel processing we usually are never over 1500 K and hence we consider the phases relevant below this temperature, namely ferrite and austenite.

Most elemental solids are close packed, but Fe is one of the few exceptions which occurs in a more open bcc structure. The stabilization of the bcc structure has been attributed to its magnetism [1].

3.1.2.2 Iron carbides

Cementite is the most common metastable carbide in steel. At room temperature it is ferromagnetic (FM) with a Curie temperature, T_c, of about 483 K [40, 41]. Although cementite is the most common carbide observed in steels, a sequence of precipitations precede the final formation of cementite. Roughly, with increasing temperature the carbides appear to precipitate in the order: η-Fe_2C, Fe_5C_2 and Fe_3C [3, 4]; the appearance of ϵ-Fe_2C precedes η-Fe_2C.

Experimentally, it was found that η-Fe_2C forms first in quenched steels at temperatures between 370 and 470 K [42, 43]. But, it was also noticed that ϵ-Fe_2C is the only carbide forming up to 520 K and forms along with cementite till 600 K and that it acts as a precursor for the formation of Fe_5C_2 [44, 45]. A long aging study at 300 K followed by a brief 405 K anneal showed the presence of both η-Fe_2C and ϵ-Fe_2C [46]. ϵ-Fe_2C is a non-stoichiometric carbon deficient structure of η-Fe_2C. It was recently shown that ϵ-Fe_2C is only slightly more unstable than η-Fe_2C and that it can relax to the latter structure [4]. Above 720 K it has been observed that Fe_3C forms exclusively [42, 43]. Both kinetic and thermodynamic factors could be responsible for these observations. It is interesting that the precipitation sequence can be altered by the application of a magnetic field thereby showing that the magnetic free energy plays an important role in the stabilization of the carbide phases [4, 47, 48]. But, the predominance of each of the carbides in a definite temperature range has been attributed to the lowering of its free energy (and hence stabilization) with temperature [4].

Apart from playing an important role in steels, cementite also displays many interesting properties, such as INVAR behavior [49], and is also suspected to be a major component of the earth's core [50]. Cementite, Hägg carbide and η-Fe_2C along with Fe_7C_3, ϵ-$Fe_{2.2}C$ also form during the Fischer-Tropsch process [51] (and references therein).

3.1.3 Theory

The first attempt at describing the properties of iron was done way back in 1978 by Moruzzi et al. [52]. The local spin density approximation (LSDA) that they used wrongly indicated fcc-Fe to be more stable than bcc-Fe. The description of the properties of iron improved by a great measure by the use of the generalized gradient approximation (GGA) in place of the LSDA. At present, the electronic, magnetic and thermodynamic properties of bcc-Fe can be described very well using first principles calculations. But, the description of the paramagnetic state of iron is still problematic. For instance, a proper theoretical understanding of the fcc-Fe magnetic state is still lacking.

Electronic, structural and magnetic properties of pure cementite were described in a number of previous communications [3, 53–55]. Furthermore, there are detailed studies of thermodynamic properties of pure cementite [48, 56], elastic properties [57–60], point defects and possible C diffusion paths [55].

Electronic, magnetic and structural properties of Fe_3C, Fe_5C_2 and η-Fe_2C have been reported [3]. Formation enthalpies [3, 61], surface properties [62], thermodynamic properties along with formation enthalpies [4] of Fe_5C_2 have also been described. Comparable work, excluding the surface properties, has been done on η-Fe_2C [3, 4, 63].

3.2 Crystal and magnetic structure

While the C in Fe_3C, Fe_5C_2 and Fe_7C_3 has a trigonal prismatic coordination of Fe atoms (Fig. 3.1), the C in η-Fe_2C (Fig. 3.1) along with ϵ-$Fe_{2.2}C$, ferritic, martensitic and austenitic Fe-C solid solutions has an octahedral coordination of Fe atoms.

Fe_3C crystallizes in an orthorhombic unit cell with 16 atoms [64]. The structure of cementite can be thought of as being derived from a hexagonal close-packed array of Fe atoms. The close-packed sheets are, however, not flat but 'pleated'. The pleated close-packed sheets lie in the [100] direction [49]. The structure is related to the structures of ϵ-iron and the ϵ-carbide [64]. The C atoms occupy a four fold Wyckoff 4c site and are coordinated by six Fe atoms in a fairly regular trigonal prism. The Fe atoms occupy positions called 'general and special positions'; Wyckoff sites 8d and 4c respectively.

The crystal structure of Hägg carbide is still under debate; a monoclinic [65–70] or a pseudo-monoclinic [71, 72] structure are suggested as alternatives. But first-principles calculations suggest that both the structures are energetically equivalent [71]. We consider the monoclinic variant of the crystal structure in this work as it has slightly higher symmetry than the pseudo-monoclinic crystal structure. The monoclinic crystal structure has 28 atoms in the unit cell. In the Hägg carbide, C atoms occupy an 8f position while Fe atoms occupy the Wyckoff positions 8f, 8f and 4e.

η-Fe_2C also crystallizes in the orthorhombic unitcell [45, 73–75] with 6 atoms. In η-Fe_2C the C and Fe occupy the Wyckoff sites 2a and 4g respectively. The unit cells of bcc-Fe and the carbides are shown in Fig. 3.1.

The lattice parameters, fractional coordinates of bcc-Fe along with those of the carbides are given in Table 3.1. As can be seen, the lattice parameters agree well with experimental results and previous first-principles results. Although GGA is known to underbind most elemental solids, in the case of bcc-Fe it gives a slightly smaller lattice parameter compared to experiments. This tendency is further confirmed by the slightly smaller lattice parameters obtained from GGA for the carbides compared to experiments.[1]

The total magnetization of the carbides decreases with increasing fraction of C in the carbide and the magnetic moment on the Fe atoms also decreases with increasing number of C nearest neighbors. The magnetic moment per Fe atom and

---

[1] The Birch Murnaghan equation of state was used to fit to the energy vs. volume curve to obtain the equilibrium lattice parameter for bcc-Fe. For the carbides, first the ions were relaxed, then the shape and volume and finally both the ions and shape were relaxed simultaneously.

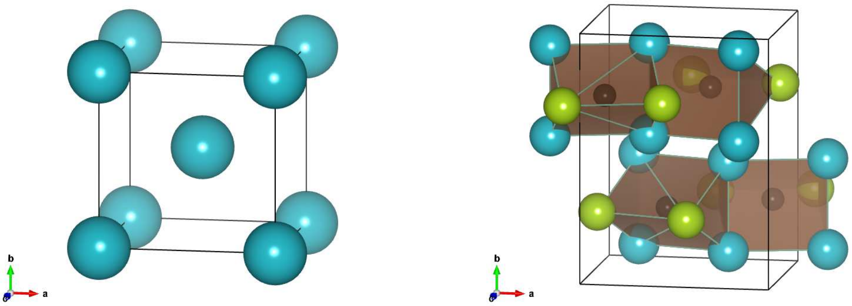

(a) bcc-Fe (b) Fe_3C

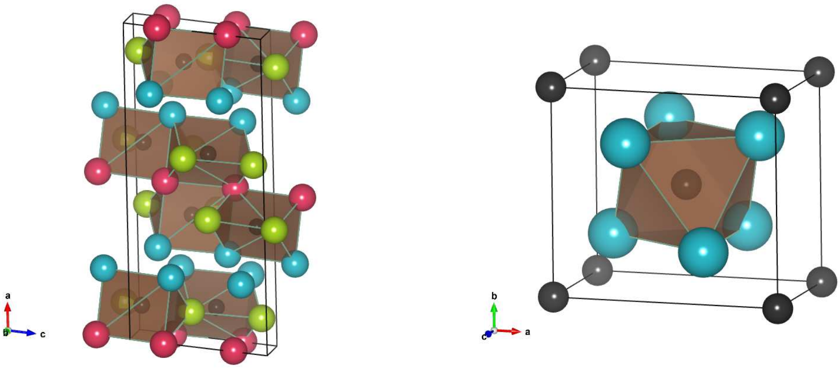

(c) Fe_5C_2 (d) η-Fe_2C

Figure 3.1: Crystal structures

Carbide (Sp. Gp. No., Pearson Sym.)	Lattice parameters [Å]	Atom (Site)	Fractional coordinates x, y, z	Magnetic moment / Fe atom [μ_B/Fe atom]	Magnetic moments [μ_B]
bcc-Fe (229, cI2)	a = 2.832 (2.866)		0.000, 0.000, 0.000 (0.000), (0.000), (0.000)		2.22 (2.22)
Fe_3C (62, oP16)	a = 5.032(5.090) b = 6.708(6.744) c = 4.477(4.525)	C(4c)	0.876, 0.250, 0.438 (0.877), (0.250), (0.444)	1.87	-0.10
		Fe1(4c)	0.035, 0.250, 0.837 (0.037), (0.250), (0.840)		1.97
		Fe2(8d)	0.176, 0.068, 0.332 (0.182), (0.067), (0.337)		1.89
Fe_5C_2 (15, mC28)	a = 11.579(11.563) b = 4.495(4.573) c = 4.975(5.058) β = 97.6(97.7)	C(8f)	0.113, 0.186, 0.579 (0.106), (0.189), (0.577)	1.69	-0.10
		Fe1(8f)	0.401, 0.084, 0.082 (0.404), (0.095), (0.079)		2.11
		Fe2(8f)	0.214, 0.082, 0.310 (0.213), (0.073), (0.314)		1.69
		Fe3(4e)	0.000, 0.067, 0.250 (0.000), (0.073), (0.250)		1.04
$\eta - Fe_2C$ (58, oP6)	a = 4.708 b = 4.281 c = 2.824	C(2a)	0.000, 0.500, 0.000 (0.000), (0.500), (0.000)	1.61	-0.10
		Fe(4g)	0.346, 0.751, 0.000 (0.333), (0.750), (0.000)		1.68

Table 3.1: Crystal structures of Fe_3C, Fe_5C_2 and η-Fe_2C. The column labeled "Site" indicates both the multiplicity and the Wyckoff symbol. The numbers in parenthesis are experimental results obtained from [64], [68] and [45] for Fe_3C, Fe_5C_2 and $\eta - Fe_2C$ respectively. Expt. results for bcc-Fe from [76].

the magnetic moment on each of the Fe atoms are give in Table 3.1. The magnetic moments of the Fe atoms in cementite agree well with the experimental results in Ref. [77].

3.3 Thermodynamic properties

3.3.1 Theory

The Helmholtz (F) and Gibbs (G) free energies of a system are given as

$$\begin{aligned} F &= E - TS \\ G &= H - TS = E + pV - TS = F + pV \end{aligned}$$

At constant temperature and pressure, the relevant thermodynamic quantity to consider when comparing state changes is the Gibbs free energy G. The change in Gibbs free energy can thus be written as

$$\begin{aligned} \Delta G &= \Delta H - T\Delta S \\ &= \Delta E + p\Delta V - T\Delta S \end{aligned} \tag{3.1}$$

At atmospheric pressures, condensed phases (liquids and solids) can be considered incompressible ($\Delta V = 0$). Hence, using $\Delta V = 0$ in 3.1, we would have

$$\Delta G = \Delta E - T\Delta S = \Delta F$$

where F is the Helmholtz free energy. Therefore, we can consider the change in Helmholtz free energy as the relevant quantity when investigating changes of states for solids.

Now, consider the formation of the solid AB_2 from its constituent elements A and B at a temperature T

$$A + 2B \rightarrow AB_2 \tag{3.2}$$

The Helmholts free energy of formation for the reaction can be written as [2]

$$\begin{aligned} \Delta F &= F[AB_2] - (F[A] + 2F[B]) \\ &= (E[AB_2] - (E[A] + 2E[B])) - T\left(S[AB_2] - (S[A] + 2S[B])\right) \\ &= \Delta E - T\Delta S \end{aligned}$$

where $F[A]$ is the free energy of the element A at the temperature T and so on. Thus, to obtain an accurate free energy of formation, one also needs to calculate the change in entropy of the reaction. But, the total energy obtained from a routine first-principles calculation is usually at T=0 K and thus one can only calculate ΔE for a reaction unless the change in entropy is taken into consideration by

---

[2] When one considers the Gibbs free energy of the reaction, another term $p\Delta V$ occurs. ΔV is the difference in the molar volumes of the products and the reactants and is easily obtained from either experiments or first-principles calculations.

some other means. But, nonetheless, it is not unusual to find in scientific literature that one calculates the formation energy ΔE at 0 K and compares this 0 K formation energy free energy changes obtained from experiments at finite temperatures. Fortunately, although not many mention it, this is partly justified by the Neumann-Kopp rule [78].

The Neumann-Kopp rule states that the heat capacity of a solid compound AB_2 formed from solid elements A and B can be written as the sum of the weighted heat capacities of the elements A and B [79],

$$C_p(AB_2)(T) \approx C_p(A)(T) + 2C_p(B)(T)$$

$$C_p(AB_2)(T) - C_p(A)(T) - 2C_p(B)(T) \approx 0 \tag{3.3}$$

Using Eq. 3.3 and the relations,

$$\Delta H(T) = \int_0^T C_p \mathrm{d}T \qquad - T\Delta S(T) = -T\int_0^T \frac{C_p}{T}\mathrm{d}T$$

we can show that

$$\Delta G(AB_2)(T) - \Delta G(A)(T) - 2\Delta G(B)(T) = 0$$

$$\Delta(\Delta G(T)) \approx 0$$

This implies that the change in free of the reaction ΔG as a function of temperature $\Delta(\Delta G(T))$ is approximately zero. Equivalently, for Helmholtz free energy we would have,

$$\Delta(\Delta F(T)) \approx 0$$

and thus,

$$\Delta(\Delta E(T)) \approx 0$$

3.3.1.1 Formation energy

Thus the formation energy for the reaction in Eq. 3.2 can be given as

$$\Delta E = E[\mathrm{AB_2}] - E[\mathrm{A}] - 2E[\mathrm{B}] \tag{3.4}$$

where $E[\mathrm{AB_2}]$ is the internal energy of the compound AB_2 and $E[\mathrm{A}]$ and $E[\mathrm{B}]$ are the internal energies of the elements from which AB_2 forms.

The free energy of a solid can also be written as a sum of the energy at 0 K and due to vibrational, magnetic and electronic excitations at higher temperatures, i.e.

$$F(T) = E(0) + F_{vib}(T) + F_{mag}(T) + F_{el}(T) \tag{3.5}$$

where $E(0)$ is the energy of the solid at 0 K, F_{vib}, F_{mag}, F_{el} are the temperature dependent vibrational, magnetic and electronic free energies. $E(0)$ is obtained from a routine DFT calculation, F_{vib} can be obtained by calculating the phonons in the solid, F_{mag} can be obtained by calculating the magnons, and F_{el} can approximated from the electronic density of states at the Fermi level.

3.3.1.2 Vibrational free energy

Vibrational free energy of a solid can be obtained from a number of approximations: the Debye model [80], the Einstein model [80], the small displacement method and from linear response theory. The vibrational free energy in the Debye model is given as [80]

$$F_{vib}(T) = 9k_B T \left(\frac{T}{T_D}\right)^3 \int_0^{T_D/T} \frac{x^3}{e^x - 1} \mathrm{d}x \tag{3.6}$$

where T_D is the Debye temperature given by

$$T_D = \frac{hc_s}{2k_B} \sqrt[3]{\frac{6}{\pi}\frac{N}{V}} \tag{3.7}$$

where c_s is the speed of sound in the solid, N is the number of atoms in the solid, and V is the volume of the solid. The Debye temperature can be interpreted as the temperature at which the highest-frequency mode (and hence all modes) are excited.

The Debye model treats the vibrations of the atomic lattice as phonons in a box, in contrast to the Einstein model, which treats the solid as many individual, non-interacting quantum harmonic oscillators. The Debye model correctly predicts the low temperature dependence of the heat capacity, which is proportional to T^3. Similar to the Einstein model, it also recovers the Dulong-Petit law at high temperatures. But due to simplifying assumptions, its accuracy suffers at intermediate temperatures [81].

Ignoring the anharmonic contributions, F_{vib} can also be approximated using the small displacement method. We use the method as implemented in the PHON program [82]. F_{vib} can be calculated as follows [82]. Consider a crystal at very low temperature and expand the potential energy function around the equilibrium positions of the nuclei. The first term of the expansion is simply the energy of the system calculated with the ions in their equilibrium positions, $E(0)$. If the crystal is near its minimum energy configuration the linear term of the expansion is zero, and the first term is a quadratic term in the atomic displacements:

$$U_{harm} = E_{perf} + \frac{1}{2} \sum_{ls\alpha,l't\beta} \phi_{ls\alpha,lt\beta} u_{ls\alpha} u_{l't\beta}, \tag{3.8}$$

where $\mathbf{u}_{ls}$ denotes the displacement of atom s in unit cell l, α and β are Cartesian components, and $\phi_{ls\alpha,l't\beta}$ is the force-constant matrix, given by the double derivative $\partial^2 U/\partial u_{ls\alpha}\partial_{l't\beta}$ evaluated with all atoms at their equilibrium positions. This force constant matrix gives the relation between the forces $\mathbf{F}_{ls}$ and the displacements $\mathbf{u}_{l't}$, as can be seen by differentiating Eq. 3.8 and ignoring the higher-order anharmonic terms:

$$F_{ls\alpha} = -\partial U/\partial u_{ls\alpha} = -\sum_{l't\beta} \phi_{ls\alpha,l't\beta} u_{l't\beta}. \tag{3.9}$$

Within this quasi-harmonic approximation (the prefix "quasi" is there to indicate that the force constant matrix may depend on volume), the potential energy function U_{harm} completely determines the physical properties of the system, and in particular the Helmholtz free energy, which at constant volume takes the form:

$$F(T) = E(0) + F_{harm}(T),$$

with the quasi-harmonic component of the free energy given by:

$$F_{vib} = k_B T \sum_n \ln\left(2\sinh(\hbar\omega_n/2k_B T)\right),$$

with ω_n the frequency of the nth vibrational mode of the crystal, k_B the Boltzmann constant, and T the temperature of the system. In a periodic crystal, the vibrational modes can be characterized by a wave-vector $\mathbf{q}$, and for each such wave-vector there are three vibrational modes for every atom in the primitive cell. If the frequency of the sth mode at wave-vector $\mathbf{q}$ is denoted by $\omega_{\mathbf{q}s}$, then the vibrational free energy is:

$$F_{vib} = k_B T \sum_{\mathbf{q}s} \ln\left(2\sinh(\hbar\omega_{\mathbf{q}s}/2k_B T)\right).$$

The vibrational frequencies $\omega_{\mathbf{q}s}$ are the square root of eigenvalues of the dynamical matrix, $D_{s\alpha,t\beta}(\mathbf{q})$, defined as:

$$D_{s\alpha,t\beta}(\mathbf{q}) = \frac{1}{\sqrt{M_s M_t}} \sum_l \phi_{ls\alpha,0t\beta} \exp[i\mathbf{q}\cdot(\mathbf{R}_0 + \boldsymbol{\o}_t - \mathbf{R}_l - \boldsymbol{\o}_s],$$

where $\mathbf{R}_l + \boldsymbol{\o}_s$ represents the equilibrium position of atom s with mass M_s in primitive cell l, and the sum runs over the infinite number of primitive cells in the crystal. If the complete force-constant matrix is known, then $D_{s\alpha,t\beta}$ and hence the frequencies $\omega_{\mathbf{q}s}$ can be obtained at any $\mathbf{q}$.

The force constant matrix expresses the proportionality between displacements and forces, when the displacements are small enough for this relationship to be linear (Eq. 3.9). All that has to be done, in principle is to displace a single atom t in a cell l' in Cartesian direction β, all other atoms being held fixed at their equilibrium positions; the forces $F_{ls\alpha}$ on all the atoms give directly the elements of the force constant matrix $\phi_{ls\alpha,l't\beta}$ for the give $(l't\beta)$. If this procedure is repeated for all other $(l't\beta)$, all the elements of the force constant matrix can be obtained. Translational invariance implies that the number of separate calculations required to do this is at most three times the number of atoms in the primitive cell, but for most materials symmetry relations can be used to reduce this number substantially.

3.3.1.3 Magnetic free energy

$F_{mag}(T)$ can be obtained in different ways. One way to calculate $F_{mag}(T)$ is by knowing how the magnetic contribution to the specific heat capacity C_v^{mag} varies with temperature. The magnetic free energy can be written as

$$\begin{aligned} F_{mag}(T) &= E_{mag}(T) - TS_{mag}(T) \\ &= \int C_v^{mag}(T)\mathrm{d}T - T\int \frac{C_v^{mag}}{T}\mathrm{d}T \end{aligned} \tag{3.10}$$

where E, S, C_v are the internal energy, entropy and specific heat at constant volume respectively. In the case of iron the contribution above and below the Curie temperature T_C, can be obtained from [83]

$$\begin{aligned} C_m &= k_f(T/T_C)\exp[-4(1-T/T_C)] \qquad (T < T_C) \\ &= k_p(T/T_C)\exp[8p(1-T/T_C)] \qquad (T > T_C) \end{aligned}$$

The parameters k_f and k_p are determined by the Curie temperature T_C, the magnetic entropy S_{mag}, and the fraction (f_s) of magnetic entropy above the Curie temperature, with

$$\begin{aligned} k_f &= 4(1-f_s)S_{mag}/(1-\exp(-4)) \\ k_p &= 8pf_sS_{mag} \end{aligned}$$

where

$$S_{mag} = R\ln(1+S_a)$$

and $f_s = 0.105$, and $p = 2$ are fitting parameters and S_a is the magnetic moment per Fe atom. They are also used as parameters for the hcp structures cementite and Hägg carbides, due to the strong similarity between the local structure of the Fe sublattices to that of the fcc lattice.

3.3.1.4 Electronic free energy

The free energy contribution from electronic excitations F_{el} is also obtained first by an approximation of the electronic contribution C_v^{el} to the specific heat capacity and then using an equation similar to Eq. 3.10. In the simplest approximation, C_v^{el} is given as

$$C_v^{el} = \gamma T = \frac{2\pi^2}{3}N(E_F)k_B^2T$$

where $N(E_F)$ is the electronic density of states the Fermi level E_F. But, usually C_v^{el} has appreciable contributions only at very high temperatures and is usually neglected. For a more detailed discussion see Chap. 10 of Ref. [84].

3.3.2 Results and discussion

3.3.2.1 Formation energies

The formation energies[3] of the carbides calculated from Eq. 3.4 are listed in Table 3.2. The formation energies of all the three carbides are positive, indicating that

---

[3] 100 meV/atom $\approxeq$ 9.65 kJ/mole

Property	bcc-Fe	Fe_3C	Fe_5C_2	η-Fe_2C
Formation energy [meV/atom] at 0 K	0	16 (49±11)	13	5
Debye temperature [K] Expt.	429 453	538 604±44 [49] 501±27 [60] 475/468 [93]	541	647

Table 3.2: Thermodynamic properties. Experimental values are listed in parenthesis.

they are all metastable with respect to the elements from which they form. Our results are in good agreement with previous first-principle results [4,56,61,85–90]. The formation energies increase in the order: $Fe_3C > Fe_5C_2 > \eta$-Fe_2C and is consistent with earlier calculations [4, 85]. It is interesting to note that these carbides also occur in the same sequence during precipitation in steels [86].

3.3.2.2 Vibrational free energy

The phonon dispersions[4] of the three carbides along with bcc-Fe is shown in Fig. 3.2. The phonon dispersion of bcc-Fe agrees very well with previously reported calculations [57] and experiments [91, 92]. The phonon dispersion of cementite is similar to the one obtained by Jiang et al. [57]. The phonon dispersions of Fe_5C_2 and η-Fe_2C have not been reported yet. All the carbides have phonon frequencies between 0 and 10 THz. Cementite and Hägg carbides have three blocks of phonon frequencies between 10 and 20 THz. η-Fe_2C only has two blocks with the second one between 15 and 22 THz. Only η-Fe_2C has phonon frequencies above 20 THz.

The vibrational free energy calculated using the small displacement method (Sec. 3.3.1.2) for the carbides along with the vibrational free energy of bcc-Fe is shown in Fig. 3.3. Debye temperatures were obtained by fitting the vibrational free energy obtained using the Debye model to the one obtained from the small displacement method (Fig. 3.3).

As expected the 'harder' carbides have a higher Debye temperature compared to bcc-Fe. The Debye temperature shows a strong dependence on the structure of the carbide. Both Fe_3C and Fe_5C_2 which have similar crystal structures have very similar Debye temperatures while η-Fe_2C which has a different crystal structure also has a much higher Debye temperature.

3.3.2.3 Predominance of cementite in steels

Although a number of iron carbide phases are known experimentally only one metastable carbide phase occurs predominantly in steels and the reasons for this

---

[4] Primitive k-points as listed at the Bilbao Crystallography server have been used.

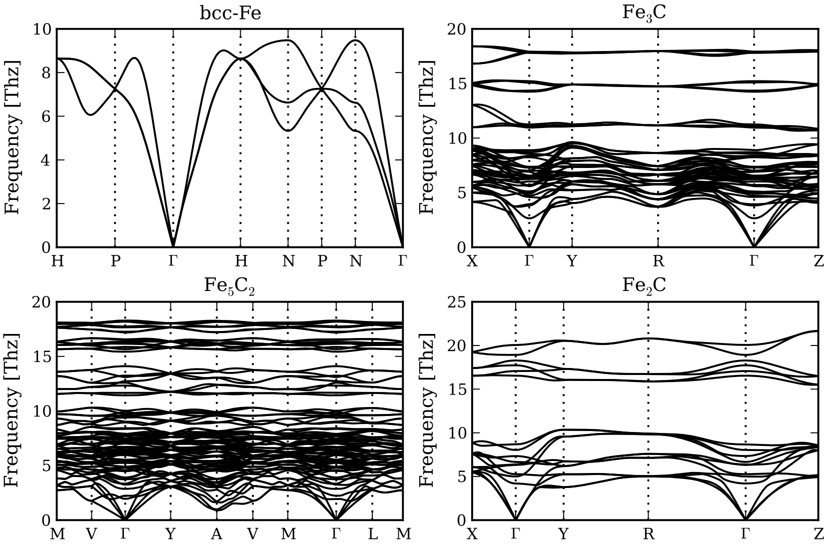

Figure 3.2: Phonon dispersion.

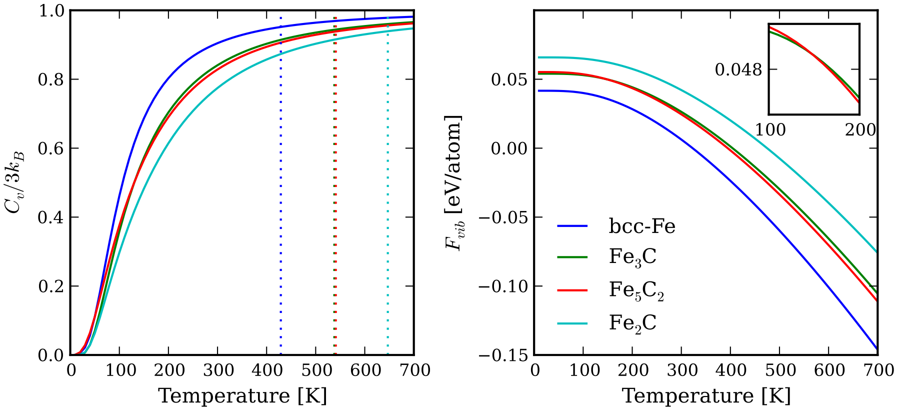

Figure 3.3: Debye temperatures and vibrational free energy for bcc-Fe, Fe_3C, Fe_5C_2, and η-Fe_2C.

were unclear. It is conventionally understood that the predominance of cementite Fe_3C is due to lattice matching of the carbide with the iron matrix. The vibrational free energy $F_{vib}(T)$ obtained in this study (Sec. 3.3.2.2) along with $E(0)$ and $F_{mag}(T)$ (Eq. 3.5) obtained by Fang et al. was used to show that contributions from the vibrational free energy and the magnetic free energy rather than from conventional lattice mismatch with the matrix, are the origin of the predominance of cementite during steel fabrication processes [86].

3.4 Mechanical properties

3.4.1 Theory

When small stresses are applied to a material, the deformation of the material (strain) is linearly proportional to the applied stress. When the stress is removed the 'elasticity' of the material returns the material to its original shape. This is elasticity theory at its most basic. From an atomistic point of view, this can be understood in the following way.

Imagine a crystalline solid in which all the atoms are connected by springs (bonds) which are harmonic for small displacements (the restoring force is proportional to the displacement). Given a certain direction in which the springs are connected, the spring constants are all equal. But, springs in different directions have different spring constants. Now, if we apply a small stress in a certain direction, the material will deform harmonically and the deformation would be directly proportional to the magnitude of the spring constant in that direction. If the magnitude of the applied stress is too large and we go beyond the harmonic regime of the spring, we might actually destroy the spring (break a bond) and there will be no restoring force to restore the crystal to its original shape. The regime below which the crystal completely regains its original shape after the removal of the stress is the regime of elasticity.

Stress describes the surface forces acting on a volume element in a continuum and can be represented by a symmetric second order tensor σ_{ij} thus with only six independent components. Strain describes the state of deformation of a solid body and can similarly be represented by a symmetric second order tensor ϵ_{ij} with six independent components.

The relation between the applied stress and the resultant strain in the material are related to each other via the fourth rank compliance tensor:

$$\epsilon_{ij} = S_{ijkl}\sigma_{kl} \tag{3.11}$$

which in matrix notation would be $\boldsymbol{\epsilon} = \boldsymbol{S\sigma}$.

Or equivalently, the applied strain is related to the resultant stress via the stiffness tensor:

$$\sigma_{ij} = C_{ijkl}\epsilon_{kl} \tag{3.12}$$

Tensor notation	11	22	33	23,32	13,31	12,21
Voigt notation	1	2	3	4	5	6

Table 3.3: Relation between tensor notation and Voigt notation.

and as before in matrix notation $\boldsymbol{\sigma} = \boldsymbol{C\epsilon}$. As can be seen, the stiffness tensor is just an inverse of the compliance tensor, $\mathbf{C} = \mathbf{S}^{-1}$.

Depending on the translational and rotational symmetries present in a crystalline system, the number of independent components of the fourth rank reduces to 21, for the least symmetric crystal system, from 81 in the full tensor. Depending on to which crystal system a crystal belongs to, the number of independent components are: triclinic (21), monoclinic (15), orthorhombic (9), trigonal (7), tetragonal (5), hexagonal (5) and cubic (3).

Since six independent components are enough to describe stress and strain, Voigt [94] used this fact to replace the cumbersome second and fourth order tensors in a three-dimension vector space by vectors and matrices in a six-dimension vector space. The different components in the tensor notation and Voigt notation transform as shown in Table 3.3.

In matrix notation Eq. 3.12 can now be written as

$$\begin{pmatrix} \sigma_{xx} \\ \sigma_{yy} \\ \sigma_{zz} \\ \sigma_{yz} \\ \sigma_{xz} \\ \sigma_{xy} \end{pmatrix} = \begin{pmatrix} C_{11} & C_{12} & C_{13} & C_{14} & C_{15} & C_{16} \\ C_{12} & C_{22} & C_{23} & C_{24} & C_{25} & C_{26} \\ C_{13} & C_{23} & C_{33} & C_{34} & C_{35} & C_{36} \\ C_{14} & C_{24} & C_{34} & C_{44} & C_{45} & C_{46} \\ C_{15} & C_{25} & C_{35} & C_{45} & C_{55} & C_{56} \\ C_{16} & C_{26} & C_{36} & C_{46} & C_{56} & C_{66} \end{pmatrix} \begin{pmatrix} \epsilon_{xx} \\ \epsilon_{yy} \\ \epsilon_{zz} \\ 2\epsilon_{yz} \\ 2\epsilon_{xz} \\ 2\epsilon_{xy} \end{pmatrix}$$

where the Voigt notation has been used only for the stiffness tensor.

Usually, the elastic properties of a material, consisting of anisotropic grains are replaced by those of an "equivalent" material; a material with grains at random orientations behaves isotropically. These processes of averaging are especially important to treat materials consisting of crystalline grains of random orientation. There are three main schemes: Voigt [94], Reuss [95] and Hill [96].

The Voigt averaging scheme is based on the stiffness matrix (assuming a given uniform strain) and the bulk modulus K and the shear modulus G are given by

$$K_V = \frac{A + 2B}{3}, \qquad G_V = \frac{A - B + 3C}{5},$$

where

$$A = \frac{C_{11} + C_{22} + C_{33}}{3}, \qquad B = \frac{C_{23} + C_{13} + C_{12}}{3}, \qquad C = \frac{C_{44} + C_{55} + C_{66}}{3}.$$

On the other hand, the Reuss averaging scheme is based on the compliance matrix (assuming a given uniform stress) and:

$$K_R = \frac{1}{3a + 6b}, \qquad G_R = \frac{5}{4a - 4b + 3c},$$

where

$$a = \frac{S_{11} + S_{22} + S_{33}}{3}, \qquad b = \frac{S_{23} + S_{13} + S_{12}}{3}, \qquad c = \frac{S_{44} + S_{55} + S_{66}}{3}.$$

In both cases, the Young's modulus E and the Poisson's ratio ν are given by

$$E = \left(\frac{1}{3G} + \frac{1}{9K} \right)^{-1}, \qquad \nu = \frac{1}{2} \left(1 - \frac{3G}{3K + G} \right).$$

The Hill average is the arithmetic average of the Voigt and Reuss values, $K_H = 0.5(K_V + K_R)$, $G_H = 0.5(G_V + G_R)$, and so on.

The elastic tensor is determined by performing six finite distortions of the lattice and deriving the elastic constants from the strain-stress relationship [97] as implemented in VASP. The averages were calculated using the ElAM code [98]. The PBE exchange-correlational functional with a plane wave cutoff of 500 eV was used in calculating the mechanical properties listed below.

3.4.2 Results and discussion

The stiffness matrices of bcc-Fe, Fe_3C, Fe_5C_2, and η-Fe_2C are given in Table 3.5. The bulk modulus, Young's modulus, shear modulus, and the Poisson's ratio along with various averages are given in Table 3.4. When comparing to experiments, we consider the Hill average unless otherwise mentioned.

In line with the underestimation of the lattice parameter for bcc-Fe, we obtain a 10% larger bulk modulus compared to experiments (188 vs. 170 GPa). But usually, an error of about 10% in bulk moduli obtained from first-principles calculations is expected compared to experiments. The Young's modulus, shear modulus and the Poisson's ratio agree well with experiments (Table 3.4) though. While C11 is overestimated by 20% compared to experiments (276 vs. 226 GPa), C44 is underestimated by about 20% (94 vs. 116 GPa) (experimental information form [76]). A bulk modulus of 179 GPa is obtained when the energy-volume method is used and a Birch-Murnaghan equation of state is used.[5]

Direct experimental determination of single-crystal elastic constants of cementite are still not feasible due to difficulties in growing large enough single-crystals [55]. Elastic constants have been determined indirectly through various ways (see Ref. [99] for a compilation). The spread in the experimental values is large. For example, the bulk moduli vary from 105 GPa to 244 GPa, the Young's moduli vary from 140 to 298 GPa, the shear moduli vary from 46 to 95 GPa. But, a bulk modulus of around 175 GPa is obtained consistently by most measurements on bulk, polycrystalline samples using diamond anvil cell measurements. Our results fall in between the ranges observed experimentally (Table 3.4). The bulk modulus, Poisson's ratio and the stiffness matrix, (except for C_{44}) that we obtain are within 5%

---

[5] The PW91 exchange correlation functional was used in this calculation with a 400 eV plane wave cutoff energy.

percent from the values obtained in Ref. [55]. The strong departure of the experimental values of the elastic-stiffness tensor from experiments was suggested to be due to the existence of Fe_3C in more than one crystal structure [60].

No experimental or theoretical determination of elastic moduli and stiffness constants has been done for the Hägg or η-Fe_2C carbides. The values we compute are listed in Table 3.4 and 3.5. Although there are a couple of negative components in the stiffness tensor for Fe_5C_2, the lowest eigen values of the stiffness tensor for all the carbides are positive and hence are mechanically stable [100]. Fe_3C, Fe_5C_2 and η-Fe_2C are all carbides with increasing amounts of C. In general, metal carbides show higher elastic stiffness than the metal itself and well known examples include TiB_2, TiC, VC, ZrC and TaC [101]. Thus, for the present carbides under consideration we can expect a larger elastic moduli and smaller Poisson's ratios compared to bcc-Fe. In line with the argument, the bulk modulus of all the carbides are higher than that of bcc-Fe. Although, the Young's modulus and shear modulus of cementite is lower than that of bcc-Fe, they increase with the fraction of C going from cementite to η-Fe_2C.

While bcc-Fe and η-Fe_2C behave similarly similarly both under uniform stress and strain, the behavior of Fe_3C and Fe_5C_2 are very different under uniform stress and strain as can be seen from the differences in Young's and shear moduli. Both Fe_3C and Fe_5C_2 have one anomalously small shear constants; for Fe_3C, C_{44} is about 15 GPa and for Fe_5C_2 C_{66} is 35 GPa.

3.5 Electronic properties

The total spin resolved electronic density of states for bcc-Fe and the carbides display no band gap indicating that they are metallic. The Fermi energy, similar to that of bcc-Fe also falls in a minimum of the density of states of the minority spin band. The majority spin band is nearly filled while the minority spin band is nearly half filled clearly showing that they are magnetic (Fig. 3.5). The averaged angular momentum projected density of states on Fe in bcc-Fe is shown in Fig. 3.4. The total and partial density of state of all the carbides display similar characteristics. The projected density of states for C and the different metal sites are shown in Fig. 3.6, 3.7, and 3.8. From Fig. 3.4 it can clearly be seen that 3d states contribute almost entirely to the total density of states of Fe. Majority of the 3d states occur between -5 eV to 4 eV with a few around 9 eV. In the carbides, the C-2s states occur between -14 eV and -12 eV and the C-2p states occur from -8 eV to -5 eV and again above the Fermi level. In contrast to bcc-Fe, the Fe-3d states are present already from -8 eV all the way to 10 eV approximately with a distinct block between -8 eV and -5 eV, where C-2p states also occur. This clearly shows the hybridization between the C-2p and the Fe-3d states indicating covalent bonding. While the bonding states appear between -8 eV to -5 eV, the anti-bonding states are spread above the Fermi level.

	Bulk modulus [GPa]	Young's modulus [GPa]	Shear modulus [GPa]	Poisson's ratio
		bcc-Fe		
Reuss	187	211	81	0.31
Voigt	188	217	83	0.31
Hill	188	214	82	0.31
BM	179	-	-	-
[102]	170	211	82	0.29
		Fe_3C		
Reuss	220	109	93	0.42
Voigt	222	246	38	0.32
Hill	221	177	66	0.37
BM	215	-	-	-
Expt. [55]	175	196	74	0.36
and Ref. therein	174	177		
	174	200		
		200		
		Fe_5C_2		
Reuss	226	203	75	0.35
Voigt	226	262	100	0.31
Hill	226	233	88	0.33
BM	233	-	-	-
		η-Fe_2C		
Reuss	223	255	98	0.31
Voigt	226	271	104	0.30
Hill	225	263	101	0.30
BM	223	-	-	-

Table 3.4: Mechanical properties. Reuss, Voigt and Hill averages. PBE at 500 eV cutoff.

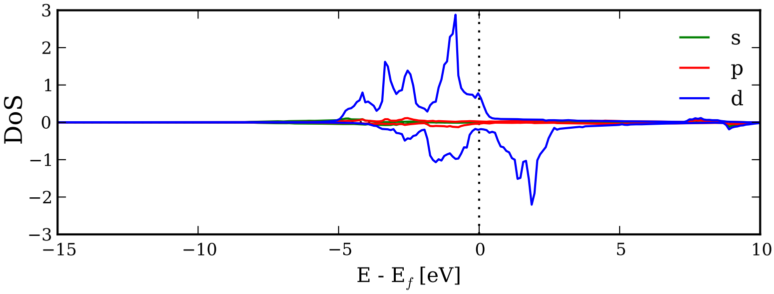

Figure 3.4: Partial electronic density of states, bcc-Fe.

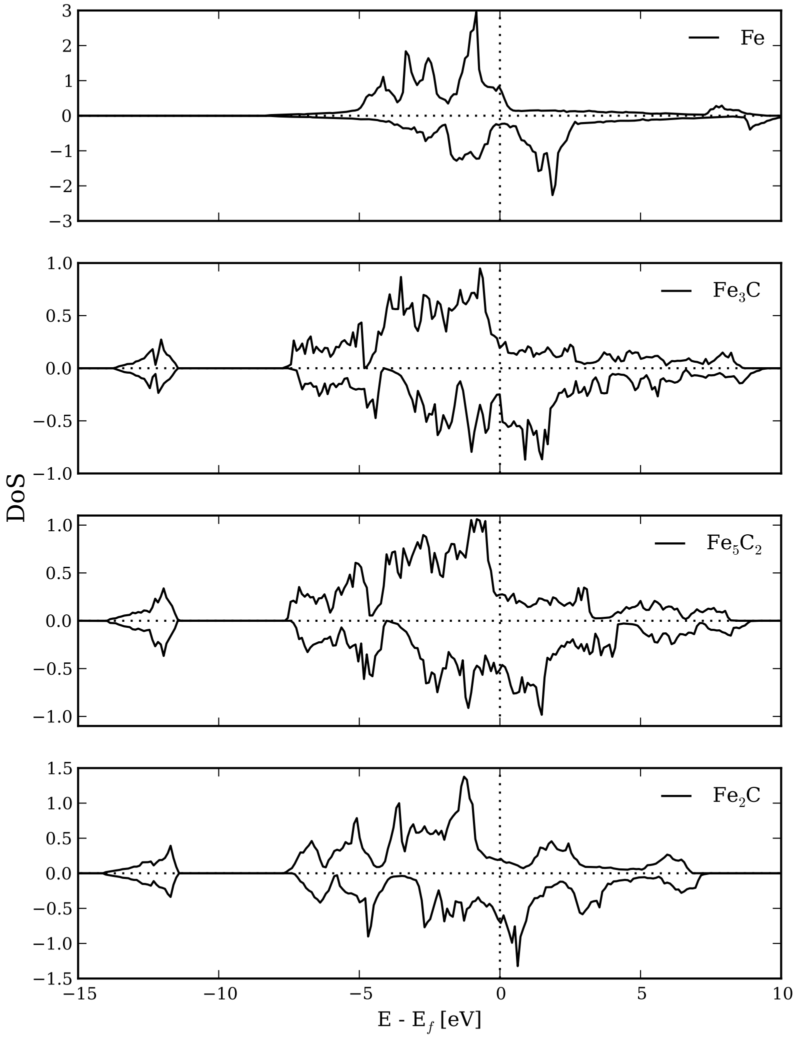

Figure 3.5: Electronic density of states of bcc-Fe, Fe_3C, Fe_5C_2 and η-Fe_2C.

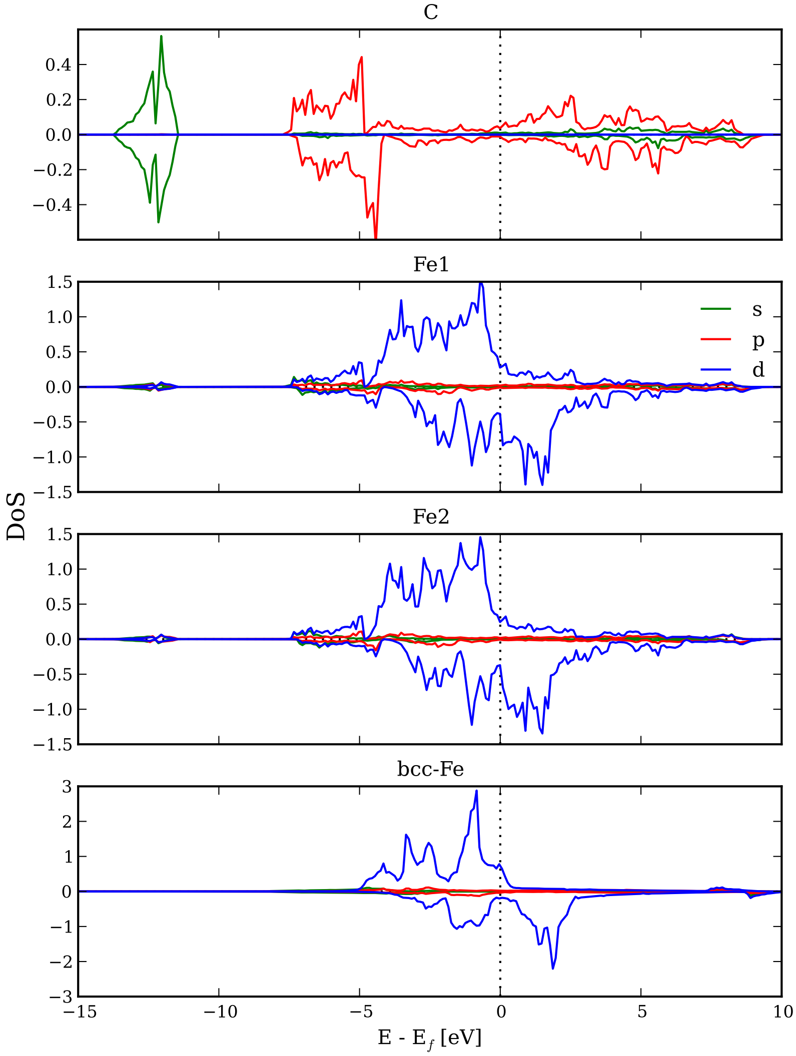

Figure 3.6: Electronic density of states, Fe_3C

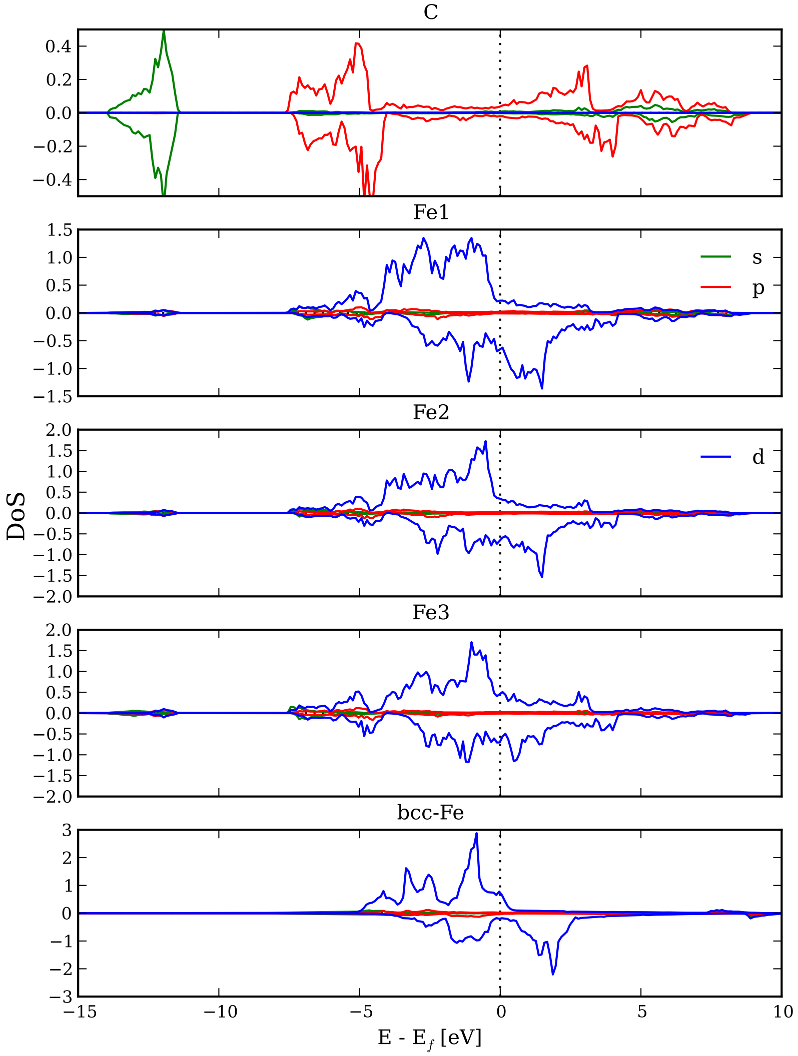

Figure 3.7: Electronic density of states, Fe_5C_2.

$\begin{pmatrix} 276 & 144 & 144 & 0 & 0 & 0 \\ 144 & 276 & 144 & 0 & 0 & 0 \\ 144 & 144 & 276 & 0 & 0 & 0 \\ 0 & 0 & 0 & 94 & 0 & 0 \\ 0 & 0 & 0 & 0 & 94 & 0 \\ 0 & 0 & 0 & 0 & 0 & 94 \end{pmatrix}$	$\begin{pmatrix} 388 & 155 & 162 & 0 & 0 & 0 \\ 155 & 342 & 159 & 0 & 0 & 0 \\ 162 & 159 & 317 & 0 & 0 & 0 \\ 0 & 0 & 0 & 11 & 0 & 0 \\ 0 & 0 & 0 & 0 & 133 & 0 \\ 0 & 0 & 0 & 0 & 0 & 133 \end{pmatrix}$
$\begin{pmatrix} 347 & 183 & 147 & 0 & -9 & 0 \\ 183 & 333 & 151 & 0 & 25 & 0 \\ 147 & 151 & 389 & 0 & 2 & 0 \\ 0 & 0 & 0 & 139 & 0 & -11 \\ -9 & 25 & 2 & 0 & 132 & 0 \\ 0 & 0 & 0 & -11 & 0 & 35 \end{pmatrix}$	$\begin{pmatrix} 293 & 190 & 142 & 0 & 0 & 0 \\ 190 & 345 & 167 & 0 & 0 & 0 \\ 142 & 167 & 404 & 0 & 0 & 0 \\ 0 & 0 & 0 & 107 & 0 & 0 \\ 0 & 0 & 0 & 0 & 97 & 0 \\ 0 & 0 & 0 & 0 & 0 & 136 \end{pmatrix}$

Table 3.5: Stiffness matrices (GPa) as obtained from first-principles calculations. From top-left to bottom-right: bcc-Fe, Fe_3C, Fe_5C_2, and η-Fe_2C .

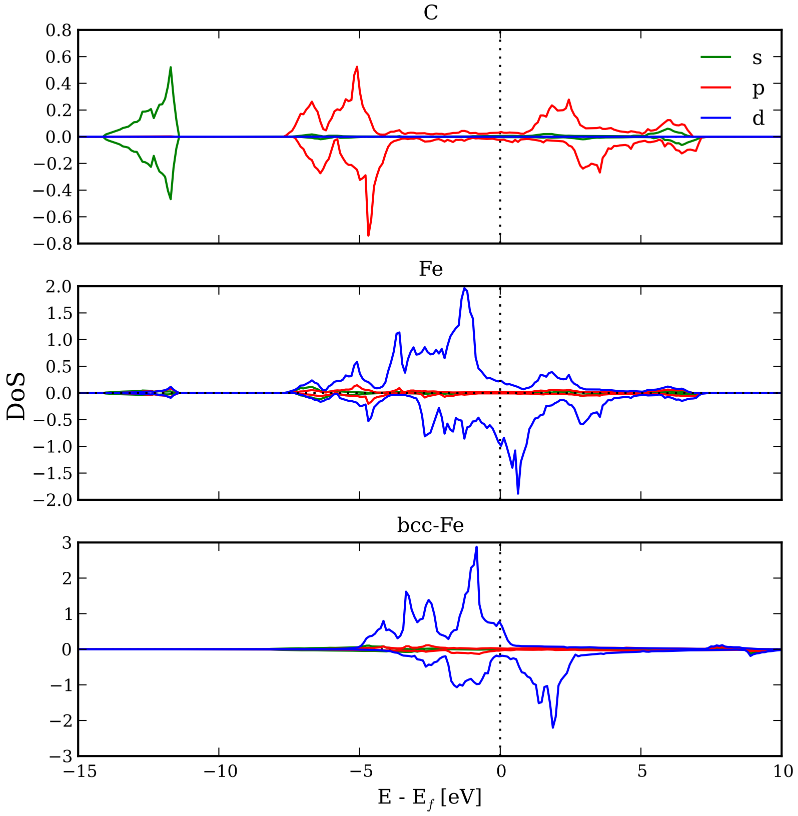

Figure 3.8: Electronic density of states, η-Fe_2C.

Chapter 4

bcc-Fe with impurity atoms

4.1 Introduction

In this chapter, we calculate the solution energy of various alloying elements in bcc-Fe. These solution energies are used in the calculation of the partitioning energies of the alloying elements in Chap. 6 and 7. They can also be used in the calculation of solubility products of precipitate phases forming in bcc-Fe [103]. In addition, changes in magnetism and volume of impurity substituted bcc-Fe are studied. Results similar to the ones in this Chapter have been published in Ref. [104].

4.2 Methodology

bcc-Fe is modeled by a 3×3×3 supercell of bcc-Fe unit cells (Fe_{54}). Metal impurities in bcc-Fe substitutional solid solution are modeled by substituting one of the Fe atoms in the supercell with the impurity atom, represented as $Fe_{53}M$. A 4×4×4 supercell of bcc-Fe unit cells was also used to check the effect of supercell size on the solution enthalpy (Sec. 4.3.2).

We used the spin polarized generalized gradient approximation (GGA) to density functional theory (DFT) [18, 19] and a plane wave basis with an kinetic energy cut-off of 400 eV. The Kohn-Sham equations were solved using the Vienna ab initio simulation package (VASP, version 4.6.34) [105–109]. The valence and core electron interactions were described using the projector augmented wave method (PAW) [38]. All the projection operators were evaluated in real space as determined automatically by VASP. First order Methfessel-Paxton method was used with a smearing width of 0.1 eV. The PW91 exchange correlation functional [110, 111] with the Vosko-Wilk-Nusair interpolation [112] for the correlation part was used. The relaxations were assumed to have converged when the energy in two consecutive ionic relaxation steps differed by less than 10^{-5} eV. For accurate bulk energies, a final calculation was done without any relaxation using the linear tetrahedron method with Blöchl corrections for smearing. k-space sampling was done using the Monkhorst-Pack method [35] using 6×6×6 and 4×4×4 Gamma centered grids for the 54 and 128 atom supercells of bcc-Fe respectively. Both the k-point density and energy cutoff were checked for sufficient convergence of the total energies. Charges on the impurity ions were calculated using a Bader analysis of the charges using the VTST tool set [113–116].

We use the terms locally and fully relaxed structures in our discussion of the results and it merits a brief on note on their usage. In a 'fully relaxed' impurity substituted supercell, the volume, shape and atoms around the impurity atom are allowed to relax to equilibrium. In a 'locally relaxed' supercell, only the atoms in the supercell are allowed to relax at the fixed volume of the original bcc-Fe supercell.

4.3 Results and Discussion

4.3.1 Pure bcc-Fe

The results for pure bcc-Fe are very similar to the results discussed in Chap. 3. The lattice parameter that we obtain, 2.836 Å, agrees well with the lattice parameter obtained from experiments, 2.866 Å. Similarly, the magnetic moment per Fe atom, 2.21 μ_B also agrees quite well with the experimental value of 2.12 μ_B.

4.3.2 Solution energies and size dependence

The total enthalpies with the impurity elements in bcc-Fe are given in Table 4.1. As mentioned before, we use these total energies in the calculation of the partitioning energies in Chap. 6 and 7. Another use of these total enthalpies is to compute the mixing enthalpy for the solution of the impurity atoms in bcc-Fe.

The solution energies of the 54 and 128 atom supercells is given in Table 4.2. The solution energy is calculated as,

$$H^{n}_{sol} = H_{\mathrm{Fe_{n-1}M}} - H_{\mathrm{Fe_{n-1}}}$$

where n is the number of atoms in the supercell and M is the metal atom. As can be seen the difference $H^{54}_{sol} - H^{128}_{sol}$ is not very significant; the maximum being about 60 meV/atom for Mn and about 20 meV/atom for Al, P, S, Nb, Mo and W. It is seen that the total energy for Mn is very sensitive to the parameters of the calculation. The large discrepancy for Mn could be a consequence of this sensitivity. For Nb, Mo and W the difference might be arising due to relaxation effects due to the bigger size of Nb, Mo and W compared to Fe. Thus, no significant size dependence is observed for the solution energies in bcc-Fe as a function of the size of the supercell.

Element	$H_{Fe_{53}M}$ [eV] (spin)	$V_{Fe_{53}M}$ [Å^3] (spin)	V_{Fe53M} [Å^3] (non spin)	$\mu_{Fe_{53}M}$ [μ_B] (full)	$\mu_{Fe_{53}M}(V_{Fe_{54}})$ [μ_B] (local)
Al	-439.544	612.40	573.91	115.36	115.30
Si	-441.634	610.27	570.26	115.77	116.01
P	-441.453	609.76	569.65	116.42	116.63
S	-438.981	611.88	569.43	117.38	117.41
Ti	-443.689	615.87	575.72	116.06	115.55
V	-444.748	614.41	573.51	116.52	116.33
Cr	-444.707	614.37	567.88	117.07	116.79
Mn	-443.817	613.98	567.50	117.32	117.04
Fe	-443.295	611.96	563.90	119.70	119.70
Co	-442.226	613.51	570.88	120.53	120.38
Ni	-440.451	614.84	570.88	121.02	120.65
Cu	-438.078	614.32	571.35	118.45	118.22
Nb	-445.287	619.27	577.64	117.18	116.23
Mo	-445.870	618.27	575.07	117.41	116.82
W	-448.091	617.93	575.26	117.37	116.84

Table 4.1: Total enthalpy of the spin polarized super cells, volumes of spin polarized and non spin polarized supercells, magnetization of the fully and locally relaxed $Fe_{53}M$ supercells.

Element	$H_{Fe_{53}M}$	$H_{Fe_{127}M}$	H_{sol}^{54}	H_{sol}^{128}	$H_{sol}^{54} - H_{sol}^{128}$
Al	-439.544	-1047.077	-4.459	-4.477	0.018
Si	-441.634	-1049.143	-6.548	-6.542	-0.006
P	-441.453	-1048.933	-6.367	-6.332	-0.035
S	-438.981	-1046.461	-3.895	-3.861	-0.035
Ti	-443.689	-1051.206	-8.604	-8.605	0.002
V	-444.748	-1052.262	-9.662	-9.661	-0.001
Cr	-444.707	-1052.220	-9.621	-9.619	-0.002
Mn	-443.817	-1051.276	-8.731	-8.675	-0.056
Fe	-443.295	-1050.810	-8.209	-8.209	0.000
Co	-442.226	-1049.743	-7.140	-7.142	0.002
Ni	-440.451	-1047.973	-5.365	-5.372	0.007
Cu	-438.078	-1045.598	-2.993	-2.997	0.005
Nb	-445.287	-1052.776	-10.201	-10.175	-0.026
Mo	-445.870	-1053.371	-10.784	-10.770	-0.014
W	-448.091	-1055.592	-13.005	-12.991	-0.014

Table 4.2: Solution energies for the 54 atom and 128 atom supercells. All values in eV/atom

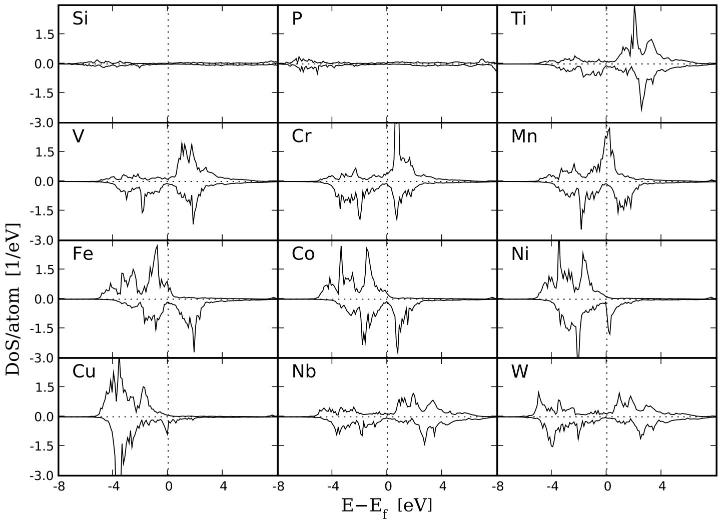

Figure 4.1: Site projected density of states of the impurity atoms in bcc-Fe. p-states are shown for Si and P. d-states are shown for the rest. Plots for Al, S and Mo are not shown as they are similar to those of Si, P and W respectively.

4.3.3 Partial density of states

The partial density of states of the impurity atoms in bcc-Fe (4.1) qualitatively agree quite well with the ones calculated by Drittler et al. [117]. The Fermi level falls in the minimum of the spin down density of states and forms a pseudo gap [118]. The higher electronegativity of Fe atoms compared to Al leads to a complete loss of valence electrons (Fig. 4.2) and hence almost no p-states are seen. The p-states for P and S are seen in the -4 to -8 eV range. For all the 3d transition metal atoms till Ni, the Fermi level is pinned in the minimum of the spin down partial density of states. The movement of the spin up band going from Cr to Ti is understood in terms of filling up of a an empty virtual bound state that appears close to the Fermi level [119]. The spin up band is gradually filled and the virtual bound state moves closer to the Fermi level. At Co, the spin up states are more or less filled and the spin down states start to fill up at Ni. For Cu, both the spin up and the spin down states are completely filled [104, 119]. The minimum in the density of states is not very well defined in the case of Nb, Mo and W. The spin polarization of the d-band is also relatively smaller compared to the 3d transition elements.

4.3.4 Bader charge analysis

Partial charges on the impurity elements in general follow the trend in the Pauling electronegativity of the respective elements. Exceptions are Al, Mo and W. Al loses

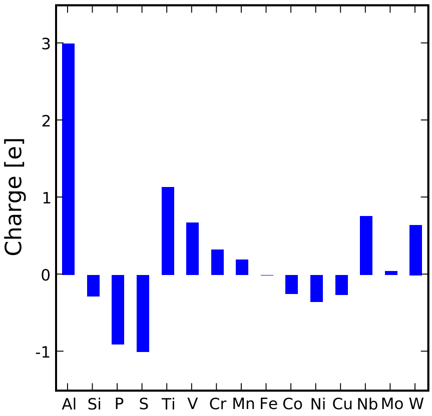

Figure 4.2: Partial charges on the impurity atoms computed using a Bader analysis of the charge distribution.

all of it's valence electrons and has a charge of about +3 e^-. Mo and W although more electronegative than Fe still lose charge instead of gaining it.

4.3.5 Impurity magnetic moments

The case of transition metal impurities in bcc-Fe has been studied in detail in [104, 117, 120]. Al, Si, P and S show negligible spin polarization and have negligible local moments. The early and late transition metals, Sc, Ti, V, Cu and Zn, do not satisfy the local Stoner criterion and therefore the magnetic moments induced on these atoms is not intrinsic but is induced by the host atoms [104]. Cr, Mn, Co and Ni satisfy the Stoner criterion and therefore have an intrinsic magnetic moment. In the case of Cu and Zn, the d-band is completely full and thus no magnetic interaction with the host is expected. The moments on the impurity atoms are shown in Figure 4.3. The local moments of the early 3d transition elements have a slightly higher magnitude than the moments seen either in Dritter, et al.'s results or in experiments.

The qualitative agreement with the previous results [117] is good except for the case of Mn. The moment on Mn seems to be very sensitive to the parameters of the calculation. A range of ferro and anti-ferromagnetic moments have been reported for Mn in the past. Experiments seem to suggest a slightly positive moment on Mn. But it should be noted that the magnetic moments are also sensitive to temperature and concentration variations. It is seen (also in Ref. [104]) that the magnetic moment of Mn is extremely sensitive to the volume of the supercell; switching from anti-ferromagnetic at slightly lower volumes to ferromagnetic at slightly larger volumes. This, along with the sensitivity of the moment to temperature and concentration and the fact that first-principles calculations are carried out at 0 K could be a possible reason for the discrepancies between the theoretical

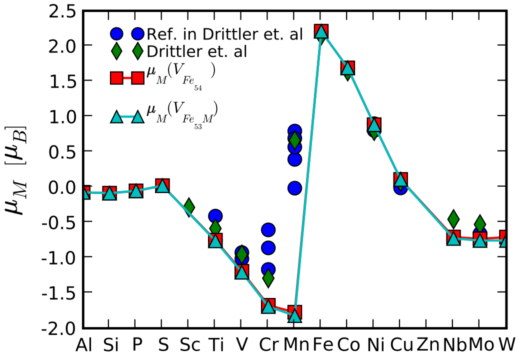

Figure 4.3: Impurity local moments for the locally relaxed, $\mu_M(V_{Fe_{54}})$ and fully relaxed, $\mu_M(V_{Fe_{53}M})$ configurations. They are compared with the local moments reported by Drittler, et~al. [117] and the experimental local moments reported therein.

and experimental values. Also, the high value of density of states for Mn suggests that a slightly different structure is more stable (possibly a slightly larger lattice parameter, or a ferromagnetic coupling with the host bcc-Fe lattice, or both).

4.3.6 Total magnetization

The magnetization of the locally and fully relaxed $Fe_{53}M$ supercells are given in Table 4.1. The change in magnetization for the locally and fully relaxed impurity substituted supercells is shown in Figure 4.4. Though the magnetization of the fully relaxed supercell is always higher than that of the locally relaxed supercell (except for Si, P and S), both curves show a similar qualitative behavior. The change in total magnetization of the supercell can be accounted by a substitution effect and a volume effect.

The change in the electronic band structure brought about by the introduction of the impurity atoms into pure bcc-Fe accounts for the major change in magnetization (Figure 4.1). Even though the impurity moment decreases going from Ti to Mn, the total magnetization increases. This is similar to the finding of Drittler et al. [117] and has been discussed in more detail therein.

In a truly local moment picture, a loss of a single Fe atom from the supercell should lead to a loss of about 2.1 μ_B if the impurity is non-magnetic. While this is not the case for Al, Si and P, S and Cu show the expected loss. Hybridization of the metalloid p-orbitals with the neighboring Fe d-orbitals renders the d-electrons ineffective to contribute to the magnetic moment. This explains the loss of about 4 μ_B in the case of Al.

The change in magnetization of the fully relaxed supercell with respect to the locally relaxed supercell can be explained by the change in magnetization of a

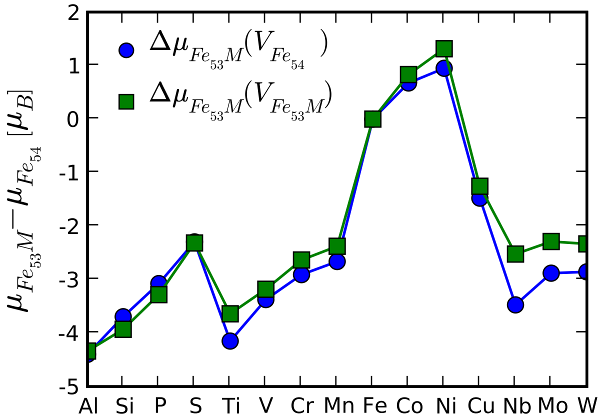

Figure 4.4: Change in total magnetization of locally and fully relaxed impurity substituted $Fe_{53}M$ supercells with respect to pure bcc-Fe, Fe_{54} supercell.

pure bcc-Fe supercell with volume. The change in magnetization of a pure bcc-Fe supercell with volume is shown by the broken line in Figure 4.5. Assuming the band structure of the impurity substituted supercell does not change on volume relaxation, the difference in magnetization between the locally relaxed impurity substituted supercell and the fully relaxed impurity substituted supercell should arise due to the change in volume of the supercell. Figure 4.5 shows the plot of the difference in magnetization between impurity substituted locally relaxed and the corresponding fully relaxed supercells against the change in volume. It can be clearly deduced from the plot that the difference in magnetization closely follows the change in magnetization of the iron matrix due to the change in volume of the supercell.

4.3.7 Change in volume

The volumes of the $Fe_{53}M$ supercells for spin polarized and spin non polarized calculations are given in Table 4.1. The change in volume of the supercells relative to the bcc-Fe supercell, Fe_{54} are plotted in Figure 4.6. It can be clearly seen that the changes in volumes of the spin polarized Si and P lead to a decrease in the volume of the supercell, while Al and S do not have an effect on the volume. Going from Ti to Cu in the 3d series all the elements tend to increase the volume of the supercell relative to Fe. Nb, Mo and W from the 4d series are significantly bigger than the 3d elements and hence increase the volume of the $Fe_{53}M$ supercell to a greater extent than the 3d transition elements. Co and Ni also tend to increase the volume of the supercells which is not what one would expect based on size arguments. Hence, this increase in volume should be coming either from magnetic effects or from electronic effects. Magnetic effects can be ruled out as even for the non spin polarized calculations, the volumes of the Co and Ni supercells

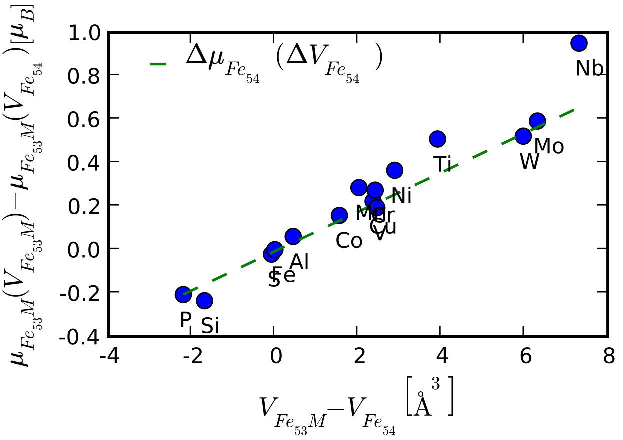

Figure 4.5: Plot of change in magnetization of the fully relaxed $Fe_{53}M$ supercell with respect to the locally relaxed $Fe_{53}M$ supercell. The broken line is a linear fit to the change in the total magnetization with volume of a pure Fe_{54} supercell.

increases with respect to the pure supercell. In fact, the changes in volumes for all the non spin polarized calculations are considerably higher than those for the spin polarized case. This is due to the effect of spin polarization on Fe. Spin polarization causes the volume per Fe atom to increase by about 0.89 $\mathring{A}^3$. Hence, the spin polarized supercell which is already bigger due to spin polarization is able to accommodate the volume changes due to the impurities better than the non spin polarized supercell.

4.4 Conclusion

We calculated the solution enthalpies of alloying elements in bcc-Fe to be used in Chap. 6 and 7. In addition to the solution enthalpies, we also studied the changes in volume and magnetism brought about by the inclusion of impurity atoms in bcc-Fe. Negative moments are induced by the surrounding Fe atoms in the case of Ti, V, Sc, Cu and Zn. In the case of Cr, Mn, Ni and Co an intrinsic magnetic moment exists. The total magnetism of the impurity substituted supercells changes as if the change in magnetism is brought about completely due to the change in the volume of the supercell.

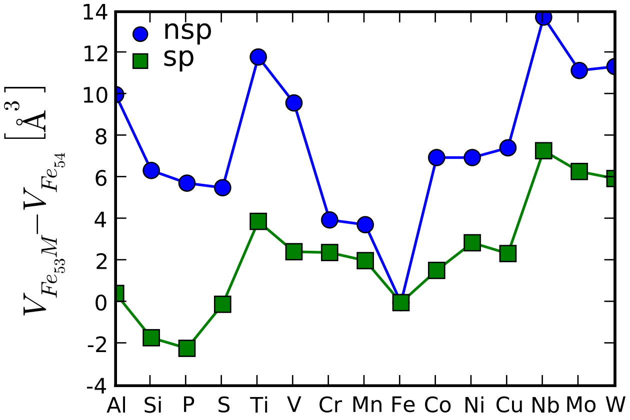

Figure 4.6: Change in volume of the $Fe_{53}M$ supercell relative to the Fe_{54}. Circles represent the changes in volume for a non spin polarized (nsp) calculation while the changes in volume for a spin polarized (sp) calculation are given by the squares.

Chapter 5

Diffusion of carbon in bcc-Fe in the presence of Si

5.1 Introduction

Knowledge about the diffusion of carbon, both in the metallic matrix [121–123] and within precipitated carbide phases [124] is important for understanding the steel making process. It is known that diffusion of carbon, and other interstitial species, is strongly affected by the presence of other alloying elements [125–130] one of the most important alloying elements widely used in TRIP steels is Si. Most of our current understanding on the effect of alloying elements on interstitial diffusion is derived from sophisticated mechanical spectroscopic measurements, especially those based on Snoek damping, augmented with atomistic modeling using fitted solute-interaction parameters [131–136]. These intuitively developed atomic models of diffusion and solute interactions can be verified against solute interaction energies, diffusion activation energies and attempt frequencies derived from ab-initio calculations [121, 137–140]. In addition, they also provide an opportunity for deeper understanding of the diffusion processes at the atomic level. Apart from this practical significance, atomic diffusion is the rate limiting step in many processes. Experimentally, Si is known to affect the Snoek damping peak associated with C in bcc Fe [128, 133, 141] and it is also known to influence the precipitation of carbides [142, 143]. Hence, this work derives its significance both from the practical point of view and also from a much more fundamental point of view.

First, individual solute atoms, C and Si in bcc-Fe are examined. This reveals the most stable configurations of C and Si atoms in bcc-Fe. Then, we compute the energetics of bringing the solute atoms C and Si into close proximity in bcc-Fe. This tells us the effect of Si on the arrangement of C around it. Third, the most stable configurations obtained in the first and the second steps are used to determine the energy barriers of the transition states for carbon diffusion in iron rich Fe-C and

Fe-Si-C respectively through climbing-image nudged elastic band (CI-NEB) calculations. Only the energetics of C, Si and both in bcc-Fe and the diffusion energy barriers for C in the presence of Si will be discussed in this thesis.[1]

The interaction energies of C around Si in bcc-Fe are used to derive the chemical potential of C far away from it in the bcc-Fe matrix. The energy barriers for C diffusion in the presence of Si are used further in KMC simulations. Only a summary of these results is given in this thesis; details can be obtained from Ref. [144].

5.1.1 Computational Details

The electronic calculations used the projector augmented wave (PAW) method [38] as implemented in the Vienna ab initio simulation package [108, 109, 145] (VASP). The exchange correlation potential was of the generalized gradient approximation (GGA) type as formulated by Perdew and Wang [110]. Integrations in reciprocal space were performed by sampling with Monkhorst-Pack grids; for the 54 atom 3×3×3 bcc cell we used a grid where 6 divisions were made along the reciprocals of the **a**, **b**, and **c** axes. Precision was set to "medium". For the 128 atom 4×4×4 bcc cell a k-point grid was used with 4 divisions along the reciprocals. In all calculations the electronic wave functions were expanded in terms of plane waves up to a cutoff kinetic energy of 400 eV. The convergence criteria for energy and force were 0.1 meV and 100 meV/nm, respectively. Structural optimizations were re-initiated at least 2 times.

The minimum energy path of carbon atoms between neighboring interstitial sites was computed with the climbing-image nudged elastic band (CI-NEB) method using the transition state package developed by Henkelman and Jónsson [146, 147]. Images were kept separate using a spring force constant of 500 eV/nm^2.

5.2 Results and Discussion

5.2.1 C and Si in bcc-Fe

For pure ferromagnetic bcc Fe results concerning lattice parameter (a_{bcc}=0.283 nm) and magnetization per Fe atom (m_{Fe}=2.21 μ_B) are almost identical to those reported in the careful study of Jiang and Carter [137] who used the same software and the same Fe and C PAW potentials as in this study.

For the C atom in the octahedral ($\frac{1}{2}00$) and tetrahedral ($\frac{1}{2}\frac{1}{4}0$) positions we also obtained similar energy differences, with the octahedral site in this work being favored by about 0.83 eV. As mentioned by Jiang and Carter [137], the tetrahedral position is the saddle point along the minimum energy path (MEP) connecting neighboring octahedral positions. Therefore, the energy difference between the octahedral and tetrahedral positions corresponds to the activation energy for diffusion on the octahedral sublattice. The activation energy calculated here, 0.83 eV,

---

[1] The rest was carried out by my collaborators.

compares well with other DFT results 0.90 - 0.92 eV [138, 139], and 0.86 eV [137]. Our number agrees fortuitously well with the experimentally measured activation energies reported in the literature of 0.87 eV [148], 0.88 eV [149], 0.82 eV [150], 0.83 eV [151]. More recent Snoek type measurements have given a similar activation energy of 0.84 eV [125, 143]. For completeness, the energy of substitutional C was computed as well. It is found to be about 2.22 eV above that of octahedral C, so that under near equilibrium conditions the occurrence of substitutional C can be ruled out. Another theoretical study [139] reported a similar high energy of 1.97 to 2.37 eV for substitutional C.

The magnetization of supercells Fe_{54} and $Fe_{54}C$, with C in the octahedral interstice, were found to be the same. This indicates that C in low concentrations in the octahedral interstices has little effect of the magnetic properties. Nevertheless, when we define the local moments as the spin density integrated over the Voronoi atomic volumes, we find that the local moments of Fe are clearly affected near the interstitial C atom. The two Fe atoms at the nearest neighbor positions ($[\frac{1}{2}0\ 0]$ in unrelaxed configuration) from the octahedral C atom have local moments that are reduced by about 0.5 μ_B, the four Fe atoms at the 2^{nd} neighbor ($[\frac{1}{2}\frac{1}{2}0]$ unrelaxed) are unaffected, while the eight Fe atoms at the 3^{rd} neighbor ($[1\ \frac{1}{2}0]$ unrelaxed) have local moments that are enhanced by about 0.14 μ_B.

When C is in the tetrahedral interstice (the transition state), the magentic moment of the four nearest neighbor Fe atoms ($[\frac{1}{2}\frac{1}{4}0]$ unrelaxed) are reduced by 0.6 μ_B while it increases on the four Fe atoms at the 2^{nd} nearest neighbor positions ($[\frac{3}{4}\ \frac{1}{2}0]$ unrelaxed) by about 0.2 μ_B. The net effect of carbon on the magnetization m is nil while it is in the octahedral interstice, while the magnetization m is reduced by about 1.5 μ_B per carbon atom in the tetrahedral interstitial transition state. This means that the activation energy for carbon diffusion is affected by an applied magnetic field. When the local moments and the applied field are aligned, the activation energy for diffusion is increased by ΔmB, where $\Delta m = 1.5\,\mu_B = 87\,\mu eVT^{-1}$, and where B is the magnetic field. In order to have a 0.1 eV change in the activation energy a field of 1150 T would be required, which is about one order of magnitude greater than the 2006 world record in a non-destructive experiment [152].

The single Si impurity calculations clearly indicate that Si dissolves substitutionally because it is energetically much more favorable than the octahedral and tetrahedral interstitial positions (see Table 5.1). The Fe-Si nearest neighbor pairs around the substitutional Si atom are slightly elongated (about 0.4 %), indicating that Si in the metallic environment of Fe is just slightly larger than Fe itself. This immediately indicates that Si is too large to fit in the interstitial positions. Si is indeed experimentally known to be a substitutional alloying element. The bcc lattice parameter of Fe-Si solid solutions is observed to be only weakly dependent on the Si concentration over a large range of compositions [153,154], confirming our finding that Si has a size very close to that of the Fe in which it dissolves.

Based on the above findings, we have considered the interaction between Si and C in terms of Si-C pairs where the Si atom is always substitutional and the C atom is always in the octahedral interstice.

5.3 C-Si interactions in bcc-Fe

As apparent from the Table 5.1 and Fig. 5.1, the effective interactions between Si and C are strongly dependent on the distance, they are repulsive at distance less than about a bcc lattice parameter, weakly attractive between 1 and 1.5 times the lattice parameter, and tend to become weak at greater distances. The repulsion at short distances is no surprise; Si is slightly larger than Fe, so in its vicinity there is less room in the interstitial positions. The attractive effective interactions at slightly larger distance might appear surprising, but they too can be reasoned. While the first nearest neighbor Fe-Si pairs are a little elongated, the second neighbor Fe-Si pairs are a little shortened because the squares formed by first nearest neighbors are a little expanded. Therefore just beyond a distance of about one bcc lattice parameter the octahedral interstices are a little less flattened than those in the unperturbed pure Fe crystal structure. Naturally, the C atoms fit a little better here. This attraction is thus an elastic effect. In any case, the attraction is not very strong, at most about 0.10 eV when Si and C are separated by a vector $[\frac{3}{2}00]$. Fig. 5.1 and Table 5.1 indicate that the effective interaction is not only a function of distance, but also of the particular vector R: the interaction for $[\frac{3}{2}00]$ differs from that for $[11\frac{1}{2}]$ while they are equidistant.

The interaction between Si and C causes variation in the fraction of octahedral interstitial sites that are occupied by carbon, depending on the distance to a Si atom. Beyond the 6^{th} nearest neighbor Si-C interactions are negligible so that we may safely assume that the fraction carbon in those shells is the same as at infinite distance from a Si atom. We first discuss the thermodynamic equations governing the distribution and chemical potential of C around Si and then discuss our results with reference to these relations.

We define a solute excess energy[2] ,

$$\Delta E(X) = E(\mathrm{Fe}_n X) - nE(\mathrm{Fe}), \tag{5.1}$$

The effective interaction energy J between two solute atoms X and "Y" at a certain distance $\mathbf{R}_s$ from each other may be defined as

$$J^{XY}_{\mathbf{R}_s} = \frac{1}{m}\left[E(\mathrm{Fe}_n XY, \mathbf{R}_s) - nE(\mathrm{Fe}) - \Delta E(X) - \Delta E(Y)\right], \tag{5.2}$$

where s indicates a particular neighbor shell and where the multiplicity m takes care of the fact that the finite size and the periodicity of the cell causes the interaction to occur multiple times in a cell for certain $\mathbf{R}_s$. An example for the 333 cell is the interaction between a substitutional Si at [000] and an octahedral C at $[\frac{3}{2}00]$, where the C atom has another Si neighbor at [300] so that $m = 2$.

---

[2] where, for reasons of optimal error cancellation, all energies, including the energy per Fe atom, $E(\mathrm{Fe})$, are obtained from supercells with the same dimensions. Here, supercells consisting of 3×3×3 and 4×4×4 bcc cubes were used.

Composition	Position C $[a_{bcc}]$	Position Si $[a_{bcc}]$	ΔE [eV/cell]	J_{SiC} [eV]
Fe_{54}				
$Fe_{53}C$	[0 0 0]		-6.134	
$Fe_{54}C$	$[\frac{1}{2} 0\ 0]$		-8.356	
$Fe_{54}C$	$[\frac{1}{2} \frac{1}{4} 0]$		-7.524	
$Fe_{53}Si$		[0 0 0]	-6.528	
$Fe_{54}Si$		$[\frac{1}{2} 0\ 0]$	-1.507	
$Fe_{54}Si$		$[\frac{1}{2} \frac{1}{4} 0]$	-1.729	
$Fe_{53}SiC$	$[\frac{1}{2} 0\ 0]$	[0 0 0]		0.478
$Fe_{53}SiC$	$[\frac{1}{2} \frac{1}{2} 0]$	[0 0 0]		0.750
$Fe_{53}SiC$	$[1\ \frac{1}{2} 0]$	[0 0 0]		-0.021
$Fe_{53}SiC$	$[1\ \frac{1}{2} \frac{1}{2}]$	[0 0 0]		-0.057
$Fe_{53}SiC$	$[1\ 1\ \frac{1}{2}]$	[0 0 0]		-0.044
$Fe_{53}SiC$	$[\frac{3}{2} 0\ 0]$	[0 0 0]		-0.101
$Fe_{53}SiC$	$[\frac{3}{2} \frac{1}{2} 0]$	[0 0 0]		0.016
$Fe_{53}SiC$	$[\frac{3}{2} 1\ 0]$	[0 0 0]		-0.021
$Fe_{53}SiC$	$[\frac{3}{2} 1\ \frac{1}{2}]$	[0 0 0]		-0.021
$Fe_{53}SiC$	$[\frac{3}{2} 1\ 1]$	[0 0 0]		-0.035
$Fe_{53}SiC$	$[\frac{3}{2} \frac{3}{2} 0]$	[0 0 0]		-0.013
$Fe_{53}SiC$	$[\frac{3}{2} \frac{3}{2} 1]$	[0 0 0]		-0.016
$Fe_{53}SiC$	$[\frac{1}{2} 0\ 0]$	$[\infty\ \infty\ \infty]$		0.000

Table 5.1: Excess solute energies ΔE (Eq. 5.1) and effective Si-C interactions J_{SiC} (Eq. 5.2). Composition indicates which atoms are present in the supercell, positions are given in units of the bcc-Fe lattice parameter.

Interaction between Si and C atoms can cause correlations. Given the rather high solubility of Si in bcc Fe, at low concentrations Si must form a random solid solution in bcc Fe where the individual Si atoms are far apart from each other. Carbon atoms, which diffuse much more easily than Si atoms, see below, will arrange themselves around the Si atoms. Fig. 3 of Ref. [144] shows that carbon fractions are drawn to the 4^{th}, 5^{th}, and 6^{th} neighbor shells, and are strongly repelled from the 1^{st} and 2^{nd} shells around Si atoms. Although the attraction is much weaker than the repulsion, on the whole Si atoms attract C, so that the fraction of C at infinite distance from Si is below what it would have been if no Si were present. Therefore, Si effectively decreases the C concentration far away from the Si atoms, and lowers the C chemical potential. This means that C segregation towards Si increases the solubility of C in bcc Fe and suppresses the formation of carbides in bcc Fe.

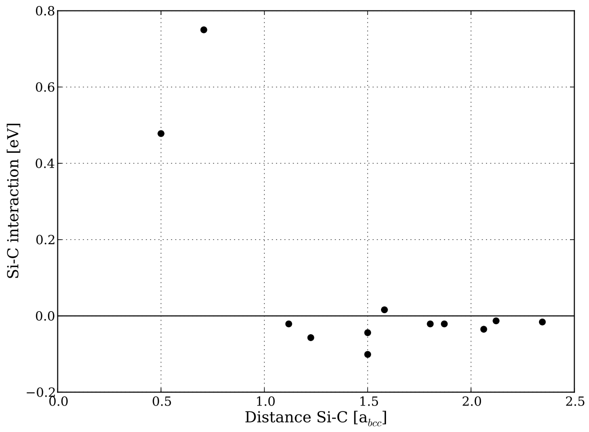

Figure 5.1: Interaction energy between substitutional Si and octahedral C in bcc-Fe as a function of distance in units of the bcc lattice parameter.

5.4 Activation energy barriers for diffusion

Fig. 5.2 shows the minimum energy path for octahedral carbon diffusion in bcc Fe in the absence of Si. In Fig. 5.2a the carbon atom moves between nearest neighbor octahedral positions such as $[\frac{1}{2}0\ 0]$ and $[\frac{1}{2}\frac{1}{2}0]$. The saddle point then occurs at a tetrahedral position ($[\frac{1}{2}\frac{1}{4}0]$) with an activation energy of 0.83 eV. We have also considered C jumps between non-nearest neighbor octahedral interstices in bcc Fe without Si. The MEP between the second neighbor octahedral sites $[\frac{1}{2}0\ 0]$ and $[0\ \frac{1}{2}0]$ always converged to a path with the octahedral $[\frac{1}{2}\frac{1}{2}0]$ site as intermediary. In other words, the jump between second nearest neighbor sites is really two times a nearest neighbor jump, from $[\frac{1}{2}0\ 0]$ to $[\frac{1}{2}\frac{1}{2}0]$ and from $[\frac{1}{2}\frac{1}{2}0]$ to $[0\ \frac{1}{2}0]$. The MEP between third neighbor octahedral sites $[\frac{1}{2}0\ 0]$ and $[0\ \frac{1}{2}\frac{1}{2}]$ could be found however, and it is displayed in Fig. 5.2b. It has a very high activation energy of 1.61 eV, so that the three nearest neighbor jumps that connect these sites, e.g. from $[\frac{1}{2}0\ 0]$ to $[\frac{1}{2}\frac{1}{2}0]$ next to $[0\ \frac{1}{2}0]$, and next to $[0\ \frac{1}{2}\frac{1}{2}]$, have a much greater likelihood of occurring.

In the presence of Si, the nearest neighbor activation energies are dependent on the proximity of Si. The jumps between second and third nearest neighbors, as shown in Fig. 5.3b and 5.3c always reverted to a sequence of nearest neighbor jumps. The minimum energy pathway (MEP) for the nearest neighbor jump immediately next to a substitutional Si atom, as shown in Fig. 5.3a, is displayed in Fig. 5.4. For the C jumping from $[\frac{1}{2}0\ 0]$ to $[\frac{1}{2}\frac{1}{2}0]$, the barrier does not connect points at equal energy because the $[\frac{1}{2}0\ 0]$ site for C is energetically favored over the $[\frac{1}{2}\frac{1}{2}0]$ site by about 0.3 eV, as is apparent from Table 5.1 also. The activation energy for diffusion is affected also, it is now direction dependent: it is about 0.65 eV from right to left (i.e. from $[\frac{1}{2}\frac{1}{2}0]$ to $[\frac{1}{2}0\ 0]$), and about 0.95 eV in the opposite direction. Fig. 5.4 shows all the distinct jumps between octahedral interstices around a single

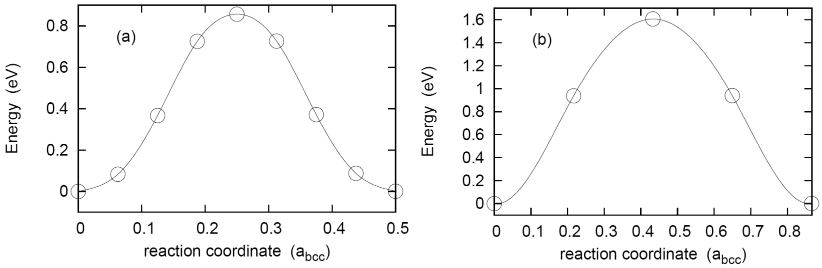

Figure 5.2: Minimum energy paths for C diffusion in bcc-Fe: (a) C from $[\frac{1}{2} 0\ 0]$ to $[\frac{1}{2} \frac{1}{2} 0]$; (b) C from $[\frac{1}{2} 0\ 0]$ to $[0\ \frac{1}{2} \frac{1}{2}]$.

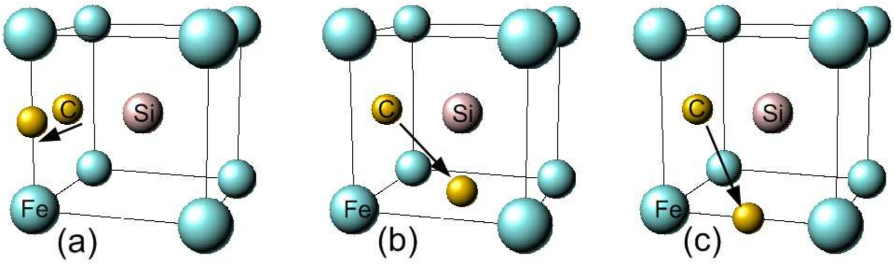

Figure 5.3: Minimum energy paths for C diffusion in the presence of a single substitutional Si atom in bcc-Fe: the Si atoms located at the origin [0 0 0], (a) C from $[\frac{1}{2} 0\ 0]$ to $[\frac{1}{2} \frac{1}{2} 0]$; (b) C from $[\frac{1}{2} 0\ 0]$ to $[0\ \frac{1}{2} 0]$; (c) C from $[\frac{1}{2} 0\ 0]$ to $[0\ \frac{1}{2} \frac{1}{2}]$.

substitutional Si atom in a 3×3×3 bcc cell.

5.5 Kinetic Monte Carlo simulations

Kinetic Monte Carlo (KMC) simulations employing kinetically resolved activation barrier (KRA) and attempt frequencies determined using transition state theory (TST) lead to the following observations [144].

First, Si reduces carbon diffusivity remarkably, especially at low temperature. Just 2 at. % Si substitutionally dissolved in bcc Fe reduces the C diffusivity by almost 39 % at 500 K and by 14 % at 1000 K.

Second, there are two mechanisms by which Si reduces the diffusivity of C: a) the first and second neighbor shells around Si are so high in energy that C is blocked from these sites, this reduces the number of positions through which C can diffuse (labyrinth mechanism); and b) at slightly greater distances C gets weakly trapped around Si so that it remains immobilized for some time, depending on the temperature (trapping mechanism [134]). Since KMC simulations allow us to switch different interaction parameters on or off we can precisely pinpoint the contribution of each mechanism and their influence on diffusivity can be determined.

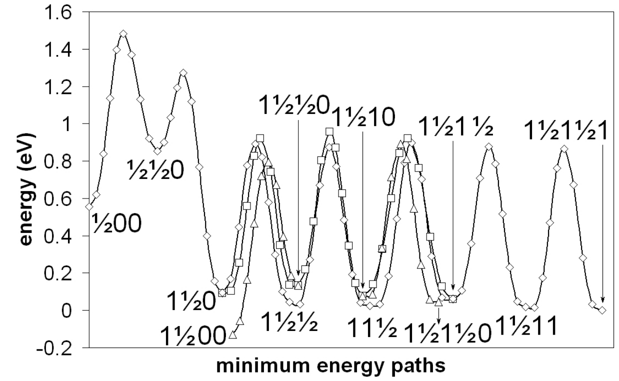

Figure 5.4: Carbon diffusion paths in the presence of a single substitutional Si atom in bcc-Fe: Si at [0 0 0], C jumping between various nearest-neighbor octahedral interstices.

When the attractive Si-C interactions in the third through sixth shells are set to zero, the C diffusion in Fe with 2 at. % Si is reduced by 10% both at 500 K and at 1000 K. This indicates that at 1000 K the labyrinth mechanism is the most important one. When instead simulations are repeated whereby the repulsive Si-C interactions in the first and second shells are set to zero, diffusivity in Fe with 2 at. % Si reduced by 35% at 500 K and by 8 % at 1000 K. This indicates that at 500 K the trapping mechanism is dominant, but that at 1000 K labyrinth and trapping mechanisms contribute about equally.

5.6 Conclusion

It has been shown that the interstitial site preference and the diffusion of C in ferromagnetic bcc-Fe can be accurately computed through density functional electronic structure calculations. The activation energy for diffusion agrees well with consensus experimental assessments. The interaction between Si and C strongly depends on distance, it is strongly repulsive for the first and second shell around the Si atom, weakly attractive in the third up to and including the sixth shell, and essentially vanishing beyond the sixth shell. The weak attraction causes a C enriched “cloud” around Si atoms at ambient and intermediate temperatures. This reduces the C concentration away from the Si atoms, so that in the presence of low Si concentrations the chemical potential of C is reduced. Therefore, at low concentrations Si diminishes the thermodynamic driving force for carbide formation. The Si-C interaction is reflected also in the influence of Si on the C diffusivity: (I) at high temperatures of about 1000 K, the strong repulsion between C and Si in the first and second neighbor shells plays an important role. This causes a mild reduction in the C diffusivity because there are fewer diffusion paths as C is blocked from sites very close to Si. (II) at lower temperatures of about 500 K, the energetically weaker attraction plays a dominant role in reducing the diffusivity of C through entrapment of C at a large number of interstitial sites in the vicinity of Si. At 500 K, 1 at. % of Si in solution may reduce the diffusivity by as much as 22% relative to Si-free bcc Fe.

The experience that Si suppresses or retards carbide formation [142, 143] now can be understood to have two aspects: a) by attracting and trapping the C chemical potential is reduced, reducing the driving force for carbide precipitation and b) by reducing the diffusivity of C the precipitation of carbides is slowed down. Both effects are sensitive to temperature because Si traps C only weakly.

Chapter 6

First-principles prediction of partitioning of alloying elements between cementite and ferrite

6.1 Introduction

Cementite is the most common metastable carbide in steel. At room temperature it is ferromagnetic (FM) with a Curie temperature, T_c, of about 483 K [40, 41]. Cementite has an orthorhombic crystal structure represented by Pearson symbol oP16 and space group number 62. It has 12 Fe and 4 C atoms per unit cell [41, 64]. There are two inequivalent Fe positions, viz. the general and the special positions, with the Wyckoff notation 8d and 4c respectively. Carbon atoms also occupy a 4c Wyckoff site. Cementite displays many interesting properties, such as INVAR behavior [49], and is suspected to be a major component of the earth core as well [50]. Cementite can be present in various forms in steel and strongly affects its properties. The (de)stabilization of cementite plays an important role in the secondary hardening of steel [155, 156] and the suppression of cementite by alloying elements is of utmost interest for transformation induced plasticity (TRIP) steels [157,158] and for steels based on the quenching and partitioning process [159]. In low-alloyed steels, the cementite phase usually co-exists with bcc-Fe solid solution phase commonly referred to as ferrite. Therefore, partitioning of alloying elements and cementite (de)stabilization by alloying elements have to be regarded as a balance involving both the cementite and the ferrite phases.

Alloying element partitioning has been investigated in the past by various experimental methods. It has been consistently found that Cr [40, 160–170] and Mn [40, 160–164, 167, 168, 171–176] partition to the cementite phase while Si [40, 160, 161, 164, 167, 171–175, 177, 178] has a higher concentration in the bcc-Fe phase. There also have been, although less extensive, investigations that indicate that Al [179], Co [164] and Cu [176] partition to the bcc-Fe phase while V [40, 162, 164, 173, 180], Mo [40, 163, 164, 167, 173, 181] and W [164, 181] preferably dissolve in the cementite phase. It is not necessary for all the alloying elements to partition either to the bcc-Fe or the cementite phase: depending on the concentration of alloying elements used and the processing conditions, alloying elements like Ti, Nb and V [40, 162, 164, 173, 180] form very stable NaCl type carbide phases; P segregates to grain boundaries [182, 183], and Al might combine with oxygen and nitrogen to form aluminium oxide and aluminium nitride respectively. S is usually bound by Mn in the form of MnS and is not present in appreciable amounts to actually partition to either of the phases. Hence, from the experimental data, partitioning of Ti, P, and S in particular remain rather unclear.

Partitioning has been studied theoretically also by computing enthalpy changes upon substitution of Fe atoms by alloying elements on the Fe sublattices in cementite. The (de)stabilization of cementite by 3d and 4d transition elements was investigated by Shein et al. [184]. They report that Sc, Ti, V, Cr, Zr and Nb stabilize cementite while Ni, Cu, Pd and Ag destabilize it. Jang et al. [87, 185] report that cementite is stabilized by Mn and destabilized by Si. Both Shein et al. [184] and Jang et al. [87,185] attribute the (de)stabilization of cementite to the formation enthalpy of the alloying element substituted cementite. Zhou et al. [186] find a positive formation enthalpy for Cr substituted cementite and they conclude that Cr substitution destabilizes cementite. Medvedeva et al. [187], however, report that Cr substitution increases the cohesive energy, which they interpret as a stabilization of cementite.

In this communication we calculate both formation enthalpies and partitioning enthalpies, as defined below, considering both FM and non-magnetic (NM) cementite with alloying element substitutions. We show that partitioning enthalpies generally describe the partitioning of alloying elements between bcc-Fe and cementite in agreement with experiments while the formation enthalpies do not. Finally, we point to some remaining disparities in the calculated partitioning behavior.

6.2 Methodology

The balance for the formation of alloying element substituted cementite from the elements,

$$(3q-1)Fe + M + qC \rightleftharpoons Fe_{3q-1}MC_q, \tag{6.1}$$

gives the formation enthalpy as,

$$H_f = H[Fe_{3q-1}MC_q] - (3q-1)H[Fe] - H[M] - qH[C], \tag{6.2}$$

where M is an alloying element substituting one Fe atom in cementite ($Fe_{3q}C_q$) to give the alloying element substituted cementite ($Fe_{3q-1}MC_q$). $H[Fe_{3q-1}MC_q]$, etc. are the total enthalpies at 0 K. The pure elements are in their standard states, i.e., Fe is FM with the bcc crystal structure, C in the form of graphite and M in the appropriate crystal structure at ambient temperature and pressure (see Table 6.1).

Previously, Jang et al. [87, 185] and Shein et al. [184] have interpreted the change in the formation enthalpies of alloying element substituted FM cementite with respect to FM cementite,

$$\Delta H_f^{FM} = H_f[Fe_{3q-1}MCq^{FM}] - H_f[Fe_{3q}Cq^{FM}], \tag{6.3}$$

as a gauge whether M partitions to, and stabilizes cementite. As cementite is only a weak ferromagnet with a low Curie temperature it is worthwhile to consider it in NM state also (see below),

$$\Delta H_f^{NM} = H_f[Fe_{3q-1}MCq^{NM}] - H_f[Fe_{3q}Cq^{NM}]. \tag{6.4}$$

In a steel the alloying elements, at sufficiently low concentrations, are generally not in their elemental states, but are dissolved either in bcc-Fe or in cementite. Hence, it is obviously not appropriate to take M in its standard state as a reference state. A more appropriate balance to study the alloying element partitioning and the (de)stabilization of cementite can be given as,

$$Fe_{n-1}M + Fe_{3q}C_q \rightleftharpoons Fe_{3q-1}MC_q + Fe_n, \tag{6.5}$$

where $Fe_{n-1}M$ and Fe_n represent the alloying element dissolved in bcc-Fe and pure bcc-Fe respectively. This gives the partitioning enthalpy per M atom as,

$$H_p = H[Fe_n] + H[Fe_{3q-1}MC_q] - H[Fe_{n-1}M] - H[Fe_{3q}C_q]. \tag{6.6}$$

Stabilization entails a transfer of M from the solid solution of M in bcc-Fe to the cementite phase while destabilization implies that the alloying element remains in the bcc-Fe solid solution. Therefore, the (de)stabilization of cementite has to be regarded as a competition between cementite and bcc-Fe, and the latter contribution is missing from the cementite formation enthalpies defined above. It follows that a (positive) negative H_p, rather than a (positive) negative H_f, implies that the alloying element (de)stabilizes and partitions to (bcc-Fe) cementite.

First-principles density functional calculations yield enthalpies at 0 K. In the case of cementite and bcc-Fe these enthalpies are for the FM state. At the typical tempering temperatures of 600-950 K used in experiments, cementite is no longer in the FM state, while bcc-Fe is still well below its Curie temperature (bcc-Fe, T_C=1043 K). So, it might be more appropriate to use the enthalpy of the disordered magnetic state for cementite. Here, we consider that the enthalpy of magnetically disordered cementite slightly shifts in the direction of that of the NM state. Of course, without actually reaching the NM enthalpy because typically local magnetic moments on Fe atoms persist to well above the Curie temperature. Khmelevskyi et al. [188] have argued that the disordered magnetic state and the NM state in cementite are almost degenerate in energy although they base their argument on the local density approximation. Nevertheless, the FM and the NM enthalpies may be regarded as upper and lower limits for the cementite enthalpy in the vicinity of, and above T_C.

Of course, at finite temperatures the partitioning free energy, rather than the partitioning enthalpy, should be used. One approach to obtain the free energy of partitioning is to use the experimental heat capacity data of cementite with alloying elements. Unfortunately, there is little experimental data on the heat capacity of cementite. Reliable heat capacity data on alloyed cementite is almost non-existent. The second approach is to compute the free energy from first-principles calculations itself. Recently, progress has been made in this area for bcc-Fe [189] and even for pure cementite [56]. It is presently still out of reach for alloying element substituted cementite. However, considering that we expect entropy changes per M atom for the balance in Eq. 6.1 to be a few k_B at most, as is typical of vibrational, configurational and magnetic transitions, and given that the contributions on either side of the balance largely cancel each other, it follows that below 1000 K the entropy contribution (TS) is about 100 meV/atom at most. We will show that for most of the alloying elements the partitioning enthalpy is larger than 100 meV/atom so that definite conclusions can be drawn without specifically considering the entropic contributions.

6.2.1 Computational Details

We used the spin-polarized generalized gradient approximation (GGA) to density functional theory (DFT) [18, 19] and a plane wave basis with a kinetic energy cut-off of 400 eV. The Kohn-Sham equations were solved using the Vienna *ab initio* simulation package (VASP, version 4.6.34) [105, 106, 108, 109]. The valence electron and core interactions were described using the projector augmented wave method (PAW) [38]. The first-order Methfessel-Paxton method was used with a smearing width of 0.1 eV. The PW91 exchange correlation functional [110] with the Vosko-Wilk-Nusair interpolation [112] for the correlation part was used. The relaxations were assumed to have converged when the energy in two consecutive ionic relaxation steps differed by less than 10 μeV. For accurate bulk energies, a final calculation was done without any relaxation using the linear tetrahedron method with Blöchl corrections for smearing. Integrations in reciprocal-space employed Monkhorst-Pack sampling [35] such that the product of the number of k-points in the first Brillouin zone and the number of atoms in the supercell equalled about 10000. Both the k-point density and energy cut-off were verified to give total energy convergence of 1 meV or better.

Pure elements were modeled using the unit cells (or primitive cells when possible) of their respective crystal structures (Table 6.1). Co and Ni were considered FM and Cr was considered anti-ferromagnetic (AFM). It is well-known that current DFT exchange-correlation functionals do not model graphite accurately. To overcome this shortcoming, the total enthalpy of diamond was computed and a correction of -17 meV was added to account for the diamond to graphite transformation [190].

bcc-Fe was modeled with a 54 atom supercell, Fe_{54}, consisting of 3×3×3 bcc-Fe

Table 6.1: Enthalpies at 0 K of the elements in their standard states, $H[M]$.

M	Pearson Symbol	$H[M]$ $[eV/atom]$	M	Pearson Symbol	$H[M]$ $[eV/atom]$
Al	cF4	-3.697	Fe	cI2	-8.208
Si	cF8	-5.432	Co	hP2	-7.015
P	oC8	-5.369	Ni	cF4	-5.464
S	oF128	-4.110	Cu	cF4	-3.728
Ti	hP2	-7.775	Nb	cI2	-10.063
V	cI2	-8.926	Mo	cI2	-10.807
Cr	cI2	-9.470	W	cI2	-12.923
Mn	cI58	-8.982	C	hP4	-9.118

unit cells with a total enthalpy of -443.295 eV at 0 K. The dilute impurity solid solution was modeled by substituting an Fe atom by the alloying element, M, giving a composition $Fe_{53}M$ (see Table 6.2). Reciprocal space integrations employed a 6×6×6 k-point grid.

Cementite was modeled as a unit cell with 16 atoms, $Fe_{12}C_4$, and an 8×6×10 k-point grid was used for integrations. Alloying element substituted cementite was modeled by replacing one of the Fe atoms in the unit cell with the alloying element, $Fe_{11}MC_4$. We considered the alloying element substituting the Fe atom at both the general and the special positions. Both the FM and AFM configurations of the Fe atoms on the two sites were considered.

The magnetic moments on the atoms were calculated by integrating the spin densities inside the PAW spheres of the respective atoms. Finally, enthalpies for NM cementite were calculated by switching off spin-polarization of the atoms.

6.3 Results and Discussion

As dilute substitutional impurities in bcc Fe, Al, Si, P and S have negligible moments, see Table 6.2. Both 3^{rd} and 4^{th} row transition elements having less than 5 d-electrons (Ti, V, Cr, Nb, Mo, W) align AFM with increasing magnitude of moments to the surrounding Fe atoms. Alloying elements with more than 6 d-electrons (Co, Ni) align FM with decreasing magnitude of moments. With the exception of Mn (5 d-electrons), the magnetic moments on all the impurity atoms in bcc-Fe agree well with those reported by Drittler et al. [117]. The magnetic state of Mn in bcc-Fe is sensitive to supercell size. We find that Mn aligns AFM in the 54 atom supercell while it aligns FM in a bigger supercell with 128 atoms.

The magnetic alignment of the alloying elements in cementite, except for Mn, is comparable to that of bcc-Fe. Al, Si, P and S have negligible magnetic moments (Table 6.3). Early transition elements like Ti, V, Cr, Nb, Mo and W align AFM to the surrounding Fe atoms while the late transition elements Co and Ni align FM. While Mn in bcc-Fe aligns AFM (supercell with 54 atoms), it aligns FM with the surrounding Fe atoms in cementite. The magnitude of the magnetic moments on

Table 6.2: Enthalpies at 0 K of bcc-Fe supercells with respect to the Fe_{54} supercell, $\Delta H[Fe_{53}M] = H[Fe_{53}M] - H[Fe_{54}]$ and the magnetic moment on M, μ_M.

M	$\Delta H[Fe_{53}M]$ $[eV]$	μ_M $[\mu_B]$	M	$\Delta H[Fe_{53}M]$ $[eV]$	μ_M $[\mu_B]$
Al	3.751	-0.07	Fe	0.000	2.21
Si	1.661	-0.08	Co	1.069	1.69
P	1.842	-0.05	Ni	2.844	0.89
S	4.314	0.02	Cu	5.217	0.11
Ti	-0.394	-0.76	Nb	-1.992	-0.73
V	-1.453	-1.21	Mo	-2.575	-0.76
Cr	-1.412	-1.69	W	-4.796	-0.76
Mn	-0.522	-1.82			

the alloying elements is larger when substituted at the special positions than when substituted at the general position. The higher number of C atoms surrounding the alloying elements in the general position (3 in the general position vs. 2 in special position) quench the magnetic moments of the alloying elements.

The formation enthalpy of FM cementite ($H_f[Fe_{3q}C_q^{FM}]$) is in good agreement with previous first-principles calculations. While we report a formation enthalpy of 16 meV/atom (Table 6.3), Fang et al. [191] and Hallstedt et al. [56], both using similar methods as in the present communication, reported values of 20.6 meV/atom and 20.7 meV/atom at 0 K respectively. This implies that formation of cementite is unstable with respect to the pure elements. Jang et al. [87, 185], using the FLAPW method and taking the total enthalpy of graphite as obtained from FLAPW as C reference, reported a formation enthalpy of 56 meV/atom. However, as the interplanar interaction in graphite is poorly described in current first-principles methods, like Fang et al. [191] and Hallstedt et al. [56] we prefer using the first-principles computed enthalpy of diamond and making a correction for graphite. Experimentally, Meschel et al. [192] obtained a formation enthalpy of 48.7±11.4 meV/atom at 298.15 K for cementite.

Although $H_f[Fe_{3q}C_q^{FM}]$ determined by us is lower than the experimental value of Meschel et al. [192], the difference between the formation enthalpy of the Si substituted FM cementite with respect to FM cementite (Table 6.3, Figure 6.1) agrees well with the results of Jang et al. [87, 185]. For Si substituted at the special and general sites, we obtain values of 34 and 18 meV/atom respectively, while Jang et al. [87] obtained 34 and 24 meV/atom respectively. The enthalpies of the reference states, $H[M]$, used in calculating the formation enthalpy, H_f, along with the Pearson symbols of their crystal structures are listed in Table 6.1.

The formation enthalpy change, ΔH_f^{FM}, of FM cementite (Figure 6.1), is positive for Si, P, S, Mn, Co, Ni, Cu, Mo and W and negative for Al, Ti, V, Cr and Nb. Previously, Jang et al. [87, 185] and Shein et al. [184] have interpreted this as an indication that Si, P, S, Mn, Co, Ni, Cu, Mo and W stabilize and partition to bcc-Fe while Al, Ti, V, Cr and Nb stabilize and partition to cementite. This is in disagreement with experiments for Al [179], Mo [40,163,164,167,173,181], and W [164,181].

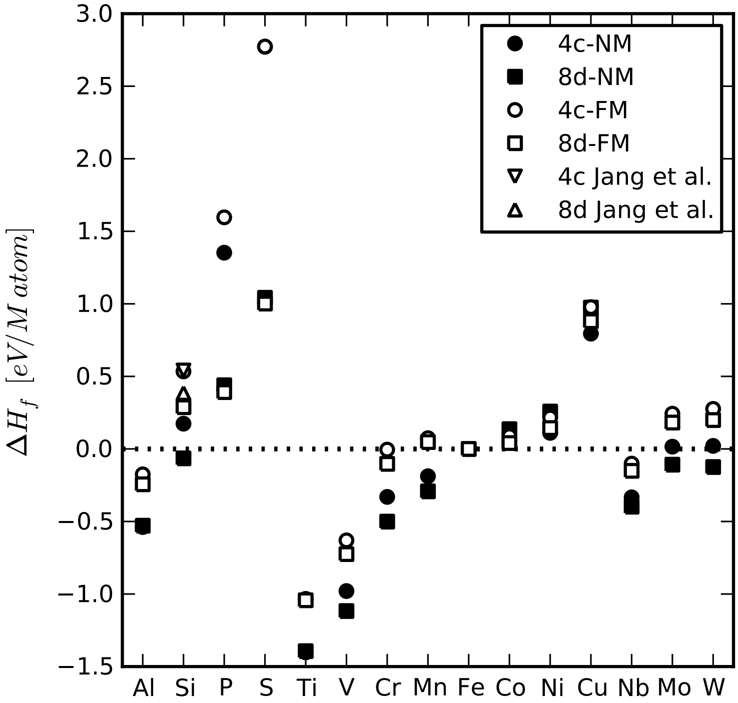

Figure 6.1: Formation enthalpy change of alloying element substituted cementite, ΔH_f.

Table 6.3: Formation enthalpies H_f of the supercells $Fe_{11}MC_4$ at 0 K. Magnetic moments, μ_M, on the alloying elements in cementite are also listed.

M	H_f $[eV]$				μ_M $[\mu_B]$	
	FM		NM			
	4c	8d	4c	8d	4c	8d
Al	0.09	0.02	1.01	1.02	−0.04	−0.04
Si	0.80	0.55	1.72	1.48	−0.04	−0.06
P	1.86	0.65	2.90	1.99	0.01	−0.07
S	3.03	1.26	4.32	2.59	0.00	−0.03
Ti	−0.77	−0.78	0.14	0.15	−0.39	−0.40
V	−0.37	−0.46	0.57	0.43	−0.54	−0.57
Cr	0.26	0.16	1.22	1.04	−0.83	−0.84
Mn	0.34	0.31	1.36	1.25	1.87	1.30
Fe	0.26	0.26	1.55	1.55	1.92	1.83
Co	0.35	0.30	1.60	1.68	1.08	1.00
Ni	0.48	0.40	1.66	1.80	0.30	0.38
Cu	1.24	1.14	2.34	2.52	0.02	0.07
Nb	0.16	0.11	1.21	1.15	−0.36	−0.38
Mo	0.50	0.44	1.56	1.44	−0.30	−0.34
W	0.54	0.46	1.57	1.42	−0.31	−0.33

For Mn the enthalpy changes are so small as to make interpretation ambiguous. While Jang et al. [185] find a slightly negative ΔH_f^{FM} for Mn, we find a slightly positive value. Also, Si is used as an essential alloying element in TRIP steels for its ability to strongly suppress the formation of cementite [193]. Hence, it is surprising that the formation enthalpy of Si, Mo and W substituted FM cementite are comparable. The disagreements with experiments in the case of Al, Mo, W and the comparable formation enthalpy of Si substituted cementite with that of Mo and W substituted cementite clearly show the shortcomings of using formation enthalpies (H_f^{FM}) to determine alloying element partitioning between bcc-Fe and cementite.

To evaluate how stabilization and partitioning might be affected by magnetic disordering in cementite, we consider the extreme case of NM cementite. The formation enthalpy change, ΔH_f^{NM}, (Figure 6.1) gives increased cementite stabilization for all elements. As mentioned above, particularly for Al and Si a movement towards stronger cementite stabilization strongly disagrees with experimental evidence as both Si and Al are used to suppress the formation of cementite in TRIP steels [193].

All the alloying elements prefer the general position over the special position in agreement with previous results [87, 184]. The preference for the general position might be slightly weakened by magnetic disordering because in NM cementite Al, Ti, Co, Ni and Cu prefer to occupy the special position. However, as energy differences between the general and special positions remain small even in the extreme case of completely vanishing magnetic moments we expect the effect to

Table 6.4: Partitioning enthalpies H_p at 0 K.

M	H_p [$eV/M\ atom$]			
	FM		NM	
	4c	8d	4c	8d
Al	0.59	0.52	0.22	0.23
Si	1.65	1.40	1.29	1.05
P	2.59	1.39	2.35	1.44
S	2.56	0.79	2.56	0.83
Ti	−0.21	−0.22	−0.57	−0.57
V	0.10	0.01	−0.24	−0.38
Cr	0.14	0.04	−0.19	−0.36
Mn	−0.18	−0.21	−0.44	−0.54
Fe	0.00	0.00	−0.00	−0.00
Co	0.21	0.16	0.18	0.26
Ni	0.12	0.04	0.01	0.16
Cu	0.24	0.14	0.06	0.24
Nb	0.04	−0.01	−0.20	−0.26
Mo	0.22	0.16	−0.01	−0.13
W	0.36	0.28	0.10	−0.04

be minor.

Table 6.3 and Figure 6.1 show that results derived from formation enthalpies do not indicate partitioning of alloying elements in agreement with experiments. On the other hand, as evident from Table 6.4 and Figure 6.2, the partitioning enthalpy H_p (Eq. 6.6) calculated from total enthalpies of FM cementite correctly indicate that Si, Al, P, S, Co, Ni and Cu partition to bcc-Fe and Ti, Mn and Nb partition to cementite. Although V, Cr, Mo and W are probably incorrectly indicated to partition weakly to bcc-Fe. Magnetic disordering of cementite, as considered through the extreme case of the NM state, is seen to favor stabilization and partitioning toward cementite. It moves the problematic elements V, Cr, Mo and W all in the correct direction of being cementite stabilizers, although W would remain on the bcc-Fe side. In contrast to the formation enthalpy evaluation, Al and Si remain strongly on the bcc-Fe side, as they should. A factor that can influence the experimental findings is whether cementite exists in the presence of austenite. Strong ferrite formers such as V, Mo, and W would segregate more strongly to cementite from austenite than from ferrite.

Consideration of entropy effects, as mentioned earlier, for most elements cannot affect our conclusions. For Ni, Cu and W only is the partitioning enthalpy less than 100 meV/atom so that entropy effects might affect our conclusions at finite temperature. However, even for these elements our results are in agreement with experiments.

Although partitioning of the alloying elements between the bcc-Fe and cementite phases appears correctly described, it fails quantitatively. Experimentally, Cr has a much higher partitioning coefficient towards cementite than Mn [164]. In contrast,

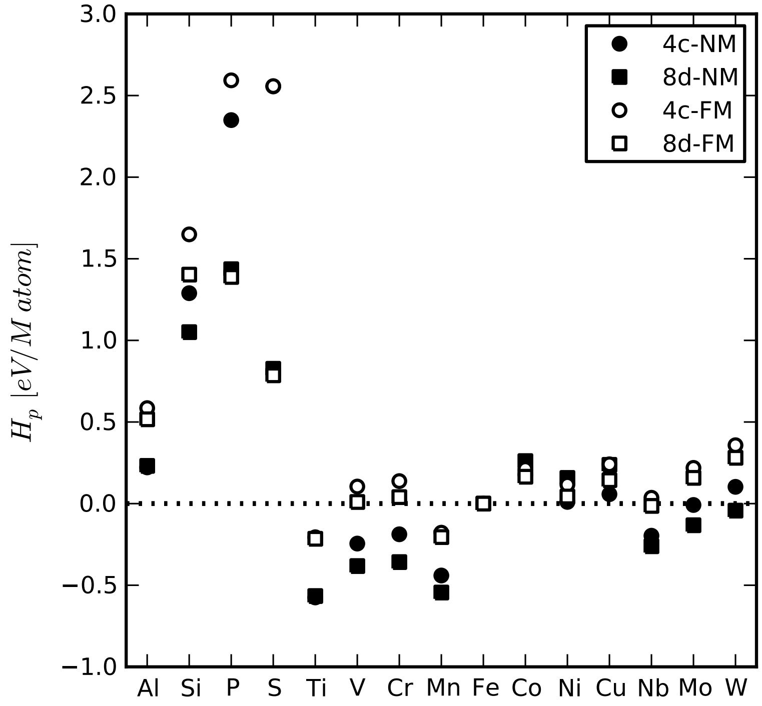

Figure 6.2: Partitioning enthalpies, H_p. For the element S the 4c-FM symbol covers and obscures the 4c-NM symbol.

we find that Mn partitions stronger. Possibly, the experimental finding here too, are affected by the much stronger austenite forming tendencies of Mn than of Cr. Second, in steel where other phases can be present, alloying elements might partition to either bcc-Fe, cementite or any of the other phases and not necessarily just between bcc-Fe and cementite.

6.4 Conclusions

Experimental findings on the partitioning of alloying elements between bcc-Fe and cementite were compared with enthalpies of FM and NM alloying element substituted cementite. Formation enthalpies were shown to not correctly describe the (de)stabilization of cementite by, or the partitioning of alloying elements. The partitioning enthalpy which describes the competition between the cementite and the bcc-Fe phases on the other hand gave results that generally agreed with experimental observations, particularly when the trends as result of magnetic disordering in cementite were considered.

Chapter 7

First-principles calculations on stabilization of iron carbides (Fe_3C, Fe_5C_2 and η-Fe_2C) in steels by common alloying elements

7.1 Introduction

In advanced low alloy steels it is important to retain austenite to ambient temperature and in this regard C acts as an efficient austenite stabilizer. Precipitation of carbides in steel depletes the amount of C available for austenite stabilization and hence it is desirable to suppress the formation of most carbide phases in advanced steels. The most commonly observed carbides in low alloy steels are cementite (Fe_3C), Hägg carbide (Fe_5C_2) and eta-carbide (η-Fe_2C). The easiest way to suppress carbide phases is by adding alloying elements that destabilize them. Therefore, it is of interest to know quantitatively to what degree various alloying elements affect carbide stability. While experimentally it maybe difficult to control and observe the occurrence of very small precipitates of the three carbide structures in steels, it will be shown that it is rather straightforward to compute the main enthalpic contribution of alloying elements to carbide stability by first-principles methods.

Experimentally, it was found that η-Fe_2C forms first in quenched steels at temperatures between 370 and 470 K [42, 43]. But, it was also noticed that ϵ-Fe_2C is the only carbide forming up to 520 K and forms along with cementite till 600 K and that it acts as a precursor for the formation of Fe_5C_2 [44, 45]. A long aging study at 300 K followed by a brief 405 K anneal showed the presence of both η-Fe_2C and

ϵ-Fe_2C [46]. ϵ-Fe_2C is a non-stoichiometric carbon deficient structure of η-Fe_2C. It was recently shown that ϵ-Fe_2C is only slightly more unstable than η-Fe_2C and that it can relax to the latter structure [86]. Above 720 K it has been observed that Fe_3C forms exclusively [42, 43]. Roughly, the carbides appear to precipitate in the order η-Fe_2C, Fe_5C_2 and Fe_3C with increasing temperature [3, 86] with appearance of ϵ-Fe_2C preceding η-Fe_2C. Both kinetic and thermodynamic factors could be responsible for this observation. But, the predominance of each of the carbide in a definite temperature range has been attributed to the lowering of its free energy (and hence stabilization) with temperature [86]. The precipitation sequence can be altered by the application of a magnetic field thereby showing that the magnetic free energy plays an important role in the stabilization of the carbide phases [47, 48, 86].

A number of ab initio studies on pure and impurity substituted cementite have been already performed. Electronic, structural and magnetic properties of pure cementite were described in a number of previous communications [3,53–55]. Furthermore, there are detailed studies of thermodynamic properties of pure cementite [48, 56], elastic properties [57, 59, 60, 63], point defects and possible C diffusion paths [55]. The energetics and electronic structure of impurity substituted cementite have also been the focus of a considerable number of previous studies [54, 58, 87–90, 184, 187, 194–199]. The partitioning behavior of alloying elements between cementite and ferrite has been described [200] and stabilization of cementite by various alloying elements has been studied [58, 87, 89, 184, 186, 194, 195, 197, 198]. In most previous computational work on the stabilization of carbide phases by alloying elements, conclusions were based on enthalpies of formation with respect to the pure carbide phase. Recently, the present authors have argued that carbide stabilization must be evaluated on the basis of partitioning enthalpies instead of formation enthalpies [200].

Relatively less attention has been paid to the carbides Fe_5C_2 and Fe_2C, for both pure and impurity substituted phases. Electronic, magnetic and structural properties of Fe_3C, Fe_5C_2 and η-Fe_2C have been reported [3]. Formation enthalpies [3, 61], surface properties [62], thermodynamic properties along with formation enthalpies [86] of Fe_5C_2 have also been described. Comparable work, excluding the surface properties, has been done on η-Fe_2C [3, 4, 63]. Calculations have been interpreted to show that while Mn and Al stabilize ϵ-Fe_2C, Si destabilizes it [89] To the best of our knowledge no work has been done on the stabilization of either η-Fe_2C or Fe_5C_2 by alloying elements.

In the present communication, adding to our previous work on alloying-element-substituted FeC_3 [200], we calculate the stabilization of Fe_5C_2 and η-Fe_2C by various alloying elements. Therefore, we can now comment on relative stabilization and address the question whether alloying species (dis)favor one carbide in relation to another. Moreover, while we have not considered substitution of the alloying elements on the C site in our previous communication [200], here we consider Al, Si, P and S on the C site of the carbides. To investigate supercell effects on stabilization we consider two supercells, 1×1×1 and 2×2×2, in the case of impurity substituted cementite. We first describe the crystal structures of the carbides, then elucidate the calculation methodology of carbide (de)stabilization , and finally we describe our results on the role of alloying elements on (de)stabilization of the carbides with respect to ferrite and the competition between carbides.

7.2 Methodology

Representing $\mathrm{Fe}_{km}\mathrm{C}_{kn}$ as the pure carbide supercell, where k is the number of formula units used to model the pure $\mathrm{Fe}_m\mathrm{C}_n$ carbide, and $\mathrm{Fe}_{km-1}\mathrm{MC}_{kn}$ as the alloying-element-substituted carbide supercell, the balance for the formation of alloying-element-substituted carbide from the elements is given as

$$(km-1)Fe + M + knC \rightleftharpoons Fe_{km-1}MC_{kn}. \tag{7.1}$$

The formation enthalpy of the impurity substituted carbide is given as

$$H_f[Fe_{km-1}MC_{kn}] = H[Fe_{km-1}MC_{kn}] - (km-1)H[Fe] - H[M] - knH[C] \tag{7.2}$$

where $H\left[Fe_{km-1}MC_{kn}\right]$ is the enthalpy of the alloying-element-substituted cementite. $H[Fe]$, $H[M]$ and $H[C]$ are the enthalpies of the elements (used as reference phases) at their respective room temperature and pressure crystal structures. A similar balance and formation enthalpy applies to the pure carbide, $\mathrm{Fe}_{km}\mathrm{C}_{kn}$ and the C site substituted carbide, $\mathrm{Fe}_{km}\mathrm{C}_{kn-1}\mathrm{M}$.

The stabilization of a carbide by an alloying element is usually given [89, 184] by the change in formation enthalpy of the alloying-element-substituted carbide with respect to the pure carbide as

$$\Delta H_f[Fe_{km-1}MC_{kn}] = H_f[Fe_{km-1}MC_{kn}] - H_f[Fe_{km}C_{kn}] \tag{7.3}$$

or, in terms of compound enthalpies as,

$$\Delta H_f[Fe_{km-1}MC_{kn}] = H[Fe] + H[Fe_{km-1}MC_{kn}] - H[M] - H[Fe_{km}C_{kn}]. \tag{7.4}$$

Similar equations apply for the C site substituted carbide.

To overcome the shortcoming of using the alloying element in its ambient temperature and pressure crystal structure as the reference state we use another quantity defined as the partitioning enthalpy [200]. The partitioning enthalpy looks at stabilization of the carbide phase by the alloying element as a competition for the alloying element between the carbide phase and the ferrite phase. In the carbide phase the alloying element can either occupy the Fe site or the C site. Depending on which site the alloying element occupies, we have two balances that determine the partitioning enthalpy. To compute the partitioning enthalpy for Fe substitution, the balance is given as,

$$Fe_{p-1}M + Fe_{km}C_{kn} \leftrightharpoons Fe_p + Fe_{km-1}MC_{kn}. \tag{7.5}$$

The partitioning enthalpy for Fe substitution is given as,

$$H_p^{(Fe)} = H[Fe_p] + H[Fe_{km-1}MC_{kn}] - H[Fe_{p-1}M] - H[Fe_{km}C_{kn}]) \tag{7.6}$$

where Fe_p, $\mathrm{Fe}_{p-1}\mathrm{M}$, $H[Fe_p]$ and $H[Fe_{p-1}M]$ represent pure bcc-Fe, the dilute solid solution of M in bcc-Fe and their enthalpies respectively.

Similar equations for C substitution are given as,

$$Fe_{p-1}M + \frac{nk-1}{nk} Fe_{km}C_{kn} \leftrightharpoons \frac{np-(n+m)}{np} Fe_p + Fe_{km}C_{kn-1}M. \tag{7.7}$$

$$H_p^{(C)} = \frac{np-(n+m)}{np} H[Fe_p] + H[Fe_{km}C_{kn-1}M] - H[Fe_{p-1}M] - \frac{nk-1}{nk} H[Fe_{km}C_{kn}]. \tag{7.8}$$

A negative value for the partitioning enthalpy implies a stabilization of the carbide while a positive value indicates stabilization of bcc-Fe. The partitioning enthalpy has been recognized as the main driving force for partitioning elsewhere also, e.g. in Eqns. 11 and 14 in the work by Benedek et al. [201]. We will show below that the stabilization of an alloying element substituted carbide with respect to ferrite can be wrongly predicted when using ΔH_f instead of H_p. For the first-principles calculations we consider the (alloying-element-substituted) carbides and (alloying-element-substituted) bcc-Fe in their 0 K ferromagnetic (FM) state.

7.3 Computational Details

We used the spin-polarized generalized gradient approximation (GGA) to density functional theory (DFT) [18, 19] and a plane wave basis with a kinetic energy cut-off of 400 eV. The Kohn-Sham equations were solved using the Vienna *ab initio* simulation package (VASP, version 4.6.36) [105, 106, 108, 109]. The valence electron and core interactions were described using the projector augmented wave method (PAW) [38]. The first-order Methfessel-Paxton method was used with a smearing width of 0.1 eV. The PW91 exchange correlation functional [110] with the Vosko-Wilk-Nusair interpolation [112] for the correlation part was used. Structural relaxations were considered converged when the energy in two consecutive ionic relaxation steps differed by less than 10 μeV and the maximum force (worst case) on any atom in the supercell was less than 40 meV/Å. Both volume and ionic positions were relaxed in all supercells considered. For accurate bulk energies, a final calculation was done without any relaxation using the linear tetrahedron method including the Blöchl corrections [202]. Integrations in reciprocal-space employed evenly spaced Monkhorst-Pack sampling [35] such that the product of the number of k-points in the first Brillouin zone and the number of atoms in the supercell equaled about 10000. Both the k-point density and energy cutoff were verified to give total energy convergence of 1 meV/supercell or better. Pure elements, except Fe see below, were modeled using the unit cells (or primitive cells when possible) of their respective crystal structures. Co and Ni were considered FM and Cr was considered anti-ferromagnetic (AFM). It is well-known that current DFT exchange-correlation functionals do not model graphite accurately. To overcome this shortcoming, the enthalpy of diamond was computed and a correction of -17 meV was added to account for the diamond to graphite transformation [190]. Pure bcc-Fe was modeled with a 128 atom supercell, Fe_{128}, consisting of 4×4×4 bcc-Fe unit cells. We used a 3×3×3 bcc-Fe supercell with 54 atoms in our previous work [200]. The 1×1×1 Fe_3C supercell is the same as its unit cell with 16 atoms and hence modeled as $Fe_{12}C_4$ while its 2×2×2 supercell with 8 unitcells was modeled as $Fe_{96}C_{32}$. Fe_5C_2 was modeled using its unit cell with 28 atoms, $Fe_{20}C_8$. η-Fe_2C was modeled with 2×2×3 unit cells with 72 atoms, $Fe_{48}C_{24}$. Alloying-atom-substituted supercells were modeled by replacing one of the Fe (or C) atoms in the unit cell with the alloying element. We considered the alloying atom substituting the Fe atom on all possible Fe-occupied Wyckoff sites. Al, Si, P and S were also considered on the C site of all the carbides. Alloying-element-substituted iron (ferrite solid solution) was modeled with $Fe_{127}M$. Similarly, alloying-element-substituted Fe_3C, Fe_5C_2 and η-Fe_2C were modeled with $Fe_{11}MC_4$ (or $Fe_{12}C_3M$ or for the 2×2×2 supercell as $Fe_{95}MC_4$ or $Fe_{96}C_{31}M$), $Fe_{19}MC_8$ (or $Fe_{20}C_7M$) and $Fe_{47}MC_{24}$ (or $Fe_{48}C_{23}M$) respectively.

7.4 Results and Discussion

7.4.1 Crystal structure and formation enthalpy of pure carbides

The results are very similar to the ones already reported in Chap. 3 and are therefore skipped here.

7.4.2 Supercell size effects

To investigate the effect of increasing supercell size on partitioning enthalpies and other properties we use supercells of different sizes for both bcc-Fe and cementite. In the case of bcc-Fe we use 3×3×3 and 4×4×4 supercells while for cementite we use 1×1×1 and 2×2×2 supercells. In computing the partitioning enthalpies, the use of either a 3×3×3 or a 4×4×4 supercell of bcc-Fe does not change the partitioning enthalpies except for a few meV in the worst cases indicating that the relaxation effects in a larger bcc-Fe supercell do not differ significantly from that of the smaller bcc-Fe supercell (see Fig. 7.1). But when a larger 2×2×2 cementite supercell is used the partitioning enthalpies changed significantly. While the formation enthalpy and the crystal structure of pure cementite do not show any perceivable changes, the increase in supercell size leads to considerable changes in the partitioning enthalpies of the impurity substituted carbides. This change is clearly noticeable in the case of alloying elements which lead to large changes in volume of the alloying element substituted supercells namely P, S, Nb, Mo and W along with Al and Si when substituted on the C site (see Fig. 7.2). The supercell effect is less pronounced in the case of Ti, V, Cr, Mn, Co, Ni and Cu where the volume change is much less compared to the former group of elements. The increase in carbide supercell size thus generally leads to a less stable carbide and

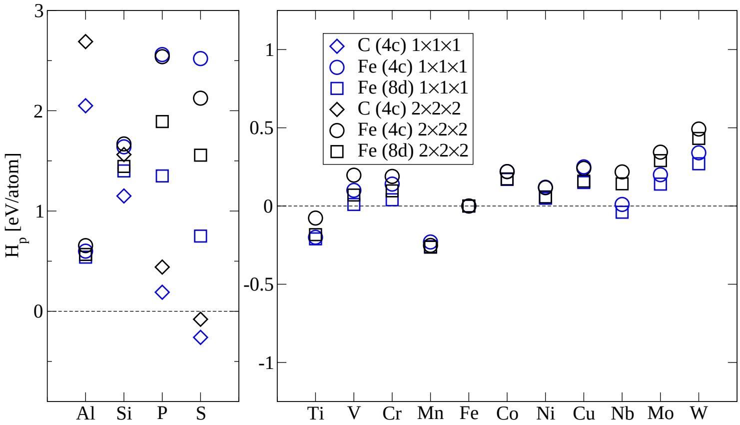

Figure 7.1: Plot illustrating the supercell size effects for cementite. Enthalpies of preference using the 4×4×4 bcc-Fe supercell along with 1×1×1 and 2×2×2 cementite supercells are shown.

hence a stronger preference of the bcc-Fe phase. This is easily rationalized: in the small supercell oversized atoms are accommodated mostly by expanding the volume while in larger supercells the distortion of the carbide lattice predominates. The expansion of the small supercell does not take into account that this volume expansion will lead to elastic strains at larger lengths scales and therefore small supercell calculations energetically might be biased towards the carbide phase unless the actual alloying element concentrations in the carbide are representative for the supercell compositions. In the discussion below we refer to the results calculated using the larger 4×4×4 and the 2×2×2 bcc-Fe and cementite supercells.

7.4.3 Site preference of alloying elements in the carbides

In Fe_3C, when substitution of the alloying elements is considered only on the metal site, all alloying elements prefer to occupy the 8d site [184, 200]. When P and S are substituted on the metal sites it is observed that there is a major reorganization of the nearest neighbor atoms. Fe atoms are seen to move closer to the P and S atoms, both of which have *p* valence electrons. No such reorganization was observed when the transition alloying elements with only *d* valence electrons occupied the Fe site. These observations along with the fact that the C site has the maximum number of Fe neighbors in the carbide structures prompted us to consider P and S along with Al and Si on the C site also. As might be expected, P and S on the basis of the strong bonding with the Fe atoms, preferred the C site over the Fe sites, see Fig. 7.4 and Table 7.2. The case of Si is somewhat ambiguous: in the 1×1×1 cementite supercell there is a clear preference for the C site whereas in the larger 2×2×2 supercell the Fe2(8d) and C sites are almost degenerate, see Fig. 7.1. It should be remarked however, that Si strongly favors dissolution in the

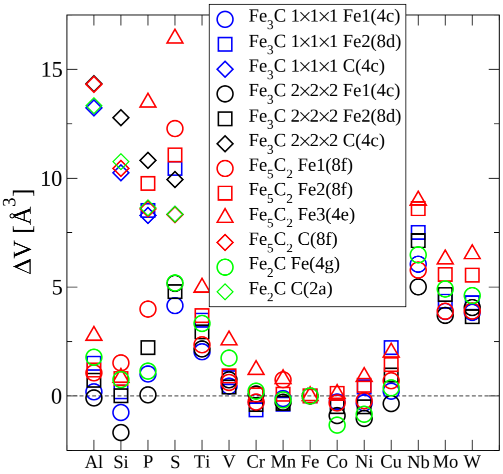

Figure 7.2: Changes in volume of alloying element substituted carbide supercells with respect to the pure carbide supercell.

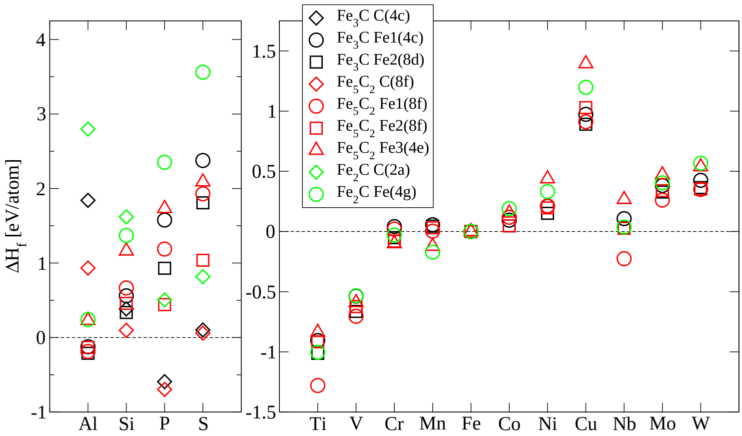

Figure 7.3: Formation enthalpies of alloying element substituted carbides as defined in Eq. 7.3.

	Fe_3C			Fe_5C_2				Fe_2C	
Element	Fe1(4c)	Fe2(8d)	C(4c)	Fe1(8f)	Fe2(8f)	Fe3(4e)	C(8f)	Fe(4g)	C(2a)
Al	-0.12	-0.21	1.84	-0.18	-0.13	0.23	0.93	0.24	2.80
Si	0.56	0.34	0.38	0.67	0.46	1.16	0.10	1.37	1.62
P	1.58	0.93	-0.59	1.19	0.44	1.73	-0.69	2.35	0.50
S	2.38	1.81	0.10	1.93	1.04	2.09	0.06	3.56	0.82
Ti	-0.91	-1.01	-	-1.28	-0.91	-0.84	-	-1.00	-
V	-0.54	-0.66	-	-0.70	-0.62	-0.59	-	-0.54	-
Cr	0.04	-0.05	-	0.02	-0.08	-0.10	-	-0.03	-
Mn	0.06	0.05	-	0.01	0.03	-0.12	-	-0.17	-
Fe	0.00	0.00	-	0.00	0.00	0.00	-	0.00	-
Co	0.09	0.05	-	0.12	0.05	0.16	-	0.19	-
Ni	0.21	0.15	-	0.21	0.20	0.44	-	0.33	-
Cu	0.97	0.89	-	0.91	1.03	1.40	-	1.20	-
Nb	0.11	0.03	-	-0.22	0.03	0.27	-	0.04	-
Mo	0.38	0.33	-	0.26	0.34	0.47	-	0.40	-
W	0.43	0.37	-	0.35	0.35	0.54	-	0.57	-

Table 7.1: Formation enthalpies of alloying-element-substituted carbides with respect to the pure carbide, ΔH_f (eV/atom). The alloying element has been considered on all possible Fe Wyckoff sites of the carbide. Formation enthalpies are calculated as defined in Eq. 7.3 with k=32, 4, 24 for Fe_3C, Fe_5C_2 and η-Fe_2C respectively and with p=128 for bcc-Fe.

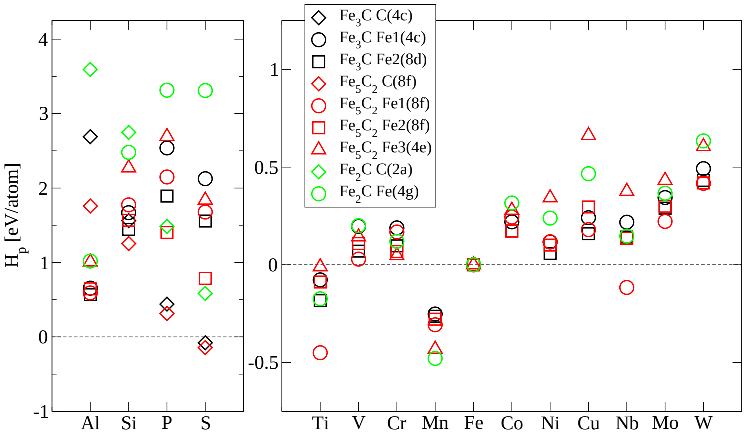

Figure 7.4: Partitioning enthalpies of alloying element substituted carbides as defined in Eq. 7.6 and 7.8.

ferrite phase rather than in cementite. Al is most stable of the Fe2(8d) site. The preference of Al, Si for the Fe site and P, S for the C site from our 2×2×2 supercell calculations agree well with previous results [194] which were carried out at a lower kinetic energy cutoff (350 eV).

In Fe_5C_2, alloying elements prefer various sites (see Fig. 7.4 and Table 7.2). The symmetry of the crystal structure is completely lost only on substitution of the alloying element on the Fe1(8f) or the Fe2(8f) sites. This loss in symmetry leads the atoms constituting the structure to have more degrees of freedom to relax and hence most of the alloying elements prefer to occupy either the Fe1(8f) or the Fe2(8f) site. All carbide formers like Ti, V, Nb and Mo seem to prefer the Fe1(8f) site which has four close C neighbors, two at about 2 Å, third at 2.4 Å and a fourth one at 2.8 Å. Although Al and Cu are not considered good carbide formers they also prefer to occupy this site. Co occupies the Fe2(8f) site with the least number of C neighbors, two at about 2 Å and the third at about 2.4 Å. Ni and W do not show any preference between the Fe1(8f) or the Fe2(8f) sites. The Fe3(4e) site is preferred by Cr and Mn only. Cr and Mn have a stronger affinity for carbon than Fe and tend to be soluble in most carbide phases. The somewhat unique site preference of Cr and Mn may be due to the rather small atomic size difference with Fe, which makes relaxation effects less important, while simultaneously the Fe3 site provides 4 close C nearest neighbors at about 2 Å. As in Fe_3C, Si, P and S prefer to occupy the C site.

In Fe_2C, P and S prefer to occupy the C site whereas Al prefers the Fe site. Although Si prefers the C site in Fe_3C and Fe_5C_2, it prefers the Fe site Fe_2C.

	Fe_3C			Fe_5C_2				Fe_2C	
Element	Fe1(4c)	Fe2(8d)	C(4c)	Fe1(8f)	Fe2(8f)	Fe3(4e)	C(8f)	Fe(4g)	C(2a)
Al	0.66	0.57	2.69	0.59	0.65	1.01	1.76	1.02	3.59
Si	1.67	1.45	1.56	1.77	1.57	2.27	1.25	2.48	2.75
P	2.54	1.89	0.44	2.15	1.40	2.69	0.31	3.31	1.49
S	2.13	1.56	-0.08	1.68	0.79	1.84	-0.14	3.31	0.58
Ti	-0.08	-0.18	-	-0.45	-0.09	-0.01	-	-0.17	-
V	0.20	0.07	-	0.03	0.11	0.14	-	0.20	-
Cr	0.19	0.10	-	0.17	0.07	0.05	-	0.12	-
Mn	-0.25	-0.26	-	-0.31	-0.28	-0.43	-	-0.48	-
Fe	0.00	0.00	-	0.00	0.00	0.00	-	0.00	-
Co	0.22	0.17	-	0.24	0.17	0.28	-	0.32	-
Ni	0.12	0.06	-	0.12	0.10	0.34	-	0.24	-
Cu	0.24	0.16	-	0.18	0.30	0.66	-	0.47	-
Nb	0.22	0.14	-	-0.12	0.14	0.38	-	0.15	-
Mo	0.34	0.29	-	0.22	0.30	0.43	-	0.37	-
W	0.49	0.43	-	0.42	0.42	0.61	-	0.63	-

Table 7.2: Partitioning enthalpies of alloying-element-substituted carbides, $H_p^{(Fe)}$ (eV/atom). The alloying element has been considered on all possible Fe Wyckoff sites of the carbide. Partitioning enthalpies are calculated as defined in Eq. 7.6 and 7.8 with k=32, 4, 24 for Fe_3C, Fe_5C_2 and η-Fe_2C respectively and with p=128 for bcc-Fe.

7.4.4 Volume changes

When fully relaxing the impurity substituted supercell we make the implicit assumption that the supercell under investigation experiences no external stress. While this assumption is valid for massive bulk materials, the assumption must be considered carefully when dealing with precipitate phases such as the ones being considered in the present paper. The precipitates are embedded in a ferrite matrix with which at least partial coherency exists which leads to a strained impurity substituted precipitate phase. Changes in volume of the precipitate phase can increase or decrease the strain. In light of this, it is worthwhile to look at the volume changes brought about by the substitution of the alloying elements on various sites. Situations can be envisaged where although it might be energetically favorable to occupy a certain site the strain effects might not actually allow such preference. Such a situation seems to clearly manifest in the case of Si. Although the preference in energy between the Fe sites and the C site is little, the volume change brought about by its substitution on the C site is much higher than its substitution on the Fe sites (10-15 Å^3 vs. -2.5-2.5 Å^3) (see Fig. 7.2). It is harder to make such an argument in the case of P and S because although the volume changes on the C site are higher compared to the changes on the Fe site, the preference to the C site is much larger compared to Si.

7.4.5 Stabilization of carbides with respect to ferrite

In our previous work [200] we have shown how using ΔH_f to determine stabilization of cementite gives results which do not agree with experiments in the case of Al, Mo and W. The case of Al is striking as it is predicted to stabilize cementite almost twice as much as Mn. Al, of course, does not stabilize cementite while Mn is experimentally known to partition to, and hence stabilize, cementite [163,167,203] (for more references see [200]). In spite of using a 4×4×4 bcc-Fe and a 2×2×2 cementite supercell in the present work instead of the 3×3×3 and 1×1×1 supercells respectively as used in [200], our conclusions about the partitioning and stabilization of the alloying elements between cementite and ferrite remain qualitatively the same when considering partitioning on the Fe site. [1]

In the case of Fe_5C_2, looking at ΔH_f might suggest that Al, Ti, V, Cr, Mn and Nb stabilize the carbide phase while the rest of the alloying elements destabilize it (Table 7.1 and Fig. 7.3). As in the case of cementite, this is a misinterpretation of the data.

However, when we consider the reference states of the alloying elements correctly via the partitioning enthalpies instead of formation enthalpies both Al [179, 204] and Si [163, 164, 167, 173, 205] destabilize the formation of not only cementite but all the carbide phases (see Fig. 7.4 and Table 7.2) regardless of whether Fe or C site substitution is considered. This shows that the conclusions about stabilization of carbides with respect to ferrite based on partitioning enthalpies are more

---

[1] Please note that we list H_f in Table 3 of [200], while in Table 7.1 of the present communication we list ΔH_f.

reliable than the ones based on formation enthalpies. Not only do both Al and Si destabilize all three carbide phases but Si destabilizes them more than Al (see Fig. 7.4).

P, Co, Ni, Cu, Mo and W also destabilize the three carbides considered here, though not nearly as strongly as Si and Al. Surprisingly, S on the C site stabilizes Fe_3C and Fe_5C_2 while destabilizing Fe_2C. Ti and Mn stabilize the three carbide phases while Nb stabilizes cementite and Hägg carbides but not η-Fe_2C. V and Cr destabilize Fe_3C and Fe_5C_2 by a negligible amount while V destabilizes η-Fe_2C.

However, the ab initio computed partitioning enthalpies do not agree with all experimental observations. Cr is know to partition, and hence stabilize, Fe_3C [163, 164, 167]. In fact, more so than Mn. Alas, Cr is computed to slightly destabilize and hence partition away from cementite, contrary to experimental evidence [163, 164, 167]. Possibly, Cr-rich carbides form prior to Fe-based carbides, and act as nucleation sites for the cementite and other Fe-based carbides. If those initial Cr-rich carbides are small enough they might not be recognized as distinct phases. We do compute that Mn stabilizes Fe_3C in agreement with experimental observations [163,164,167,203]. Mn is computed to stabilize Fe_5C_2 and Fe_2C even a little more. Our computed partitioning enthalpies do not reflect correctly the fact that Mo [163, 164, 167] and W [164] also partition to cementite, although the enthalpies involved are rather small. It should be noted that all our calculations are based on enthalpies obtained at 0 K. The neglect of entropy (S) changes at finite temperature is less likely to be tenable when enthalpy changes are of order TS, where S could be mainly due to alloy element induced magnetic (dis)ordering which could be of order k_B. Given that experimental measurements are typically in the neighborhood of the ferrite-austenite transition temperature, it follows that partitioning enthalpies less than 0.1 eV are rather inconclusive.

7.4.6 Relative stabilization of carbides

Si, P, S, and Al, destabilize η-Fe_2C much more than cementite and Hägg carbide. All alloying elements except Mn destabilize η-Fe_2C relative to Fe_3C and Fe_5C_2. At this juncture, it is interesting to note that Mn also stabilizes $\epsilon - Fe_2C$, a carbide closely related to η-Fe_2C, over cementite [89]. The competition between cementite and Hägg carbide is not nearly as strongly affected by alloying additions as the competitions involving η-Fe_2C. Si, Mo and W are found to disfavor cementite less than Hägg carbide, while Ti, Mn, and Nb promote Hägg carbide at the expense of cementite. This is in line with the complete intermixing between Fe_5C_2 and Mn_5C_2 [203], whereas such thermodynamically favorable dissolution does not exist for cementite [88]. It should be remarked though that our results indicate that Mn stabilizes η-Fe_2C and Fe_5C_2 about equally.

It is to be borne in mind that experimental observations pertain to carbides in the paramagnetic state while the first-principles calculations pertain to the ferromagnetic state at zero temperature. While configurational entropy effects can be shown to play a minor role at the temperatures of interest in relation to the computed enthalpy changes, the same cannot be said of magnetic entropies. Possibly, by considering the carbides in a disordered local moment state, and by explicitly considering magnetic entropy contributions to the free energy a better agreement with experiment might be found. Experimentally, there is a possibility for misinterpretations if Cr, V, Mo or W-rich carbides form prior to Fe-based carbides, and then subsequently act as nucleation sites for cementite or other Fe-based carbides. If those initial alloy element-rich carbides are small enough they might not be recognized as distinct phases.

7.5 Conclusion

First-principles calculations on alloying element substituted carbides, Fe_3C, Fe_5C_2 and η-Fe_2C show that Si and Al destabilize the formation of carbides with Si being the most effective. P and S prefer to occupy the C site in all the carbides while Si weakly prefers to occupy the C site in two of them, Fe_3C and Fe_5C_2. On a per atomic fraction basis, Si is about twice as effective as Al for carbide suppression. All alloying elements considered, except Mn, destabilize η-Fe_2C relative to Fe_3C and Fe_5C_2. The competition between Fe_3C and Fe_5C_2 is not so strongly affected by alloying elements. Si, Mo and W disfavor Fe_5C_2 more than Fe_3C, while Ti, Mn, and Nb stabilize Fe_5C_2 over Fe_3C. Mn stabilizes both Fe_5C_2 and η-Fe_2C to a comparable degree over Fe_3C. At finite temperature observed partitioning behavior of Cr, V, Mo and W are not explained satisfactorily on the basis of first-principles zero temperature partitioning enthalpies.

Appendix A

Fourier Series

A Fourier series can be used to represent any periodic function. Given any function $f(x)$ with a periodicity of 2π ($f(x+2\pi) = f(x)$) (Fig. A.1), its Fourier series representation can be written as

$$f(x) = \frac{a_0}{2} + \sum_{1}^{n} a_n \sin nx + \sum_{1}^{n} b_n \cos nx$$

The Fourier series representation of a square and triangle wave forms are given as

$$\begin{aligned}
f_{square}(x) &= \frac{4}{\pi} \sum_{n=1}^{\infty} \frac{\sin(2n-1)x}{(2n-1)} && \text{(A.1)}\\
&= \frac{4}{\pi} \left(\sin x + \frac{1}{3} \sin 3x + \frac{1}{5} \sin 5x + \frac{1}{7} \sin 7x + \dots \right) && \text{(A.2)}\\
f_{triangle}(x) &= \frac{8}{\pi^2} \sum_{n=1}^{\infty} (-1)^{n-1} \frac{\sin(2n-1)x}{(2n-1)^2} && \text{(A.3)}\\
&= \frac{8}{\pi^2} \left(\sin x - \frac{1}{9} \sin 3x + \frac{1}{25} \sin 5x - \frac{1}{49} \sin 7x + \dots \right) && \text{(A.4)}
\end{aligned}$$

A comparison of the original square wave and the Fourier approximation with increasing number of terms in the expansion is show in Figure A.2. It clearly shows that the Fourier series expansion represents the original function more accurately as the number of terms included in the Fourier series expansion increase and tend to infinity.

The coefficients a_n and b_n decrease as $1/n^{m+1}$ if $d^m f/dx^m$ is the lowest order derivative which exhibits discontinuities. So, for a given accuracy (least squares difference) of fitting, 'smoother' functions without discontinuities and jumps have lower number of terms in the expansion compared to functions with discontinuities. Thus, the coefficients in a square wave with jumps and discontinuities decay as $1/n$ (Eq. A.1, Fig. A.1) whereas the coefficients in a triangular waveform with no jumps but only discontinuities decay as $1/n^2$ (Eq. A.3, Fig. A.1).

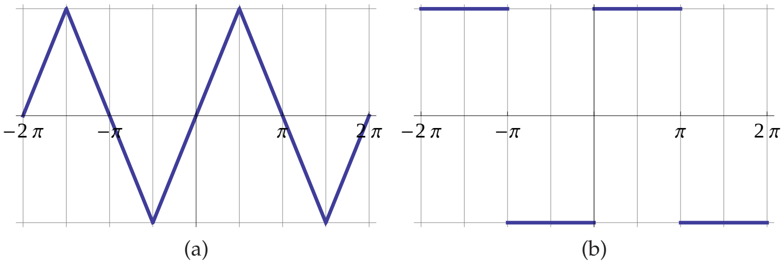

Figure A.1: Triangular (a) and square (b) wave forms. The triangular waveform has discontinuities at -$3\pi/2$, $-\pi/2, \ldots$ while the square wave has discontinuities and jumps at -2π, $-\pi, \ldots$

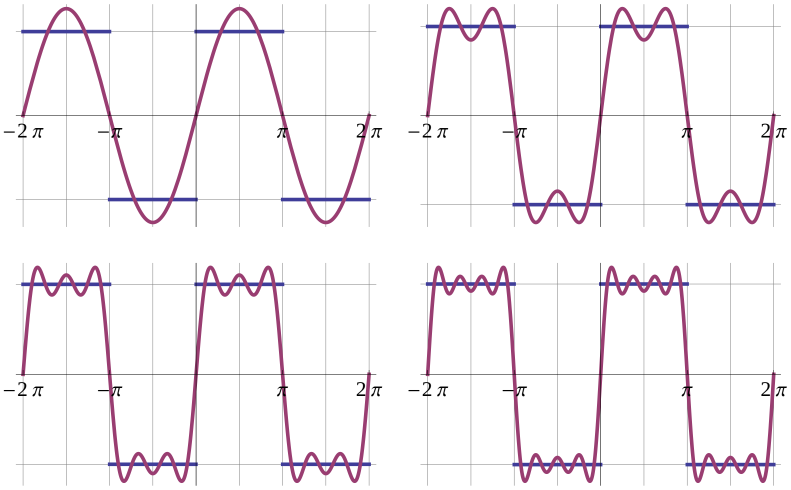

Figure A.2: The first four partial sums of the Fourier series for a square wave.

A Fourier series with a finite number of terms gives the best least squares approximation possible to $f(x)$; it does not mean that a better least squares approximation of a type different from a Fourier series cannot be found.

The idea of a Fourier series expansion can be taken as an analogy for the representation of wavefunctions using a basis set. In a Fourier series expansion, $\sin nx$ and $\cos nx$ terms act as the basis sets for the representation of periodic functions whereas atomic and molecular orbitals act as basis sets in the representation of wavefunctions.

Bibliography

[1] T. B. Massalski and D. E. Laughlin, Calphad **33**, 3 (2009). 2, 33

[2] Wikipedia, *Bainite — Wikipedia, The Free Encyclopedia* (2013). 3

[3] H. I. Faraoun, Y. D. Zhang, C. Esling, and H. Aourag, J. Appl. Phys. **99**, 093508 (2006). 2, 34, 35, 88

[4] C. M. Fang, M. A. van Huis, and H. W. Zandbergen, Scr. Mater. **63**, 418 (2010). 2, 34, 35, 43, 88

[5] B. D. Cooman, Curr Opin Solid State Mater Sci **8**, 285 (2004). 4, 6

[6] M. Hillert and L.-I. Staffansson, Acta Chem. Scand. **24**, 3618 (1970). 5

[7] B. Sundman and J. Ågren, J. Phys. Chem. Solids **42**, 297 (1981). 5

[8] M. Hillert, J. Alloys Compd. **320**, 161 (2001). 5

[9] J.-O. Andersson, T. Helander, L. Hölund, P. Shi, and B. Sundman, Calphad **26**, 273 (2002). 5

[10] G. Olson, Mat. Sci. and Eng. A **438–440**, 48 (2006). 5

[11] M. H. F. Sluiter, *Phase transformations in steels: First principles in modelling phase transformations in steels* (2012). 5

[12] S. Jenkins, http://newton.ex.ac.uk/research/qsystems/people/jenkins/mbody/mbody3.html 9, 10

[13] D. A. McQuarrie and J. D. Simon, *Physical Chemistry: A Molecular Approach*, University Science Books (1997). 10, 11, 12

[14] C. J. Cramer, *Essentials of Computational Chemistry (2nd Edition)*, John Wiley and Sons (2004). 10, 13, 14, 16, 17

[15] I. N. Levine, *Quantum Chemistry*, Prentice Hall (5th Edition) (1999). 10, 20, 23

[16] A. Szabo and N. S. Ostlund, *Modern Quantum Chemistry: Introduction to Advanced Electronic Structure Theory*, McGraw-Hill (1989). 10

[17] J. Klimeš, *PhD Thesis: Towards an accurate theoretical description of surface processes* (2011). 12, 25

[18] P. Hohenberg and W. Kohn, Phys. Rev. **136**, B864 (1964). 19, 55, 78, 90

[19] W. Kohn and L. J. Sham, Phys. Rev. **140**, A1133 (1965). 20, 55, 78, 90

[20] A. J. Cohen and N. C. Handy, Chem. Phys. Lett. **316**, 160 (2000). 24

[21] S. F. Sousa, P. A. Fernandes, and M. J. o. Ramos, J. Phys. Chem. A **111**, 10439 (2007). 24

[22] J. Hafner, J. Comput. Chem. **29**, 2044 (2008). 24

[23] J. Perdew, K. Burke, and M. Ernzerhof, Phys. Rev. Lett. **77**, 3865 (1996). 24

[24] J. Perdew, K. Burke, and M. Ernzerhof, Phys. Rev. Lett. **78**, 1396 (1997). 24

[25] C. S. Wang, B. M. Klein, and H. Krakauer, Phys. Rev. Lett. **54**, 1852 (1985). 24

[26] T. Asada and K. Terakura, Phys. Rev. B **46**, 13599 (1992). 24

[27] T. Asada and K. Terakura, Phys. Rev. B **48**, 17649 (1993). 24

[28] D. J. Singh, W. E. Pickett, and H. Krakauer, Phys. Rev. B **43**, 11628 (1991). 24

[29] R. Hafner, D. Spišák, R. Lorenz, and J. Hafner, Phys. Rev. B **65**, 184432 (2002). 24

[30] K. Burke, J. Chem. Phys. **136**, 150901(1 (2012). 24

[31] J. Klimeš and A. Michaelides, J. Chem. Phys. **137**, 120901 (2012). 24

[32] M. C. Payne, M. P. Teter, D. C. Allan, T. A. Arias, and J. D. Joannopoulos, Rev. Mod. Phys. **64**, 1045 (1992). 26, 28, 29

[33] F. Bloch, Z. Angew. Phys. **52**, 555 (1929). 28

[34] N. Ashcroft and N. Mermin, *Solid state physics*, Science: Physics, Saunders College (1976). 28

[35] H. J. Monkhorst and J. D. Pack, Phys. Rev. B **13**, 5188 (1976). 28, 56, 78, 90

[36] D. R. Hamann, M. Schlüter, and C. Chiang, Phys. Rev. Lett. **43**, 1494 (1979). 30

[37] D. Vanderbilt, Phys. Rev. B **41**, 7892 (1990). 30

[38] P. E. Blöchl, Phys. Rev. B **50**, 17953 (1994). 30, 55, 66, 78, 90

[39] M. Methfessel and A. T. Paxton, Phys. Rev. B **40**, 3616 (1989). 31

[40] M. Umemoto, Z. G. Liu, K. Masuyama, and K. Tsuchiya, Scr. Mater. **45**, 391 (2001). 34, 75, 76, 80

[41] F. Zhao, O. Tegus, B. Fuquan, and E. Brück, Int. J. Miner. Metall. Mater. **16**, 314 (2009). 34, 75

[42] L. J. E. Hofer and E. M. Cohn, Nature **167**, 977 (1951). 34, 87, 88

[43] J. W. Christian, *The Theory of Transformation in Metals and Alloys*, Pergamon Press, Amsterdam (2002). 34, 87, 88

[44] M. Manes, A. D. Damick, M. Menster, E. M. Cohn, and L. J. E. Hofer, J. Am. Chem. Soc. **74**, 6207 (1952). 34, 87

[45] Y. Hirotsu and S. Nagakura, Acta Metall. **20**, 645 (1972). 34, 35, 37, 87

[46] M. J. van Genderen, A. Böttger, R. J. Cernik, and E. J. Mittemeijer, Met. Trans. A **24**, 1965 (1993). 34, 88

[47] Y. Zhang, X. Zhao, N. Bozzolo, C. He, L. Zuo, and C. Esling, ISIJ Int. **45**, 913 (2005). 34, 88

[48] A. Dick, F. Körmann, T. Hickel, and J. Neugebauer, Phys. Rev. B **84**, 125101 (2011). 34, 88

[49] I. G. Wood, L. Vočadlo, K. S. Knight, D. P. Dobson, W. G. Marshall, G. D. Price, and J. Brodholt, J. Appl. Crystallogr. **37**, 82 (2004). 34, 35, 43, 75

[50] L. Vocadlo, J. Brodholt, D. P. Dobson, K. Knight, W. Marshall, G. Price, and I. G. Wood, Earth Planet. Sci. Lett. **203**, 567 (2002). 34, 75

[51] C. Yang, H. Zhao, Y. Hou, and D. Ma, J. Am. Chem. Soc. **134**, 15814 (2012). 34

[52] V. Moruzzi, J. Janak, and A. Williams, *Calculated electronic properties of metals*, Pergamon Press (1978). 34

[53] W. C. Chiou and E. A. Carter, Surf. Sci. **530**, 87 (2003). 34, 88

[54] I. R. Shein, N. I. Medvedeva, and A. L. Ivanovskiĭ, Physica B **371**, 126 (2006). 34, 88

[55] C. Jiang, B. P. Uberuaga, and S. G. Srinivasan, Acta Mater. **56**, 3236 (2008). 34, 47, 48, 49, 88

[56] B. Hallstedt, D. Djurovic, J. von Appen, R. Dronskowski, A. Dick, F. Körmann, T. Hickel, and J. Neugebauer, Calphad **34**, 129 (2010). 34, 43, 78, 80, 88

[57] C. Jiang, S. G. Srinivasan, A. Caro, and S. A. Maloy, J. Appl. Phys. **103**, 043502 (2008). 34, 43, 88

[58] Z. Q. Lv, W. T. Fu, S. H. Sun, X. H. Bai, Y. Gao, Z. H. Wang, and P. Jiang, J. Magn. Magn. Mater. **323**, 915 (2011). 34, 88

[59] M. Nikolussi, S. L. Shang, T. Gressmann, A. Leineweber, E. J. Mittemeijer, Y. Wang, and Z.-K. Liu, Scr. Mater. **59**, 814 (2008). 34, 88

[60] H. Ledbetter, Mat. Sci. and Eng. A **527**, 2657 (2010). 34, 43, 48, 88

[61] K. O. E. Henriksson, N. Sandberg, and J. Wallenius, Appl. Phys. Lett. **93**, 191912(1 (2008). 35, 43, 88

[62] P. J. Steynberg, J. A. van den Berg, and W. J. van Rensburg, J. Phys.: Condens. Matter **20**, 064238 (2008). 35, 88

[63] Z. Q. Lv, S. H. Sun, P. Jiang, B. Z. Wang, and W. T. Fu, Comput. Mater. Sci. **42**, 692 (2008). 35, 88

[64] E. J. Fasiska and G. A. Jeffrey, Acta Crystallogr. **19**, 463 (1965). 35, 37, 75

[65] G. Hägg, Z. Phys. Chem. B **12**, 33 (1931). 35

[66] J. P. Senateur, D. Fruchart, and A. Michel, Comptes Rendus Acad. Sci. **255**, 1615 (1962). 35

[67] K. H. Jack and S. A. Wild, Acta Crystallogr. **S21**, A81 (1966). 35

[68] J. P. Senateur, Ann. de Chimie **2**, 103 (1967). 35, 37

[69] J. J. Retief, Powder Diffract. **14**, 130 (1999). 35

[70] A. Leineweber, S. Shang, Z.-K. Liu, M. Widenmeyer, and R. Niewa, Z. Kristallogr. Crystalline Materials **227**, 207 (2012). 35

[71] H. E. du Plessis, J. P. de Villiers, and G. J. Kruger, Z. Kristallogr. Crystalline Materials **222**, 211 (2007). 35

[72] H. E. du Plessis, J. P. R. de Villiers, G. J. Kruger, A. Steuwer, and M. Brunelli, J. Synchrotron Radiat. **18**, 266 (2011). 35

[73] K. H. Jack, J. Iron Steel Inst. **169**, 26 (1951). 35

[74] K. H. Jack, Acta Crystallogr. **5**, 404 (1952). 35

[75] S. Nagakura and S. Oketani, Trans. ISIJ 8 **8**, 265 (1968). 35

[76] H. W. King, *CRC Handbook of Chemistry and Physics*, CRC Press/Taylor and Francis, Boca Raton, FL, 93 edition (2013). 37, 47

[77] O. Isnard and D. Fruchart, J. Alloys Compd. **205**, 1 (1994). 38

[78] H. Kopp, Philos. Trans. Roy. Soc. London **155**, 71 (1865). 39

[79] J. Leitner, P. Voňka, D. Sedmidubský, and P. Svoboda, Thermochim. Acta **497**, 7 (2010). 39

[80] C. Kittel, *Introduction to Solid State Physics*, John Wiley and Sons (1996). 40

[81] Wikipedia, *Debye model — Wikipedia, The Free Encyclopedia* (2012). 40

[82] D. Alfè, Comput. Phys. Commun. **180**, 2622 (2009). 40

[83] Y. Y. Chuang, R. Schmid, and Y. A. Chang, J. Mater. Sci. **16**, 153 (1985). 42

[84] G. Grimvall, *Thermophysical properties of materials*, North-Holland, Elsevier (1999). 42

[85] M. Widom and M. Mihalkovic, J. Mater. Res. **20**, 237 (2005). 43

[86] C. M. Fang, M. H. F. Sluiter, M. A. van Huis, C. K. Ande, and H. W. Zandbergen, Phys. Rev. Lett. **105**, 055503(1 (2010). 43, 45, 88

[87] J. Jang, I. Kim, and H. Bhadeshia, Comput. Mater. Sci. **44**, 1319 (2009). 43, 76, 77, 80, 82, 88

[88] J. von Appen, B. Eck, and R. Dronskowski, J. Comput. Chem. **31**, 2620 (2010). 43, 88, 98

[89] J. H. Jang, I. G. Kim, and H. K. D. H. Bhadeshia, Scr. Mater. **63**, 121 (2010). 43, 88, 89, 98

[90] J. H. Jang, I. G. Kim, and H. K. D. H. Bhadeshia, Mater. Sci. Forum **638–642**, 3319 (2010). 43, 88

[91] B. Brockhouse, H. Abou-Helal, and E. Hallman, Solid State Commun. **5**, 211 (1967). 43

[92] S. Klotz and M. Braden, Phys. Rev. Lett. **85**, 3209 (2000). 43

[93] S. P. Dodd, G. A. Saunders, M. Cankurtaran, B. James, and M. Acet, Phys. Status Solidi A **198**, 272 (2003). 43

[94] W. Voigt, Teuber 962 (1928). 46

[95] A. Reuss, ZAMM **9**, 55 (1929). 46

[96] R. Hill, Proc. Phys. Soc. London, Sect. A **65**, 349 (1952). 46

[97] Y. Le Page and P. Saxe, Phys. Rev. B **65**, 104104 (2002). 47

[98] A. Marmier, Z. A. Lethbridge, R. I. Walton, C. W. Smith, S. C. Parker, and K. E. Evans, Comput. Phys. Commun. **181**, 2102 (2010). 47

[99] J. Alkorta and J. G. Sevillano, J. Mater. Res. **27**, 45 (2011). 47

[100] R. Yu, J. Zhu, and H. Ye, Comput. Phys. Commun. **181**, 671 (2010). 48

[101] A. Cottrell, *Chemical bonding in transition metal carbides*, The Institute of Metals, London (1995). 48

[102] *Webelements*. 49

[103] T. Klymko and M. Sluiter, J. Mater. Sci. **47**, 7601 (2012). 55

[104] G. Rahman, I. G. Kim, H. K. D. H. Bhadeshia, and A. J. Freeman, Phys. Rev. B **81**, 184423 (2010). 55, 58, 59

[105] G. Kresse and J. Hafner, Phys. Rev. B **47**, 558 (1993). 55, 78, 90

[106] G. Kresse and J. Hafner, Phys. Rev. B **48**, 13115 (1993). 55, 78, 90

[107] G. Kresse and J. Hafner, Phys. Rev. B **49**, 14251 (1994). 55

[108] G. Kresse and J. Furthmüller, Comput. Mater. Sci. **6**, 15 (1996). 55, 66, 78, 90

[109] G. Kresse and J. Furthmüller, Phys. Rev. B **54**, 11169 (1996). 55, 66, 78, 90

[110] J. P. Perdew, J. A. Chevary, S. H. Vosko, K. A. Jackson, M. R. Pederson, D. J. Singh, and C. Fiolhais, Phys. Rev. B **46**, 6671 (1992). 55, 66, 78, 90

[111] J. Perdew and Y. Wang, Phys. Rev. B **45**, 13 (1992). 55

[112] S. H. Vosko, L. Wilk, and M. Nusair, Can. J. Phys. **58**, 1200 (1980). 55, 78, 90

[113] G. Henkelman, A. Arnaldsson, and H. Jónsson, Computational Materials Science **36**, 354 (2006). 56

[114] E. Sanville, S. D. Kenny, R. Smith, and G. Henkelman, Journal of Computational Chemistry **28**, 899 (2007). 56

[115] W. Tang, E. Sanville, and G. Henkelman, Journal of Physics: Condensed Matter **21**, 084204 (2009). 56

[116] VTST: http://theory.cm.utexas.edu/vasp/downloads/ 56

[117] B. Drittler, N. Stefanou, S. Blügel, R. Zeller, and P. H. Dederichs, Phys. Rev. B **40**, 8203 (1989). 58, 59, 60, 79

[118] A. P. Malozemoff, A. R. Williams, and V. L. Moruzzi, Phys. Rev. B **29**, 1620 (1984). 58

[119] V. A. Gubanov, A. L. Liechtenstein, and A. V. Postnikov, *Magnetism and electronic structure of crystals*, Springe, Berlin (1992). 58

[120] V. I. Anisimov, V. P. Antropov, A. I. Liechtenstein, V. A. Gubanov, and A. V. Postnikov, Phys. Rev. B **37**, 5598 (1988). 59

[121] J. A. Slane, C. Wolverton, and R. Gibala, Metall. Mater. Trans. A **35 A**, 2239 (2004). 65

[122] C. S. Becquart, J. M. Raulot, G. Bencteux, C. Domain, M. Perez, S. Garruchet, and H. Nguyen, Comput. Mater. Sci. **40**, 119 (2007). 65

[123] K. Tapasa, A. V. Barashev, D. J. Bacon, and Y. N. Osetsky, Acta Mater. **55**, 1 (2007). 65

[124] A. Schneider and G. Inden, Calphad **31**, 141 (2007). 65

[125] A. Strahl, I. S. Golovin, H. Neuhäuser, S. B. Golovina, and H. . Sinning, Mater. Sci. Eng., A **442**, 128 (2006). 65, 67

[126] T. Nishizawa, K. Ishida, H. Ohtani, C. Kami, and M. Suwa, Scand. J. Metall. **20**, 62 (1991). 65

[127] I. S. Golovin, M. S. Blanter, and L. B. Magalas, *Interactions of dissolved atoms and carbon diffusion in Fe-Cr and Fe-Al alloys*, number 194-199 PART 1 in Defect and Diffusion Forum (2001). 65

[128] D. Ruiz, J. L. Rivera-Tovar, D. Segers, R. E. Vandenberghe, and Y. Houbaert, Mater. Sci. Eng., A **442**, 462 (2006). 65

[129] I. S. Golovin, S. V. Divinski, J. Čížek, I. Procházka, and F. Stein, Acta Mater. **53**, 2581 (2005). 65

[130] M. S. Blanter and L. B. Magalas, Scr. Mater. **43**, 435 (2000). 65

[131] M. Koiwa and H. Numakura, *The Snoek effect in ternary BCC alloys. A review*, volume 115 of *Diffusion and Defect Data Pt.B: Solid State Phenomena* (2006). 65

[132] H. Numakura, G. Yotsui, and M. Koiwa, Acta Metallurgica et Materialia **43**, 705 (1995). 65

[133] I. S. Golovin and S. B. Golovina, Phys. Met. Metall. **102**, 593 (2006). 65

[134] C. A. Wert and R. C. Frank, Annu. Rev. Mater. Sci. **13**, 139 (1983). 65, 71

[135] S. Etienne, S. Elkoun, L. David, and L. B. Magalas, *Mechanical spectroscopy and other relaxation spectroscopies*, volume 89 of *Diffusion and Defect Data Pt.B: Solid State Phenomena* (2003). 65

[136] H. Saitoh, N. Yoshinaga, and K. Ushioda, Acta Mater. **52**, 1255 (2004). 65

[137] D. E. Jiang and E. A. Carter, Phys. Rev. B **67**, 2141031 (2003). 65, 66, 67

[138] C. Domain, C. S. Becquart, and J. Foct, Phys. Rev. B **69**, 144112 (2004). 65, 67

[139] C. Domain, J. Nucl. Mater. **351**, 1 (2006). 65, 67

[140] D. Simonovic and M. H. F. Sluiter, Phys. Rev. B **79** (2009). 65

[141] Y. A. Krishtal, Fiz. Met. Metalloved. **19**, 111 (1965). 65

[142] A. Okamoto, M. Takahashi, and T. Hino, Trans. Iron. Steel Inst. of Jpn. **21**, 802 (1981). 65, 73

[143] F. Walz, T. Wakisaka, and H. Kronmüller, Phys. Status Solidi A **202**, 2667 (2005). 65, 67, 73

[144] D. Simonovic, C. K. Ande, A. I. Duff, F. Syahputra, and M. H. F. Sluiter, Phys. Rev. B **81**, 054116 (2010). 66, 69, 71

[145] G. Kresse and D. Joubert, Phys. Rev. B **59**, 1758 (1999). 66

[146] G. Henkelman, B. P. Uberuaga, and H. Jónsson, J. Chem. Phys. **113**, 9901 (2000). 66

[147] G. Henkelman and H. Jónsson, J. Chem. Phys. **113**, 9978 (2000). 66

[148] C. A. Wert, Phys. Rev. **79**, 601 (1950). 67

[149] S. Takaki, J. Fuss, H. Kugler, U. Dedek, and H. Schultz, Radiation effects **79**, 87 (1983). 67

[150] M. Weller, J. Phys. Colloques **46**, 10 (1985). 67

[151] W. Pascheto and G. P. Johari, Metall. Mater. Trans. A **27**, 2461 (1996). 67

[152] S. A. Crooker and N. Samarth, Appl. Phys. Lett. **90** (2007). 67

[153] W. Leslie, Metallurgical Transactions **3**, 5 (1972). 67

[154] B. Predel, in O. Madelung (editor), *Dy-Er – Fr-Mo*, volume 5e of *Landolt-Börnstein - Group IV Physical Chemistry*, 1–6, Springer Berlin Heidelberg (1995). 67

[155] K. Lee, H. Yang, and H. Kwon, Metall. Mater. Trans. A **32**, 1659 (2001). 75

[156] H. Kwon, C. Kim, K. Lee, H. Yang, and J. Lee, Metall. Mater. Trans. A **29 A**, 397 (1998). 75

[157] D. V. Edmonds, Materials Science Forum **638–642**, 110 (2010). 75

[158] S. Godet, C. Georges, and P. J. Jacques, in *Material Science and Technology Meeting 2003*, 523–536 (2003). 75

[159] M. Santofimia, L. Zhao, Y. Takahama, and J. Sietsma, Mater. Sci. Forum **638–642**, 3485 (2010). 75

[160] C. Zhu, X. Xiong, A. Cerezo, R. Hardwicke, G. Krauss, and G. Smith, Ultramicroscopy **107**, 808 (2007). 75

[161] J. Takahashi, K. Kawakami, M. Sugiyama, and T. Tarui, J. Iron. Steel Inst. Jpn. **93**, 145 (2007). 75

[162] D. Parsons, T. Malis, and J. Boyd, J. Heat. Treat. **3**, 213 (1984). 75, 76

[163] R. Thomson and M. Miller, Appl. Surf. Sci. **87-88**, 185 (1995). 75, 76, 80, 97, 98

[164] M. Ko, T. Sakuma, and T. Nishizawa, J. Jpn. Inst. Met. **40**, 593 (1976). 75, 76, 80, 83, 97, 98

[165] J. Chance and N. Ridley, Metall. Mater. Trans. A **12 A**, 1205 (1981). 75

[166] N. Ridley, M. Malik, and G. Lorimer, Mater. Charact. **25**, 125 (1990). 75

[167] R. Thomson and M. Miller, Acta Mater. **46**, 2203 (1998). 75, 76, 80, 97, 98

[168] S. Al-Salman, G. Lorimer, and N. Ridley, Acta Metall. **27**, 1391 (1979). 75

[169] Z.-K. Liu, L. Höglund, B. Jönsson, and J. Ågren, Metall. Mater. Trans. A **22**, 1745 (1990). 75

[170] N. Razik, G. Lorimer, and N. Ridley, Metall. Trans. A **7 A**, 209 (1976). 75

[171] S. Babu, K. Hono, and T. Sakurai, Metall. Mater. Trans. A **25**, 499 (1994). 75

[172] S. Babu, K. Hono, and T. Sakurai, Appl. Surf. Sci. **67**, 321 (1993). 75

[173] Q. Liu, Y. Chu, Z. Wang, W. Liu, and B. Zhou, Acta Metall. Sinica **44**, 1281 (2008). 75, 76, 80, 97

[174] G. Miyamoto, J. Oh, K. Hono, T. Furuhara, and T. Maki, Acta Mater. **55**, 5027 (2007). 75

[175] J. Lis, J. Morgiel, and A. Lis, Mater. Chem. Phys. **81**, 466 (2003). 75

[176] M. Miller and G. Smith, Met. Sci. **11**, 249 (1977). 75, 76

[177] J. Lis, A. Lis, and C. Kolan, Mater. Charact. **59**, 1021 (2008). 75

[178] S. Al-Salman, G. Lorimer, and N. Ridley, Metall. Trans. A **10**, 1703 (1979). 75

[179] W. Leslie and G. Rauch, Metall. Trans. A **9 A**, 343 (1978). 76, 80, 97

[180] G. Dunlop, C.-J. Carlsson, and G. Frimodig, Metall. Mater. Trans. A **9**, 261 (1978). 76

[181] D. Shtansky and G. Inden, Acta Mater. **45**, 2861 (1997). 76, 80

[182] R. Wu, A. Freeman, and G. Olson, Science **265**, 376 (1994). 76

[183] R. Ding, T. Rong, and J. Knott, Mater. Sci. Technol. **21**, 85 (2005). 76

[184] I. Shein, N. I. Medvedeva, and A. L. Ivanovskiĭ, Phys. Status Solidi B **244**, 1971 (2007). 76, 77, 80, 82, 88, 89, 92

[185] I. G. Jang, J. H.and Kim and H. K. D. H. Bhadeshia, Mater. Sci. Forum **638-642**, 3319 (2009). 76, 77, 80, 82

[186] C. Zhou, B. Xiao, J. Feng, J. Xing, X. Xie, Y. Chen, and R. Zhou, Comput. Mater. Sci. **45**, 986 (2009). 76, 88

[187] N. I. Medvedeva, L. E. Kar'kina, and A. L. Ivanovskiĭ, Phys. Solid State **48**, 15 (2006). 76, 88

[188] S. Khmelevskyi, A. Ruban, and P. Mohn, J. Phys.: Condens. Matter **17**, 7345 (2005). 77

[189] F. Kormann, A. Dick, B. Grabowski, B. Hallstedt, T. Hickel, and J. Neugebauer, Phys. Rev. B: Condens. Matter **78**, 033102 (2008). 78

[190] M. H. F. Sluiter, in D. Seidman, P. Bellon, C. Abromeit, and J.-L. Boquet (editors), *Mat. Res. Soc. Proc.*, 43–48 (2006). 78, 91

[191] C. M. Fang, M. A. van Huis, and H. W. Zandbergen, Phys. Rev. B **80**, 224108 (2009). 80

[192] S. V. Meschel and O. J. Kleppa, J. Alloys Compd. **321**, 183 (2001). 80

[193] L. Samek, E. De Moor, J. Penning, and B. C. De Cooman, Met. Mat. Trans. A **37A**, 109 (2006). 82

[194] O. Y. Gutina, N. I. Medvedeva, I. R. Shein, A. L. Ivanovskiĭ, and J. E. Medvedeva, Phys. Status Solidi B **246**, 2167 (2009). 88, 95

[195] M. Konyaeva and N. Medvedeva, Phys. Solid State **51**, 2084 (2009). 88

[196] Z. Q. Lv, W. T. Fu, S. H. Sun, Z. H. Wang, W. Fan, and M. G. Qv, Solid State Sci. **12**, 404 (2010). 88

[197] N. Medvedeva, I. Shein, M. Konyaeva, and A. Ivanovskiĭ, Phys. Met. Metall. **105**, 568 (2008). 88

[198] X. Wang and M. Yan, Int. J. Mod. Phys. B **23**, 1135 (2009). 88

[199] N. Medvedeva, I. Shein, O. Gutina, and A. Ivanovskiĭ, Phys. Solid State **49**, 2298 (2007). 88

[200] C. K. Ande and M. H. F. Sluiter, Acta Mater. **58**, 6276 (2010). 88, 89, 91, 92, 97

[201] R. Benedek, A. van de Walle, S. S. A. Gerstl, M. Asta, D. N. Seidman, and C. Woodward, Phys. Rev. B **71**, 094201(1 (2005). 90

[202] P. E. Blöchl, O. Jepsen, and O. K. Andersen, Phys. Rev. B **49**, 16223 (1994). 90

[203] G. P. Huffman, P. R. Errington, and R. M. Fisher, Phys. Status Solidi B **22**, 473 (1967). 97, 98

[204] L. Qingdong, L. Wenqing, W. Zemin, and Z. Bangxin, Acta Metall. Sinica **45**, 1281 (2009). 97

[205] E. Kozeschnik and H. K. D. H. Bhadeshia, Met. Mat. Sci. Tech **24**, 343 (2008). 97

Publications

1. C. K. Ande and M. H. F. Sluiter, First-principles calculations on stabilization of iron carbides Fe_3C, Fe_5C_2, and η-Fe_2C in steels by common alloying elements, Met. Mat. Trans. A, **43**, 4436-4444 (2012) (Chap. 7)

2. T. Klymko, C. K. Ande, M. H. F. Sluiter, Solubility products for precipitate phases in steels from first-principles calculations, MRS Proceedings, **1296** (2011)

3. C. K. Ande and M. H. F. Sluiter, First-principles prediction of partitioning of alloying elements between cementite and ferrite, Acta. Mat., **58**, 6276 (2010) (Chap. 6)

4. C. M. Fang, M. H. F. Sluiter, M. A. van Huis, C. K. Ande and H. W. Zangbergen, Origin of predominance of cementite among iron carbides in steel at elevated temperatures, Phys. Rev. Lett., **105**, 055503 (2010) (based on Chap. 3)

5. D. Simonovic, C. K. Ande, A. I. Duff, F. Syahputra and M. H. F. Sluiter, Diffusion of Carbon in bcc-Fe in the presence of Si, Phys. Rev. B., **81**, 054116 (2010)
   D. Simonovic, C. K. Ande, A. I. Duff, F. Syahputra and M. H. F. Sluiter, Erratum: Diffusion of Carbon in bcc-Fe in the presence of Si, Phys. Rev. B., **81**, 054116 (2010) (based on Chap. 5)

Summary

We used Density Functional Theory based first principles plane-wave calculations to determine which alloying elements can be used to suppress the formation of iron carbides in transformation induced plasticity (TRIP) steels. TRIP steels are low-alloy steels that combine properties of enhanced strength and ductility that satisfy the requirements of the automotive industry for good formable high-strength steels. To obtain a good TRIP effect, it is essential to retain the austenite phase to room temperature. Carbon is the most effective alloying element for the stabilization of austenite to room temperature. However, it is usually lost to precipitating carbides during the cooling of steel from the austenite phase to room temperature. The loss of C can be avoided by adding appropriate alloying elements that destabilize the formation of the carbide phases (Chap. 1). We used Density Functional Theory (DFT) based first-principles calculations (Chap. 2) to quantitatively determine the degree of (de)stabilization by various alloying elements to the formation of iron carbides (Chap. 6 and 7).

First, it was made sure that DFT accurately describes the ground state structural, mechanical and vibrational properties of the pure phases and we see good agreement in this regard with experimental data. Structural (crystal structure), mechanical (bulk modulus, Young's modulus, shear modulus, Poisson ratio), electronic (total and partial electronic density of states) and magnetic properties (total and atomic magnetic moments) of iron and iron carbides in their ground state are well described by DFT (Chap. 3). While in the quasi-harmonic approximation it is also relatively straightforward to obtain the high temperature vibrational properties (vibrational free energy, Debye temperature) of the phases considered in this thesis, it is relatively difficult to obtain the high temperature magnetic properties (magnetic free energy) (Chap. 3).

Although the exact formation energies of different alloy phases cannot be determined to chemical accuracy, the relative difference in formation energies can be obtained accurately using DFT. We find that the stability of the carbides increases in the order: $Fe_3C < Fe_5C_2 < \eta\text{-}Fe_2C$. It should be noted though that the stabilities were calculated at a temperature of 0 K. At finite temperatures, vibrational, magnetic and electronic free energies will have to be included to compare their stabilities (Chap. 3). The inclusion of vibrational and magnetic free energies leads to a change in the stability of the carbides at higher temperatures and make cementite (Fe_3C) stable at higher temperatures. This explains the predominance of cementite in steels (Chap. 3).

In dilute solutions of Ti, V, Sc, Cu and Zn in bcc-Fe a negative magnetic moment is induced on the alloying element atoms by the positive moments of the surrounding Fe atoms. Cr, Mn, Ni and Co have intrinsic moments. The total magnetic moment of an impurity substituted bcc-Fe supercell changes as if the change in magnetism is brought about completely due to the change in the volume of the supercell of pure bcc-Fe without the impurity atom (Chap. 4).

Si in bcc-Fe reduces the chemical potential and diffusivitiy of C in bcc-Fe. Dissolved at low concentrations in bcc-Fe Si diminishes the thermodynamic driving force for carbide formation. The suppression of carbide formation by Si has two aspects: a) it reduces the driving force for carbide precipitation by reducing the chemical potential of C by attracting and trapping it in ferrite and b) by reducing the C diffusivity in ferrite (Chap. 5).

Formation enthalpies were shown not to correctly describe the (de)stabilization of carbides, nor do they describe correctly the partitioning of alloying elements between carbides and bcc-Fe phases accurately (Chap. 6 and 7). It is seen that the partitioning energy, defined in this work thesis, describes the (de)stabilization of carbides by alloying elements better than formation energies (Chap. 6 and 7). In agreement with experimental measurements, our calculations show that Si, Al and P are the alloying elements that destabilize carbides the most when replacing Fe in the carbide (Chap. 6 and 7). On a per atomic fraction basis, Si is more effective than Al in the destabilization of the carbides. Our calculations show that magnetism can play an important role in determining the stability of iron carbides accurately.

All the alloying elements, except Mn, destabilize η-Fe_2C relative to Fe_3C and Fe_5C_2. The competition between Fe_3C and Fe_5C_2 is strongly affected by alloying elements. While Si, Mo and W stabilize Fe_5C_2 relative to Fe_3C, Ti, Mn and Nb do the opposite. Mn stabilizes both Fe_5C_2 and η-Fe_2C to a comparable degree over Fe_3C (Chap. 7).

At finite temperature, observed partitioning behavior of Cr, V, Mo and W are not explained satisfactorily by the present first-principles, 0 K partitioning enthalpies. For a good first principles description of the partitioning behavior, the paramagnetic nature of the carbides at higher temperatures should be taken into account (Chap. 6 and 7).

First-principles calculations complemented by a straightforward formalism for calculating the magnetic free energies can prove be invaluable in the design of new steels.

Samenvatting

Ab initio vlakke-golf berekeningen gebaseerd op "density functional" theorie zijn gebruikt om te bepalen welke legeringselementen toegepast kunnen worden om de vorming van ijzercarbides in "transformation induced plasticity" (TRIP) staalsoorten te onderdrukken. TRIP staalsoorten zijn laag-gelegeerd met een combinatie van eigenschappen zoals verbeterde sterkte en taaiheid die voldoen aan de toepassingseisen van de auto industrie voor goed vervormbare hoge-sterkte staal. Om een goed TRIP effect te verkrijgen is het essentieel om de austeniet fase the behouden tot kamertemperatuur. Koolstof is het meest effectieve legeringselement voor de stabilisatie van austeniet. Het gaat echter vaak verloren door de vorming van carbide precipitaten uit de austeniet fase tijdens het afkoelen van staal naar kamertemperatuur. Het verlies van koolstof kan voorkomen worden door toevoeging van bepaalde legeringselementen die de vorming van carbides tegengaan (hoofdstuk 1). Density functional theorie (DFT) gebaseerde ab initio berekeningen (hoofdstuk 2) zijn toegepast om kwantitatief te bepalen hoe sterk verschillende legeringselementen de ijzercarbides (de)stabilizeren (hoofdstukken 6 en 7).

Eerst is gecontroleerd dat DFT nauwkeurig de structurele, mechanische en vibrationele eigenschappen van de pure fasen in hun grondtoestand beschreef. Dat bleek het geval: goede overeenkomst werd gevonden met experimentele gegevens. Kristalstructuur, mechanische (compressiemodulus, elasticiteitsmodulus, schuifmodulus, en dwarscontractiecoëfficiënt van Poisson), elektronische (totale en partiële toestandsdichtheden) en magnetische eigenschappen (totale en atoomgebonden magnetische momenten) van ijzer en ijzercarbides in de grondtoestand blijken goed beschreven te worden door DFT (hoofdstuk 3). Terwijl in de quasiharmonische benadering de hoge-temperatuur vibrationele eigenschappen (vibrationele vrije energie, Debye temperatuur) relatief eenvoudig berekend kunnen worden voor de fasen die in dit proefschrift voorkomen, is dat niet het geval voor de hoge temperatuur magnetische eigenschappen zoals de magnetische vrije energie (hoofdstuk 3).

Hoewel de exacte formatie-energieën van verschillende legeringsfasen niet tot chemische nauwkeurigheid bepaald kunnen worden, is het toch mogelijk formatie-energie verschillen nauwkeurig te bepalen met DFT. Wij hebben vastgesteld dat de stabiliteit van de carbide fasen toeneemt in de volgorde: $Fe_3C < Fe_5C_2 < \eta\text{-}Fe_2C$. Waarbij opgemerkt moet worden dat deze stabiliteiten berekend zijn bij een temperatuur van 0 K. Om de stabiliteit bij niet-nul temperatuur te vergelijken moeten de vrije energiebijdragen van vibrationele, magnetische, en elektronische excitaties meegenomen worden (hoofdstuk 3). Het meenemen van vibrationele en magnetische vrije energieën verandert de relatieve stabiliteit van de carbides bij hogere temperaturen en leidt tot het stabiel worden van cementiet (Fe_3C). Dit verklaart de overheersende aanwezigheid van cementiet in staal (hoofdstuk 3).

In vaste oplossingen van Ti, V, Sc, Cu en Zn in kubisch ruimtelijk gecentreerd (krg) ijzer wordt een negatief magnetisch moment geïnduceerd op de legeringsatomen ten opzichte van de positieve momenten van de omringende ijzer atomen. De legeringselementen Cr, Mn, Ni, en Co hebben een intrinsiek magnetisch moment Het totale magnetische moment van een krg-Fe supercel waarin een Fe atoom vervangen wordt door een legeringselementatoom verandert alsof uitsluitend de bijkomende volumeverandering van een Fe supercel zonder legeringselementatoom verantwoordelijk is (hoofdstuk 4).

Si in krg-Fe vermindert de chemische potentiaal en de diffusiviteit van C in krg-Fe. Opgelost in lage concentraties in krg-Fe vermindert Si de thermodynamische drijvende kracht voor carbide formatie. Het onderdrukken van carbidevorming door Si heeft twee aspecten: a) Si vermindert de drijvende kracht voor carbide precipitatie door het verminderen van de chemische potentiaal van C via de aantrekking en binding van C in ferriet, en ook omdat b) Si de C diffusiviteit in ferriet vermindert (hoofdstuk 5).

Het is aangetoond dat formatie-enthalpieën de (de)stabilizatie van carbides niet correct weergeven. Ook geven de formatie-enthalpieën geen correcte weergave van de partitioneering van legeringselementen tussen de carbide en krg-Fe fasen (hoofdstukken 6 en 7). De partitioneeringsenergie, zoals gedefinieerd in dit proefschrift, beschrijft de (de)stabilizatie van carbides door legeringselementen veel beter dan de formatie energieën. Overeenkomstig experimentele metingen, geven onze berekeningen aan dat Si, Al, en P de legeringselementen zijn die carbides het meest destabilizeren wanneer deze elementen Fe vervangen in de carbides (hoofdstukken 6 en 7). Beoordeeld per atoom is Si effectiever dan Al voor het destabilizeren van carbides. Onze berekeningen tonen aan dat magnetisme een belangrijke rol kan spelen in het bepalen van de carbide stabiliteit.

Alle legeringselementen, met uitzondering van Mn, destabilizeren η-Fe_2C in verhouding tot Fe_3C en Fe_5C_2. De competitie tussen Fe_3C en Fe_5C_2 wordt sterk beïnvloed door legeringselementen. Hoewel Si, Mo en W Fe_5C_2 stabilizeren ten opzichte van Fe_3C, doen Ti, Mn en Nb het tegenovergestelde. Mn stabilizeert zowel Fe_5C_2 als η-Fe_2C over Fe_3C in een vergelijkbare mate (hoofdstuk 7).

Het bij niet-nul temperatuur waargenomen partitioneeringsgedrag van Cr, V, Mo, en W is niet bevredigend verklaard door de huidige ab initio 0 K partitioneerings enthalpieën. Voor een goede ab initio beschrijving van het partitioneeringsgedrag zal het paramagnetisme van de carbides bij hogere temperatuur in aanmerking moeten worden genomen (hoofdstukken 6 en 7).

Ab initio berekeningen gecomplimenteerd met een eenvoudig formalisme voor magnetische vrije energieën zouden van onschatbare waarde zijn voor het ontwikkelen van nieuwe staalsoorten.

Acknowledgements

The present thesis would not have been possible without the help and support of a number of people. I take this opportunity to thank all the people who made this possible.

First and foremost, I have to thank Marcel Sluiter, my supervisor, adviser and mentor during my Ph.D., for his boundless optimism, patience and support. Thanks for always being positive, curious and enthusiastic about things; this has shown me a new way of looking at the world. Also, thanks for giving me the time and space to find myself.

Although Prof. Barend Thijsse has not been my daily supervisor, his genuine humility, lack of ego, enthusiasm towards Science and his skill to explain involved concepts in simple terms have always been an inspiration. Thanks a lot for your patience and support during the completion of this thesis.

I would have never made it to the Netherlands if not for Prof. Yashonath Subramanian, my Master thesis supervisor at the Indian Institute of Science, Bengaluru, India. Thanks a lot for getting me in contact with Marcel and starting off this whole endeavor. In this regard, I also wish to thank Jayashree Nagesh for encouraging me to look for more challenging opportunities.

A special thanks should go to Anke Kerklaan-Koene for taking good care of all my travel bills. Also, all the staff at M2i, Oscar Ruigrok and Monica Reulink in particular, have been very helpful.

Another person, whom I have never even met in person, without whose expertise this work would never have been possible is Peter Bloom. Kudos for having almost no downtime on the computing cluster, hpc06, and for installing everything that I ever asked for.

Jeroen Colijn, whose untimely demise has been a shock, was extremely warm and kind during all my visits and internship at Tata Steel Europe. It was a great learning experience when he took me around the steel plant in IJmuiden - my first contact with steel in real life. Winfried Kranendonk, thanks a lot for the very careful reading of my thesis and all the detailed comments; I really appreciate them. In this aspect, thanks are also due to Prof. Dirk Lamoen and Prof. Rob de Groot for a careful reading of the thesis and the valuable comments.

Next, come all my colleagues and friends on the 8D Fourth Floor of 3mE: Andrew (Andy) Duff, Darko Simonovic, Diana Nanu, Emre Sururi Taşci, Fidel Valega,

Georgina Zimbitas, Venkata Girish, Ivan Lazić, Maria Timonova, Önnaz Ozkanat, Raymond Machunze, Sebastian Echeverri Restrepo, Stefanie Göthel, Tetyana Klymko, Vadym Kochubey and Vanya Uluc. If not for some of you guys, it would have been very hard for me to cope with the shock of living in a foreign country for the first time. Thanks to you and the others for making my time enjoyable at the department.

Then comes the Spanish gang: Angela, Amelia, Jesus, Jose, Maria, Maria-Luisa, Nerea, Sofia and Yaiza. Each of you has been special in one way or the other. I will always have a special place for Spaniards all because of how great you guys have been to hang out with.

Raghu for helping me during the very first days in Delft; Navin for nudging me all the time, with a good amount of sarcasm, to wrap up things; Rajitha for the great food, and Raam for giving me great company during our occasional travels. Vishnu and Srinath for the innumerable hours of jovial company in Eindhoven.

Muru, Suresh and Kanag - thanks a lot for keeping me great company during the hardest period of my stay in Delft. And of course, for all the great cooking - first by yourself and then by your partners Then, Vijaya Latha and Savitha respectively.

Maruti, Sarav - the best of everything that happened in Delft is of course due to you guys. I will keep it short. Thanks for being such awesome flatmates. Of course, Vinoth should be there in the list too.

I would like to thank Prof. Erwin Kessels, PMP, TU Eindhoven, for acting expeditiously and enabling my uninterrupted stay in the Netherlands after my Ph.D. I would also like to thank him for giving me additional time to finish my thesis during the last stages. Thanks are also due to all the present and past members of PMP for making my stay really enjoyable in the group.

To Catherine, for bringing additional cheer and happiness into my life and for just being there.

Finally, my parents, especially my mother, my brother and also the extended family have been extremely patient, supportive and understanding during the course of this Ph.D. Thanks a lot for selflessly standing by my side all this time.

Curriculum vitae

26 December 1982	Born in Vijayawada, Andhra Pradesh, India
1986-1998	Primary and Secondary School, Siddhartha Residential School, Vijayawada, Andhra Pradesh, India
1998-2000	Intermediate, Andhra Loyola College, Vijayawada, Andhra Pradesh, India
2000-2003	Bachelor of Science (Chemistry, Physics, Math), Andhra Loyola College, Vijayawada, Andhra Pradesh, India
2003-2006	Master of Science (Chemical Sciences), Indian Institute of Science, Bengaluru, Karnataka, India
2006-2007	Research and Development Assistant, Jawaharlal Nehru Center for Advanced Scientific Research, Bengaluru, Karnataka, India
2007-2011	Ph. D. Researcher, 1) Materials innovation institute (M2i), Delft, The Netherlands 2) Virtual Materials Lab., Dept. of Materials Science and Engineering, Delft University of Technology, Delft, The Netherlands